UCL
Université catholique de Louvain

École polytechnique de Louvain (EPL)

epl

Realisation of a Lithium-ion Battery Model for Microgrid Applications and Validation with Real-time Simulation Platform

Dissertation presented by
Maxime LEGRAIVE

for obtaining the master's degree in
Electro-mechanical Engineering
with Specialization in Energy

Supervisor
Emmanuel DE JAEGER

Readers
Marc BEKEMANS, Yann PANKOW

Academic year 2016-2017

Contents

Acronyms

AC Alternative current
BESS Battery energy storage system
BMS Battery management system
DAB Dual active bridge
DC Direct current
DER Distributed energy resource
DG Distributed generator / Distributed generation
EPLL Enhanced phase-locked loop
ESS Energy storage system
EV Electric vehicle(s)
FEC Full equivalent cycles
HC Harmonic compensator
HF High frequency
HT Hydraulic turbine
HV High voltage
ICE Internal combustion engine
IGBT Insulated gate bipolar transistor
LV Low voltage
LVRT Low-voltage ride-through
MOSFET Metal-oxide-semiconductor field-effect transistor
PCC Point of common coupling
PHIL Power hardware in the loop
PI Proportional-integral
PLL Phase-locked loop
PR Proportional-resonant
PV Photovoltaic
PWM Pulse width modulation
RES Renewable energy source
RMS Root mean square
ROCOF Rate of change of frequency
SG Synchronous generator
SMES Superconducting magnetic energy storage
SOC State-of-charge
SOH State-of-health
SRF-PLL Synchronous reference frame phase-locked loop

SSE Système de stockage d’énergie

SSEB Système de stockage d’énergie par batterie

TDD Total demand distortion

THD Total harmonic distortion

UPS Uninterruptible power system

VSI Voltage source inverter

V2G Vehicle-to-grid

WT Wind turbine

ZCS Zero current switching

Résumé

La technologie de batterie lithium-ion est relativement nouvelle : elle a été commercialisée pour la première fois en 1991. Depuis, les batteries lithium-ion ont été principalement utilisées dans les appareils portables comme les ordinateurs et les téléphones. Étant donné que la technologie est neuve, elle a constamment progressé au cours des dernières années, ce qui a entraîné une diminution du prix et une amélioration des performances. Aujourd'hui, les batteries Li-ion sont largement utilisées dans les voitures électriques. Il y a donc un intérêt clair pour les compagnies automobiles à investir dans cette technologie et à continuer à l'améliorer. En outre, il est maintenant envisageable d'utiliser ces batteries dans les réseaux électriques. En effet, les investissements dans les énergies renouvelables, en particulier le solaire et l'éolien, sont en augmentation. Comme ces sources d'énergie sont intermittentes, il y a un besoin croissant de systèmes de stockage performants.

D'autre part, la production d'énergie de plus en plus dispersée encourage à développer de nouvelles manières d'organiser le réseau électrique. Les micro-réseaux se présentent comme une manière intéressante d'intégrer plus facilement ces nouvelles sources d'énergie. Un micro-réseau est défini comme un ensemble de charges et de sources d'énergie, avec des frontières électriques clairement délimitées, qui peut se connecter et se déconnecter du réseau principal. Tandis que le réseau est traditionnellement organisé de manière centralisée où la puissance vient de larges générateurs synchrones connectés en haute tension, les micro-réseaux constituent une manière plus décentralisée d'organiser la distribution d'énergie, avec des sources connectées en basse tension. Grâce à un contrôle plus local, l'intermittence des sources renouvelables peut être mieux compensée. De plus, en cas d'incident sur le réseau principal, un micro-réseau peut s'en déconnecter et fournir l'énergie nécessaire aux charges locales. Ainsi, les micro-réseaux offrent la possibilité d'une distribution d'énergie plus sûre et de meilleure qualité. Cependant, pour qu'un micro-réseau constitué d'une part importante de sources renouvelables fonctionnent correctement, il est nécessaire d'inclure des systèmes de stockage d'énergie (SSE). Plusieurs technologies de SSE sont disponibles, parmi lesquelles la batterie Li-ion est une des plus prometteuses.

Dans ce contexte, ce mémoire présente un modèle complet de système de stockage d'énergie par batterie (SSEB) Li-ion. Ce modèle inclut la batterie Li-ion elle-même, ainsi que les différents filtres, convertisseurs et contrôleurs. Les performances dynamiques du SSEB sont mises en évidence pour observer comment celui-ci peut aider à stabiliser un micro-réseau. En plus de cela, la robustesse du SSEB face aux possibles perturbations du réseau et la qualité du courant injecté sont évaluées. Le modèle a été construit et testé sur Matlab Simulink®. Il a également réussi à fonctionner sur un simulateur temps réel, ce qui prouve la faisabilité des contrôleurs.

Les résultats des simulations montrent que le SSEB, grâce à son temps de réponse rapide, aide efficacement à stabiliser un micro-réseau. Plus spécifiquement, le SSEB a été testé en régulation de fréquence (inertie virtuelle et réserve primaire) dans un exemple simple de micro-réseau. En outre, moyennant une conception appropriée des filtres et contrôleurs, le SSEB est robuste face aux harmoniques, déséquilibre et assure une bonne qualité de l'électricité.

Abstract

Litihium-ion battery is a relatively new technology that was first commercialized in 1991. Since then, litihum-ion batteries have been mainly used for small portable technologies such as phones and computers. As it is a new technology, it has been constantly improving over the past few years, resulting in lower cost and better performances. Lithium-ion batteries are now widely used in electric vehicles and there is thus a strong incentive for car companies to further improve this technnology. In addition to that, perspectives of using Li-ion batteries for grid applications have opened up. In fact, investements in renewable energy sources are increasing, with particular attention to wind and solar power plants. The intermittence of theses resources requires high energy efficiency storage systems.

At the same time, the emergence of distributed energy resources (DER) has stimulated research into new ways of organizing the electrical grid. Microgrid technologies have attracted increasing attention as an effective mean of integrating such DER units into power systems. A microgrid is defined as a group of interconnected loads and distributed energy resources within clearly defined electrical boundaries that can connect and disconnect from the main grid to enable it to operate in both grid-connected or island mode. Whereas traditional power grids are very centralized with power flowing from large synchronous generators connected in high voltage, microgrids appear as a way to organize the electrical grid in a more decentralized manner with DER connected in low voltage. By using local control, the intermittency of renewable sources can be better compensated. Moreover, in case of power outage in the main grid, a microgrid can disconnect and provide power for the local loads. It can thus give an improved level of power quality and reliability for end-users. However, microgrids with an important share of renewable sources need enery storage systems (ESS) to provide these features. Several technologies of ESS are available, among which Li-ion battery is one of the most promising.

In this context, this master's thesis presents a complete model of Li-ion battery energy storage system (BESS). This model includes the Li-ion battery itself, as well as the different filters, converters and controllers. The emphasis of the model is placed on the dynamic performances in order to study how the designed BESS can help to support a microgrid. On top of that, the robustness of the BESS against grid perturbations is tested as well as power quality considerations. The model was built and tested with Matlab Simulink®. It was also successfully tested on a real-time simulation platform, which validates the feasability of the controllers.

The simulations results show that BESS, thanks to their fast response time, can effictively help to support a microgrid against perturbations. Specifically, the BESS was included in a simple microgrid and tested as a frequency regulation reserve (virtual inertia and primary reserve). Furthermore, with a proper design of filters and controllers, the BESS is robust against harmonics, unbalance and provides good power quality.

Chapter 1

Introduction

1.1 Evolution of Battery Technologies

Batteries provided the main source of electricity before the development of electric generators and electrical grids around the end of the 19th century. Successive improvements in battery technology facilitated the development of other technological advances such as mobile phones, portable computers and electric cars.

The first true battery was invented by the italian physicist Alessandro Volta in 1800. One of the most enduring batteries, the lead-acid battery, was invented in 1859 and is still the technology used to start most internal combustion engines car today. All batteries previously used were primary cells, and so they permanently drained after all their chemical reactions were spent. In 1899, the first nickel-cadmium battery was invented. This technology offers a higher energy density than lead acid. Research on lithium-ion batteries started in the early 20th century, but lithium-ion batteries were first commercialized by Sony in 1991. Since this technology is relatively new, it is expected to be further improved in the future [1].

As for now, lithium-ion batteries are mostly used for small portable technology devices because of their high energy density. Figure 1.1 shows how the different battery technologies compare to each other in terms of density. Lithium-ion batteries are characterized by high specific energy, high efficiency and long life [2]. Even if lithium-ion is the most expensive battery technology, its price has been decreasing since it was first commercialized and is expected to keep decreasing in the future, as shown in Figure 1.3. Meanwhile, the energy density of those batteries has been constantly increasing as shown in Figure 1.2. As a result, Li-ion batteries are now used for larger scale applications such as electric vehicles and even electrical grids.

Most electric vehicles batteries use Li-ion technology. The capacity of those batteries can reach up to 100 kWh. The price of the battery makes up around 35% of the vehicle price [5]. The expected decrease in lithium-ion battery cost should make electric vehicles more affordable in the forthcoming years.The air pollution problem in large urban areas, may be only solved by replacing internal combustion engine (ICE) cars with ideally, zero emission vehicles, i.e. electric vehicles (EVs) or, at least, by controlled emission vehicles, i.e. full hybrid electric vehicles (HEVs) and/or plug-in electric vehicles (PHEVs) [2]. This will also decrease the total CO_2 emission, especially if the electricity is produced with renewable energies.

At the same time, investments for the exploitation of renewable energy resources are increasing worldwide, with particular attention to wind and solar power energy plants, which are the most mature technologies. The intermittence of theses resources requires high energy efficiency storage systems. Batteries can efficiently store and deliver energy on demand in stand-alone power plants, as well as provide power quality and load levelling of the electrical grid in integrated systems [2].

With the improvements of lithium-ion technology, perspectives of using them for grid applications have opened up. As for now, most batteries used in power systems are lead-acid batteries because of the simplicity of the technology and its cost-effectiveness. However, it is a well established technology whose performances have not remarkably improved for a long time. Therefore, future battery research should pay more attention to other types of battery with more potential, such as Li-ion. Currently, cost and safety issues are the two main factors that impede the promotion of Li-ion for widespread use in power systems [6]. In fact, if overheated or overcharged, Li-ion batteries may suffer thermal runaway and cell rupture. In extreme cases, this can lead to combustion. To reduce these risks, Li-ion battery packs contain fail-safe circuitry that disconnects the battery when its voltage is outside the safe range [7].

Possibilities of using batteries of vehicles with electric drive for grid management are considered too. This concept, called *Vehicle-to-grid* (V2G), describes a system in which plug-in electric vehicles, such as EVs and PHEVs, communicate with the power grid to sell demand response services by either returning electricity to the grid or by throttling their charging rate [8]. Since at any given time, about 95 percent of cars are parked, the batteries in electric vehicles could be used to let electricity flow from the car to the electric distribution network and back [9]. This could increase the storage capacity of the grid and raise the economic value of plug-in electric vehicles. This technology is still in its nascent stage and is not widely implemented yet.

Because of the potential improvements of batteries performances and the increasing need for cleaner means of transportation and energy production, batteries will play a crucial role in the energy transition of the 21st century.

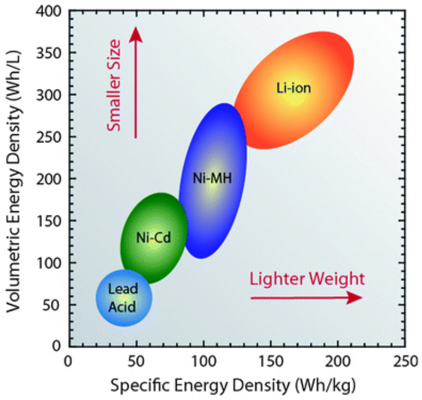

Figure 1.1 – Comparison of energy density (mass and volume) for the main battery technologies (Source : [3])

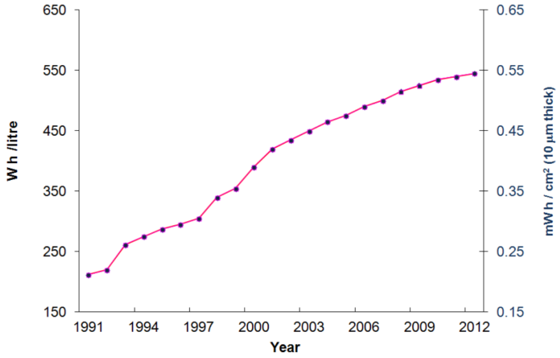

Figure 1.2 – Evolution of lithium-ion batteries energy density (Source : [4])

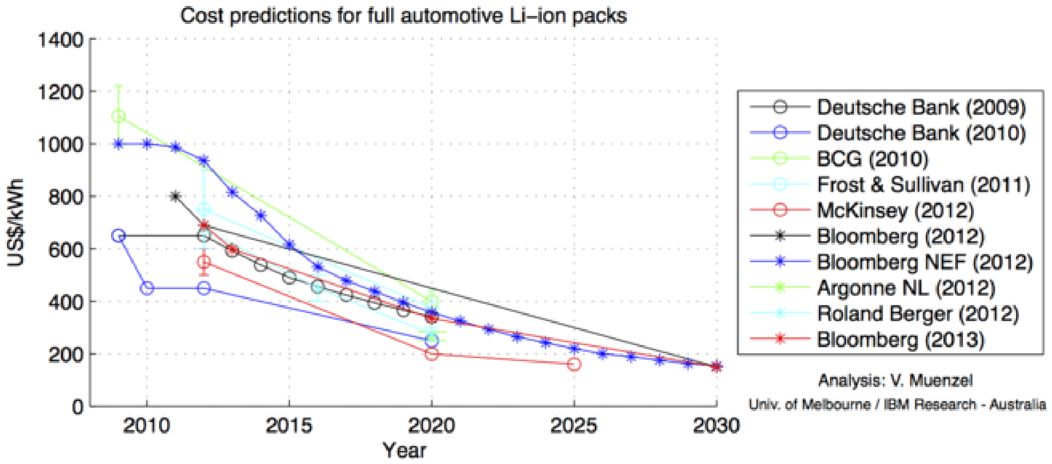

Figure 1.3 – Cost predictions for automotive lithium-ion battery packs

1.2 Microgrids

1.2.1 Concepts of Microgrids

Power generation in the traditional power grid is very centralized, with power flowing unidirectionally from large synchronous generators through a transmission/distribution network to end-users. However, the environmental issues caused by the combustion of fossil fuels have stimulated research and development into new means of producing electricity and organizing the power grid. With the emergence of distributed energy resource (DER) units, e.g., wind, photovoltaic (PV), battery, biomass, micro-turbine, fuel cell, etc., microgrid technologies have attracted increasing attention as an effective mean of integrating such DER units into power systems.

The U.S. Departement of Energy defines a microgrid as "a group of interconnected loads and distributed energy resources within clearly defined electrical boundaries that acts as a single controllable entity with respect to the grid. A microgrid can connect and disconnect from the grid to enable it to operate in both grid-connected or island mode" [10]. The purpose of this concept is to develop a platform that facilitates the integration of distributed generators (DG), energy storage systems (ESS) and loads to ensure that the power grid can supply sustainable, price-competitive and reliable electricity. Figure 1.4 shows a typical microgrid structure with DG sources such as PV systems, wind turbine systems, microturbines and distributed energy storage (DES) facilities such as battery banks, supercapacitors, flywheels, etc. DES play an essential role in microgrids by smoothing the fluctuations of power from the DG units and by improving the stability of the microgrid.

Microgrids can be classified as AC and DC type. Historically, AC has been the choice for over a hundred years due to easy transformation at different voltage levels and power transmission over long distances as well as inherent characteristic from fossil energy driven rotating machines [11]. Since then, the advance in power electronics and the increase in DC loads has made DC power grids an interesting choice. In the traditional AC grid, DC loads are connected to the grid through a AC/DC rectifier. Another posssibility is to have a hybrid AC/DC microgrid as shown in Figure 1.5. This allows to reduce the total number of converters by connecting DC loads to the DC grid and AC loads to the AC grid. The main converter is bidirectional and allows power flow between the AC and DC grids. In grid-tied mode, the AC microgrid is connected to the main utility grid at the point of common coupling (PCC).

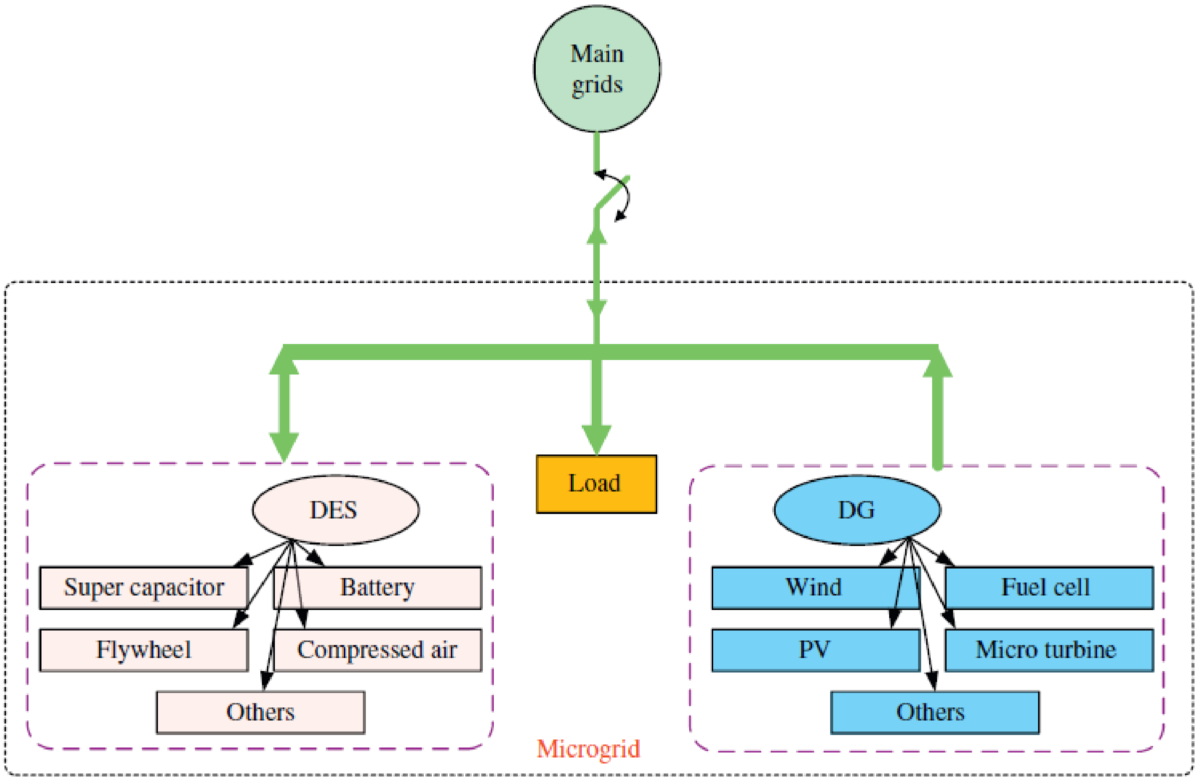

Figure 1.4 – Typical structure of a microgrid (Source : [6])

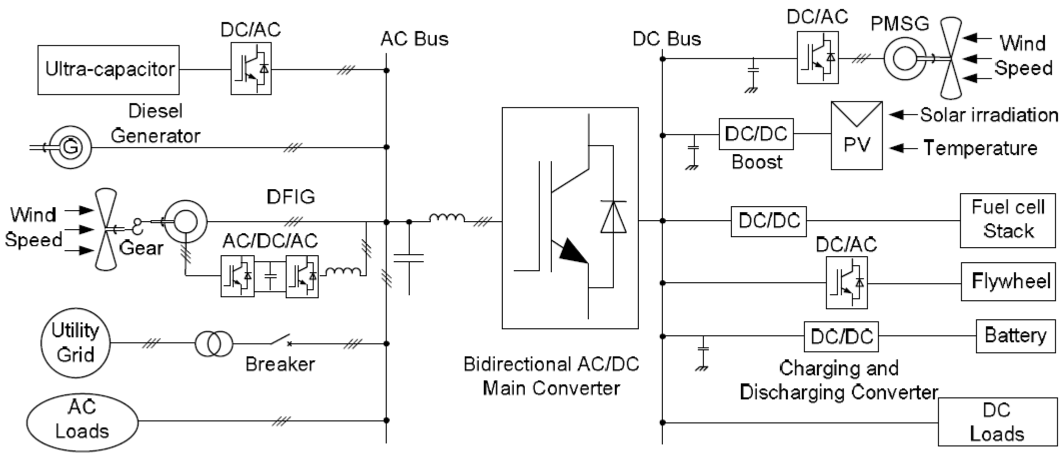

Figure 1.5 – Organisation of a hybrid AC/DC microgrid (Source : [11])

1.2.2 Advantages of Microgrids

As mentioned before, microgrids provide an effective way to integrate small-scale DERs into low voltage distribution network. By increasing the share of sustainable DERs, the dependency on fossil fuel can be reduced along with the carbon and pollution emission. By producing and consuming locally, it can also improve the energy efficiency as the power travels a shorter distance [10].

A microgrid can operate either in grid-connected mode or in island mode. In case of power outage in the main utility grid, a microgrid can then disconnect and provide power for the local loads. It can thus give an improved level of reliability for end-users. Moreover, by using local control of the DG facilities, the power quality can be enhanced and the fluctuations of intermittent sources can be effectively compensated. Promoting customer participation through demand-side management is another way of improving quality and reliability of energy supply. Recent development of Smart Grid technologies take advantage of the progress in electronic communication technology to improve the efficiency of the grid by using features such as demand-side management. Microgrids are an interesting platform to develop the Smart Grid technologies [10].

Finally, in addition to handling locally sensitive loads and the variability of renewable sources, microgrids can also provide ancillary servives to the main utility grid, such as frequency and voltage regulation, black start support and load balancing services. In this way, microgrids represent economic opportunities by compensation of these services to the bulk grid via payments [6].

1.2.3 Challenges for Microgrids

While microgrids and larger integration of DG sources solve a lot of problems, new challenges arise that need to be adressed in order to ensure that the present levels of reliability are not significantly affected and the potential benefits of DG units are fully harnessed. Those are the following :

- **Bidirectional power flows** : While the power only flows unidirectionally from high voltage to low voltage levels in the traditional power grid, the presence of DG units at low voltage can cause reverse power flows which may lead to complications in protection coordination, undesirable power flow patterns, fault current distribution, and voltage control [12].
- **Stability** : Local oscillations may emerge from the interaction of the control systems of DG units, requiring a thorough small-disturbance stability analysis. Moreover, transient stability analysis are required to ensure seamless transition between the grid-connected and stand-alone modes of operation in a microgrid [12].
- **Modeling** : Prevalence of three-phase balanced conditions, primarily inductive transmission lines, and constant-power loads are typically valid assumptions when modeling conventional power systems at a transmission level ; however, these do not necessarily hold valid for microgrids, and consequently models need to be revised [12].
- **Low inertia** : Unlike bulk power systems where high number of synchronous generators ensures a relatively large inertia, microgrids might show a low-inertia characteristic, especially if there is a significant share of power electronic-interfaced DG units. Although such an interface can enhance the system dynamic performance, the low inertia in the system can lead to severe frequency deviations in stand-alone operation if a proper control mechanism is not implemented [12].
- **Uncertainty** : The economical and reliable operation of microgrids requires a certain level of coordination among different DERs. This coordination becomes more challenging in isolated microgrids, where the critical demand-supply balance and typically higher component failure rates require solving a strongly coupled problem over an extended horizon, taking into account the uncertainty of parameters such as load profile and weather forecast. This uncertainty is higher than those in bulk power systems, due to the reduced number of loads and highly correlated variations of available energy resources (limited averaging effect) [12].

1.2.4 Energy Storage Technology in Microgrids

Energy storage technology facilitates high penetration of variable renewable energy resources. ESS has been used for a long time in power systems but the integration of renewable energy increases the demand for ESS. ESS can be divided into mechanical, electrochemical, chemical, electrical and thermal systems, as shown in Figure 1.6.

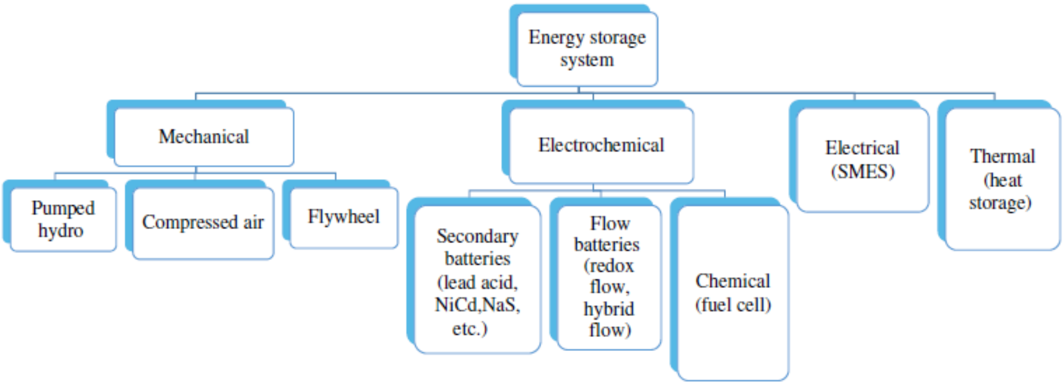

Figure 1.6 – Classification of energy storage systems (Source : Fraunhofer ISE)

The mechanical ESS are :

- **Pumped hydro** : Energy is stored in the form of gravitational potential energy, pumped from a lower elevation reservoir to a higher reservoir. Energy is retrieved by releasing the water from the higher reservoir through a turbine, generating electricity. The reservoirs can either be natural or artificial. As for now, it represents the largest capacity of energy storage technology with 96% of all active tracked storage installations worldwide and a total capacity of 168 GW [13].
- **Compressed air** : Energy is stored by compressing air into a reservoir and is retrieved by expanding the air through a turbine.
- **Flywheel** : A flywheel is a disk with a certain amount of mass that can spin to store energy in kinetic form. In order to minimize friction, a vacuum environment is usually made for the flywheel to spin in to ensure there is no air resistance. Magnetic or electromagnetic bearings can also be used to make the spinning rotor float to make sure there is no contact friction as with mechanical bearings [6].

The electrochemical ESS are :

- **Batteries** : Most batteries are rechargeable batteries, also called secondary batteries. They are composed of one or more electrochemical cells. It accumulates and stores energy through a reversible electrochemical reaction. Several different combinations of electrode materials and electrolytes are used, including lead–acid, nickel-cadmium (NiCd), nickel-metal hydride (NiMH) and lithium-ion (Li-ion).
- **Fuel cells** : This device converts the chemical energy from a fuel into electricity through a chemical reaction of positively charged hydrogen ions with oxygen or another oxidizing agent. Fuel cells are different from batteries in requiring a continuous source of fuel and oxygen or air to sustain the chemical reaction, whereas in a battery the chemicals present in the battery react with each other to generate an electromotive force (emf) [14].

The electrical ESS are :

- **Supercapacitors** : They have much higher capacitance, hence storage capacity, than regular capacitors. Supercapacitors rely on the separation of charge at an electric interface that is measured in fractions of a nanometer, compared with micrometers for most polymer film capacitors. Energy storage is by means of static charge rather than of an electrochemical process inherent to batteries [15].

- **Superconducting Magnetic Energy Storage** (SMES) : The basis of SMES is the storage of energy in the magnetic field of a DC current flowing in superconducting coils. Energy losses are effectively zero because superconductors offer no resistance to electron flow [15].

Large difference of characteristics exists among different types of ESS. Thus, the best energy storage type should be chosen according to the practical microgrid application under consideration. Figure 1.7 shows the applicable power ranges and discharge power duration of the different energy storage technologies.

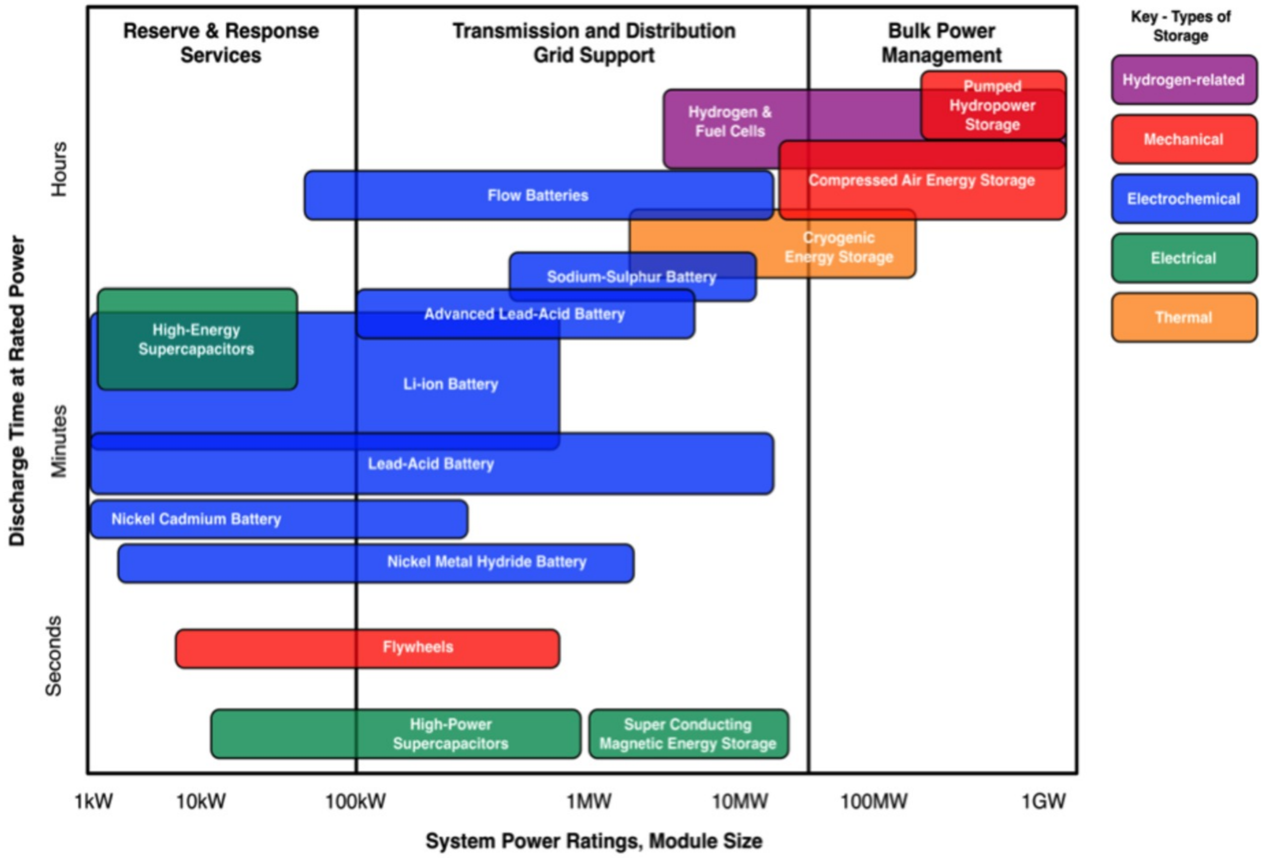

Figure 1.7 – Applicable power range and discharge power duration of different energy storage technologies (Source : [16])

1.3 Simulink Model and Real-time Simulations

The model presented in Chapter 2 was implemented and tested in Simulink®. This model was built upon the work performed during an internship at ENGIE Lab Laborelec (Linkebeek) [1]. Laborelec is a leading expertise and research centre in electrical power technology and is active on the whole electricity value chain, i.e. transmission, distribution, storage and final use. A first operational model was achieved by the end of the internship and this model was then improved for this master's thesis. The Simulink® model will be used by Laborelec in some of their future projects. Therefore, it is important to make sure it is readable for people who did not take part in its realisation. The model is structured in sub-blocks, each of them being a functional part of the system. The different functional parts of the battery system are clearly defined in Chapter 2. This type of structure is chosen for the following reasons :

---

[1] It will be refered as *Laborelec* from now on.

- It improves the readability of the model. Above a certain level of complexity, a Simulink® model can quickly become incomprehensible, especially for someone who did not take part in its realisation. This structure allows someone to use a sub-block as a *black box*, i.e. without having to fully understand how it works. However, each sub-block has to be documented so that the user can comprehend how they operate, if desired.
- This structure also makes it possible for someone to extract a sub-block and use it for a different applications. Hence, this model enlarges the Simulink® sub-blocks *library* of Laborelec.

In addition to the Simulink® tests, the model was simulated in a real-time environment. Laborelec is in possession of a real-time simulator, called *PHIL* (Power Hardware In the Loop). The PHIL works with a software named RT-Lab®. RT-Lab® is a toolbox that, with some adaptations, allows to run a Simulink® model in real-time.

Figure 1.8 illustrates the difference between offline and real-time simulation. During a discrete-time simulation, the amount of real time required to compute all equations representing a system during a given time step may be shorter or longer than the duration of the simulation time step. Figure 1.8 a) and b) respectively represent those two possibilities. These two situations are referred to as offline simulation. Considering the simulation uses fixed-size time steps, the moment at which a result becomes available is irrelevent. Conversely, during real-time simulation, the accuracy of computations not only depends upon precise dynamic representation of the system, but also on the length of time used to produce results. If simulator operations are not all achieved within the required fixed time-step, the real-time simulation is considered erroneous. This is commonly known as an *overrun* [17].

Figure 1.8 c) illustrates the chronological principle of real-time simulation. For a real-time simulation to be valid, the real-time simulator used must accurately produce the internal variables and outputs of the simulation within the same length of time that its physical counterpart would. This permits the real-time simulator to perform all operations necessary to make a real-time simulation relevant, including driving inputs and outputs (I/O) to and from externally connected devices. In this way, hadrware can be integrated in the loop an be part of the real-time simulation. Running the battery model in real-time also validates the feasability of the controllers developed in this thesis. In fact, if the model can work without overruns, the designed controllers can be implemented and integrated in a physical system.

In order for the battery model to run without overruns, its computational cost had to be restrained. Threrefore, two models were developed for each converter (DC/DC and DC/AC, refer to Chapter 2) :

- A *full model* where the switching devices of the converter are represented. Hence, this model has to be simulated with a relatively small time step.
- An *average dynamic model* where the currents and voltages are averaged over one switching period of the converter. In this way, the dynamics in the time order of a switching period is not represented but the slower dynamics is modelled. The time step used can then be larger.

The real-time simuations were successfully performed with the average dynamic models.

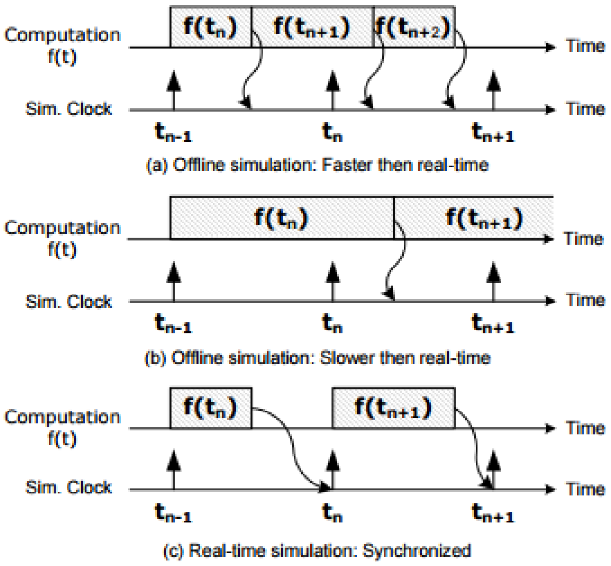

Figure 1.8 – Comparison between offline and real-time simulation (Source : [17])

In addition to that, it was initially planned to run some hardware tests as part of this thesis. Laborelec owns a SAFT Li-ion battery which is adapted for power systems. Due to several setbacks, no tests could be carried out in time to validate the model. However, Laborelec had previously tested the battery to evaluate its general characteristics. Some of the numerical values used to test the model with Simulink® are based on the given characteristics of this SAFT battery.

In the future, Laborelec will further validate and use this model as part of projects they are involved in and integrate it in their real-time simulations. For example, *ELECTRA Web-of-cells* is an European project in which Laborelec takes part with many other laboratories. The goal of this project is to study the concept of Web-of-Cells which is a decentralized real-time control concept, where the power system is divided in small cells, and where the need for reserves activations as well as the activations themselves are dealt with in a decentralized manner by cell system operators [18]. This decentralized scheme aims to ancipate the new challenges for power systems :

- More generation from intermittent renewable energy resources resulting in generation forecast errors and reduced generation dispatchability
- More distribution grid connected generation inducing reverse powerflows instead of downstream power distribution, congestions and voltage problems
- Increase of elctrical loads due to electrification of heating and transport

Chapter 2

Model of a Li-ion Battery Energy Storage System

2.1 Overview

Before going into the details of each component of a BESS, it is important to have a view of its overall structure, represented in Figure 2.1. The elements composing the battery-side of the system are the following :

- **Li-ion battery & BMS** : A battery is the assembly of electrochemical cells mounted in series and in parallel. The BMS (Battery Management System) coordinates the interactions of all the cells of a battery and gives information about the state of the battery [19]. A BESS can be composed of one or multiple battery packs, each one having its own BMS.
- **DC/DC converter** : This converter allows the power to flow from the battery to the DC bus or the other way around. Hence, it must be bidirectional. The battery is usually at lower voltage than the DC bus.
- **Battery-side controller** : This controller acts on the DC/DC converter to regulate the power flowing from/into the battery.

The DC bus is formed of a large capacitance. The voltage is controlled to be kept at a reference value such that the BESS can be connected to the grid through an AC/DC converter, despite the voltage variations at the ouptput of the battery. In fact, the DC bus capacitor acts as a filter. Other utilities such as PV panels or wind turbines can be connected to the same DC bus.

The elements composing the grid-side of the system are the following :

- **DC/AC converter** : The DC/AC converter connects the DC bus to the AC grid. In the case of a BESS, this converter also has to be bidirectional.
- **Grid-side controller** : This controller acts on the DC/AC converter to regulate the DC bus voltage and consequently the power flowing from/into the grid.

The system has to be modelled with a certain level of accuracy and complexity. When doing a model for simulations, there is always a trade-off between :

- A complex model that depicts accurately the physical phenomena
- A simple model that has a low simulation cost

Before going into the precise modelling of the different parts of the system, it is important to define the scope of the model in order to make the right hypothesis. The purpose of the model is to examine the interactions between a Li-ion BESS and a microgrid and more specifically how the BESS affects the reliability and quality of the power delivered in the microgrid. The perturbations that a microgrid has to face can occur in a short time lapse. For instance, a voltage dip can be as short as one half-cycle (10 ms) [20]. Thus, the model has to emphasize the fast dynamic performances and the power quality impact of the BESS and hypothesis for the model have to be chosen accordingly.

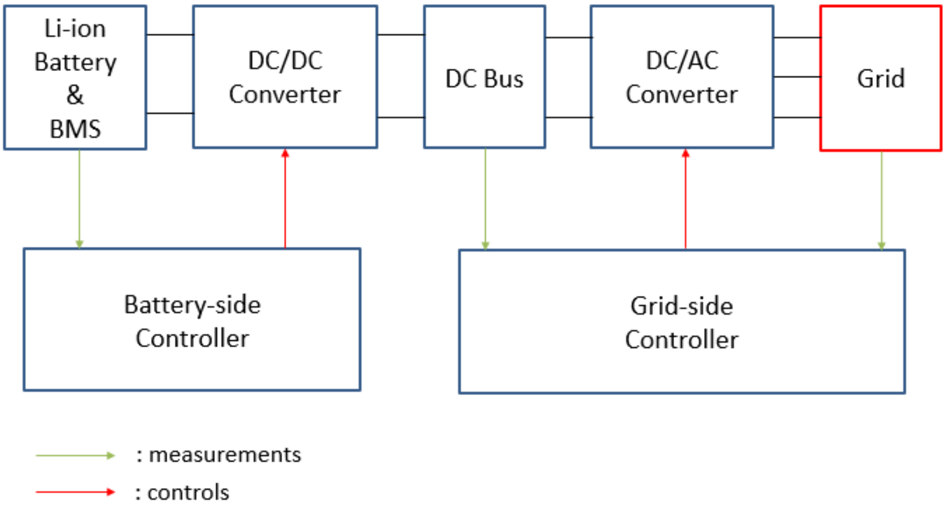

Figure 2.1 – Overall simplified structure of a BESS connected to an AC grid

2.2 Li-Ion Battery & BMS

2.2.1 Li-ion Cell : Principle of Operation

Like any other battery, a rechargeable lithium-ion battery is made of one or more power-generating compartments called cells. Each cell has essentially three components : a positive electrode, a negative electrode and a chemical called an electrolyte in between them. The positive electrode is typically made from a chemical compound called lithium-cobalt oxide (LiCoO2) or, in newer batteries, from lithium iron phosphate (LiFePO4). The negative electrode is generally made from carbon (graphite). The composition of the electrolyte varies from one type of battery to another but doesn not influence the working principle of the cell [22].

All lithium-ion batteries work in broadly the same way. When the battery is charging up, as shown in Figure 2.2, the lithium-cobalt oxide positive electrode gives up some of its lithium ions, which move through the electrolyte to the negative, graphite electrode and remain there. The battery takes in and stores energy during this process. When the battery is discharging, as shown in Figure 2.3, the lithium ions move back across the electrolyte to the positive electrode, producing the energy that powers the battery. In both cases, electrons flow in the opposite direction to the ions around the outer circuit. The electrolyte provides a conductive medium for lithium ions to move between the electrodes but the electrons do not flow through the electrolyte : it is effectively an insulating barrier, as far as electrons are concerned [22]. Both electrodes allow lithium ions to move in and out of their structures with a process called *insertion* (*intercalation*) or *extraction* (*deintercalation*), respectively.

The chemical reactions occuring at both electrodes are called *redox* (*reduction-oxidation*) reactions. Reduction and oxidation reactions are defined as follows :

- **Oxidation** is the loss of electrons or an increase in oxidation state by a molecule, atom, or ion.
- **Reduction** is the gain of electrons or a decrease in oxidation state by a molecule, atom, or ion.

The positive (cathode) electrode half-reaction in the lithium-doped cobalt oxide substrate is (left : reduction, right : oxidation) [23]:

$$CoO_2 + Li^+ + e^- \rightleftharpoons LiCoO_2$$

The negative (anode) electrode half-reaction for the graphite is (left : oxidation, right : reduction) :

$$LiC_6 \rightleftharpoons C_6 + Li^+ + e^-$$

The full reaction (left : charge, right : discharge) being :

$$LiC_6 + CoO_2 \rightleftharpoons C_6 + LiCoO_2$$

The net electromotive force of the full reaction is the difference between the reduction potentials of both half-reactions. The emf of a cell depends thus on the chemical reactions of its electrodes and electrolytes. Alkaline and zinc–carbon cells have different chemistries, but approximately the same emf of 1.5 volts; likewise NiCd and NiMH cells have different chemistries, but approximately the same emf of 1.2 volts. The high electrochemical potential changes in the reactions of lithium compounds give lithium cells emfs of 3 volts or more [24].

The electrical driving force ΔV_{bat} across the terminals of a cell is known as the *terminal voltage* (difference) and is measured in volts. The terminal voltage of a cell that is neither charging nor discharging is called the open-circuit voltage and equals the emf of the cell. Because of internal resistance, the terminal voltage of a cell that is discharging is smaller in magnitude than the open-circuit voltage and the terminal voltage of a cell that is charging exceeds the open-circuit voltage.

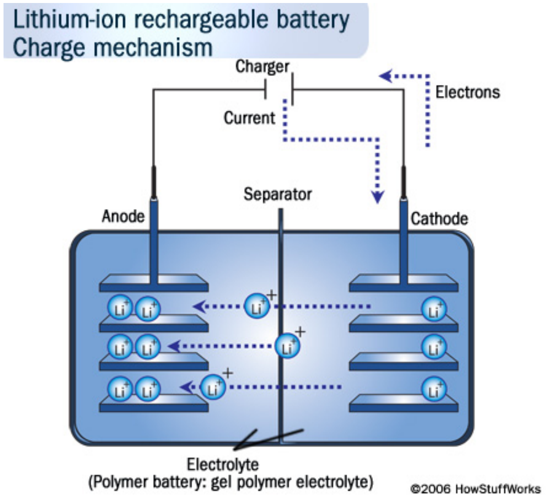

Figure 2.2 – Li-ion cell charging mechanism (Source : [21])

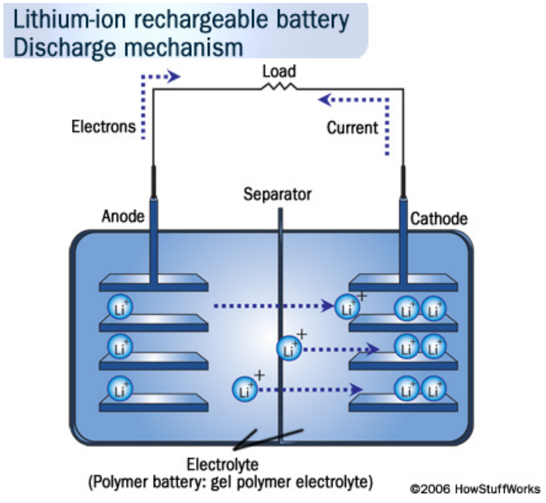

Figure 2.3 – Li-ion cell discharging mechanism (Source : [21])

2.2.2 Battery Management System

A *battery* or *battery pack* is a collection of cells which are ready for use, as it contains an appropriate housing, electrical interconnections, and possibly electronics to control and protect the cells from failure. The term *module* is often used as an intermediate topology , with the understanding that a battery pack is made of modules, and modules are composed of individual cells [25].

The BMS is required to coordinate the operation of the cells forming the battery. In fact, a battery is indissociable from its BMS as it cannot work properly without it. The objective of the BMS is to provide protection, increase the lifespan and maintain the stability of the batteries in the BESS. In order to accomplish these tasks, the BMS should have the functions of monitoring, computation, control and communication [6].

To protect the batteries from damage and maintain them in good condition, the BMS needs to monitor the temperature, voltage and current in the battery. Overheating the battery is very dangerous, and may lead to explosion and fire. Hence, temperature monitoring is very important to ensure that the batteries work in stable conditions.

The BMS has to perform computations such as the state-of-charge (SOC) and state-of-health (SOH) of the battery based on the voltage and current measurements. The SOC corresponds to the energy stored by the battery over the total energy it is able to store. The SOH is a figure of merit of the condition of a battery compared to its initial conditions. The definition of the SOH is more ambiguous as the designer decides how it is computed. The estimation of the SOH usually depends on several measurements such as internal resistance, capacity, number of charge/discharge cycles and voltage with an arbitrary weight for each parameter [26].

The monitoring of the SOC allows to control the current accordingly so that overcharging or over-discharging can be prevented. Furthermore, the current of batteries should stay in a safe range, especially during the charging process. If the charging current is too high, it will not only damage the battery's health, but also causes accidents. The BMS has to be coordinated with the DC/DC converter as it controls the charging/discharging current.

Another responsibility of the BMS is to ensure *cell balancing*. In each battery package, several battery cells are connected in series to achieve a bigger capacity. However, the quality or ability of each battery cell is not identical, which may result in imbalance among cells during charging or discharging. The imbalance among battery cells decreases the available energy of the overall battery package. Due to the safe range requirement of the battery's SOC, it stops charging or discharging when one of the cells reaches the limits. Therefore, for the unbalanced situation, the battery package will not continue to charge or discharge when the battery cell with the highest SOC reaches the upper limit or the battery cell with lowest SOC reaches the lower limit. One technique commonly used is called *passive cell balancing*. As shown in Figure 2.4, the BMS commands field-effect transistors so that the cells with higher SOC recharge the cells with lower SOC [6].

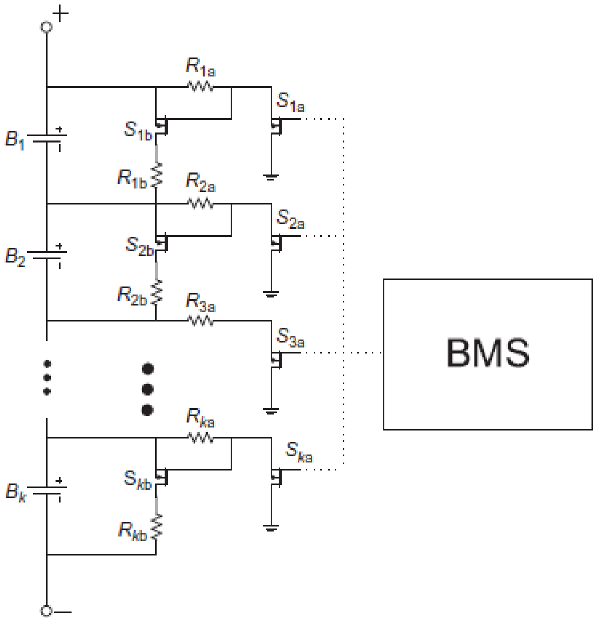

Figure 2.4 – Passive cell balancing BMS (Source : [6])

2.2.3 Equivalent Model

The goal of the model is to capture the characteristics of real-life batteries and predict their behaviour under various operating conditions. Different types of models can be used with different levels of accuracy.

Electrochemical models [27] can fully describe the behaviour of a battery with equations that capture the chemical phenomena occuring in the battery. However, these models are typically computationally time-consuming due to a system of coupled time-varying partial differential equations. Such models are best suited for optimization of the physical design aspects of electrodes and electrolyte [28].

Mathematical models [29] use stochastic approaches or empirical equations which can predict runtime, efficiency and capacity. However, these models are inaccurate (5-20% error) and have no direct relation between model parameters and the I-V characteristics of batteries. As a result, they have limited value in circuit simulation software [28] and consequently for grid applications.

Electrical models are the most intuitive for use in circuit simulation. The battery can be represented as an equivalent circuit where the number of elements in the circuit defines the complexity of the model. The use of RC parallel networks allows to model with accuracy the dynamic behaviour of the battery. However, electrical models are not the best at evaluating the runtime and the SOC of the battery. The emphasis of this model is intentionally placed on the dynamic performances.

The electrical model used is represented in Figure 2.5. The choice is to use two RC parallel networks in addition to the constant resistance R_{series} and the voltage source V_{oc} which corresponds to the open-circuit voltage of the battery. The first parallel $R_{t,s}C_{t,s}$ network models the faster transient of the battery with a time constant τ_{sec} in the order of one second [28]. The second parallel $R_{t,m}C_{t,m}$ network models the slower transient of the battery with a time constant τ_{min} in the order of one minute [28]. Some articles [28, 30] use additional RC networks with longer time constants (more than one hour) but it is not necessary for the aimed application ; using two RC networks is a good trade-off between precision and computational cost. The open-circuit voltage as well as the resistances and capacitances depend on the SOC.

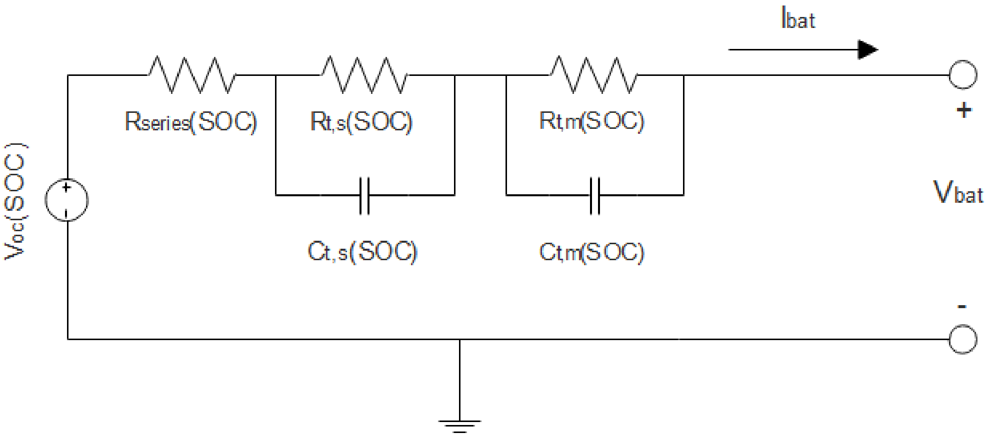

Figure 2.5 – Electrical model of a Li-ion battery

The parameters of the model are as follows :

V_{bat}	Battery output voltage [V]
V_{oc}	Battery open-circuit voltage [V]
Z_{eq}	Equivalent parasitic impedance [Ω]
I_{bat}	Battery current[A]
SOC	State-of-charge [/]
SOC_{init}	Initial state-of-charge [/]
C_{bat}	Battery capacity [A s]

where Z_{eq} is the sum of R_{series} and the two RC networks. The equations of the model are the following :

$$SOC(t) = SOC_{init} - \int_0^t \frac{I_{bat}(t)}{C_{bat}} \tag{2.1}$$

$$V_{bat} = V_{oc} - I_{bat} Z_{eq} \tag{2.2}$$

where I_{bat} is positive if the battery is discharging and negative if charging. The relations between the parameters and the SOC also have to be determined to complete the model. The choice made in Article [28] is to use polynomial functions of 6^{th} order. For instance, the relation between V_{oc} and SOC is :

$$V_{oc} = A_0 \ + \ A_1 \cdot SOC \ + \ A_2 \cdot SOC^2 \ + \ ... \ + \ A_6 \cdot SOC^6 \tag{2.3}$$

The same type of relation is used for the resistances and capacitances. All the coefficients of the polynomial functions are determined experimentally.

A few assumptions are made for the model, for the sake of simplicity and based on the aimed application for the model :

- The effect of *capacity fading* is neglected. Capacity fading refers to the irreversible loss of usable capacity of a battery due to time, temperature and cycle number. Generally, a battery is considered to be usable until reaching 70% of its initial capacity. This point is reached after roughly 2000 Full Equivalent Cycles (FEC) for Li-Ion batteries used in EV or ESS [32]. Considering the goal of the model is to study the relatively fast dynamics of a battery, it is a reasonable assumption to neglect this long term effect. The capacity of the battery is thus considered to be constant during the simulation.

- The effect of temperature is also neglected which is equivalent to considering that the temperature is constant. In addition to influencing the lifetime of the battery, temperature has an effect on the open-circuit voltage V_{oc}. The temperature of the battery pack is controlled by its cooling system. The operation of most Li-ion cell is limited to a temperature of 20°C to 40°C [31]. Figure 2.6 shows that higher temperature causes very little alteration on a typical Li-ion cell compared to room temperature.
- The effect of self-discharge is neglected. This effect causes the SOC decrease even when the battery is in off-mode. For Li-ion, the energy loss is typically asymptotical, with 5% in 24h after charge and then 1-2% per month (plus 3% for safety circuit) [33].

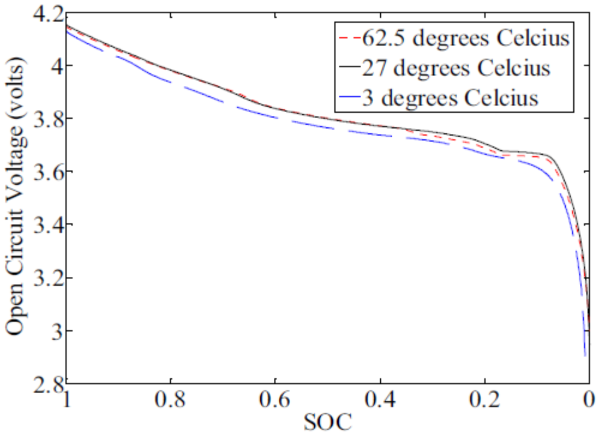

Figure 2.6 – Open-circuit voltage V_{oc} of a Li-ion cell vs SOC for different temperatures (Source : [28])

The efficiency of the battery is taken into account through the resistors of the model as they dissipate power. The BMS also intervenes, in cooperation with the DC/DC converter, in the behaviour of the battery. The BMS limits the maximal charge/discharge current of the battery. It also takes control of the current when the SOC is about 90% or 10% to avoid overcharge/over-discharge [6].

2.2.4 Example and Tests

As mentioned in Section 1.3, it was initially planned to perform experimental tests on a SAFT Li-ion battery to identify the parameters of the model. However, due to several setbacks, these tests could not be carried out. From then on, the results obtained in Article [28] (quoted 269 times) are utilized to build a realistic battery model, as it is one of the few articles who analyzes thoroughly the fast dynamic characteristics of Li-ion batteries. This article identifies the parameters for a single Panasonic CGR18650A Li-ion cell. The specifications of this cell are given in Table 2.1 [34].

Nominal Voltage	3.7 V
Capacity	2.2 Ah
Max. charge current	1.5 A (0.7 C[1])
Max. discharge current	2.2 A (1 C)

Table 2.1 – Specifications of a Panasonic CGR18650A Li-ion cell

---

[1] Currents for batteries are often expressed in C-rate where 1C corresponds to the current that the battery can provide during 1 hour

From there, the battery pack with the desired nominal voltage and capacity can be built by mounting $n_{parallel}$ branches in parallel, each one containing n_{series} cells in series. For a battery with a nominal voltage $V_{nom} = 430$ V and a capacity of $C_{bat} = 34$kWh, the specifications are given in Table 2.2 [2].

n_{series}	116
$n_{parallel}$	36
Nominal Voltage	430 V
Capacity	34kWh
Max. continuous charge current	56 A (0.7 C)
Max. continuous discharge current	80 A (1 C)
Nominal power	25kW (0.7 C)

Table 2.2 – Specifications of a 25kW/34kWh Li-ion battery

On the basis of the data given in Article [28] for one Li-ion cell, the coefficients of the polynomial functions (Eq 2.3) can be computed for the whole battery pack. The resulting functions are shown in Figures 2.7-2.10.

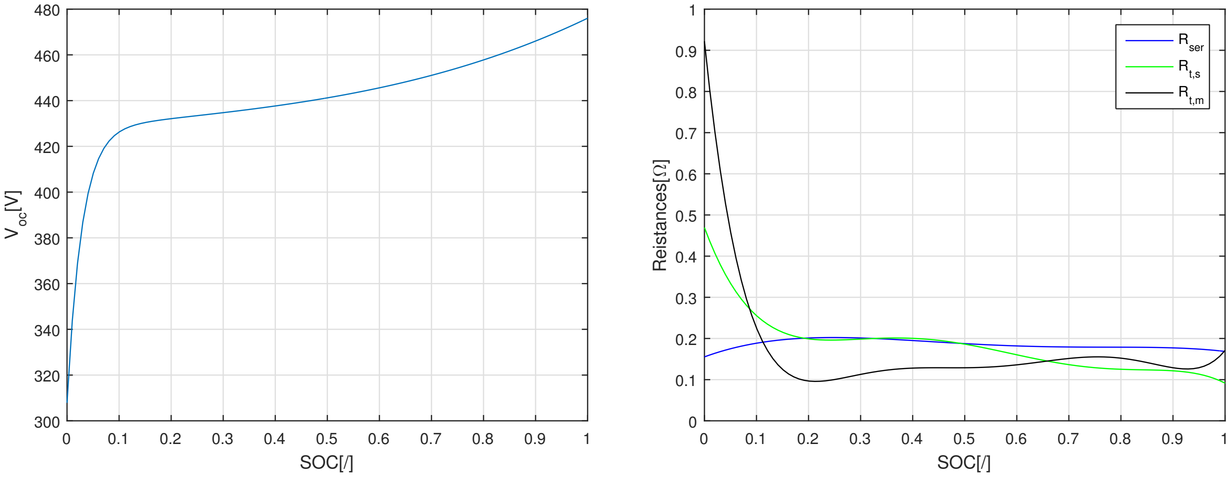

Figure 2.7 – V_{oc} vs SOC

Figure 2.8 – R_{ser}, $R_{t,s}$ & $R_{t,m}$ vs SOC

---

[2] These specifications correspond roughly to those of the SAFT Li-ion battery used by ENGIE Lab Laborelec (Linkebeek) for grid applications

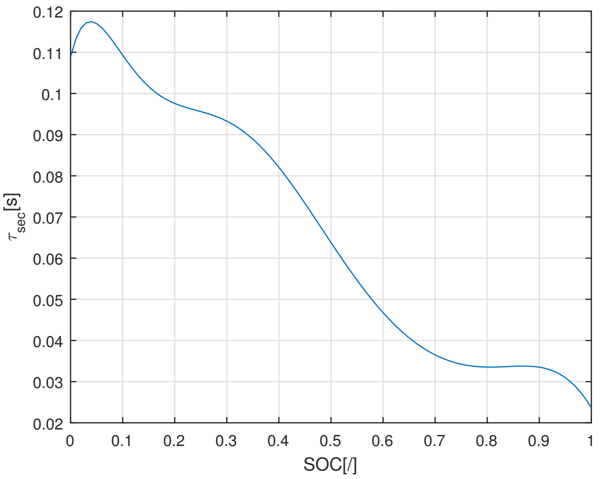

Figure 2.9 – $\tau_{sec} = R_{t,s}C_{t,s}$ vs SOC

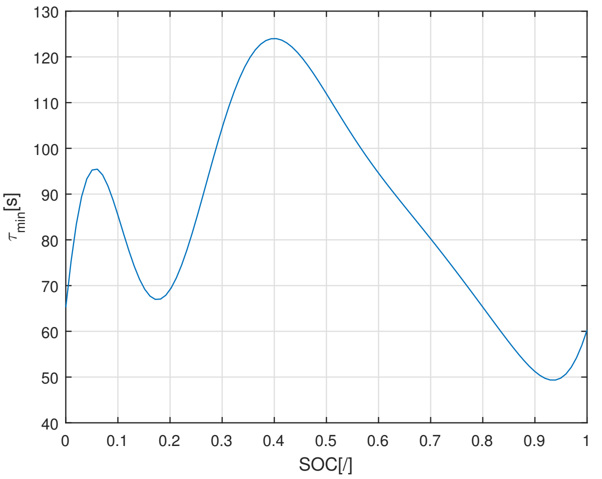

Figure 2.10 – $\tau_{min} = R_{t,m}C_{t,m}$ vs SOC

Figure 2.11 shows the response of the battery to a 1 second pulse of current. The instantaneous voltage drop is the one across R_{series} and the effect of τ_{sec} is visible. Figure 2.12 shows the response of the battery to 1 minute pulse of current where the effect of τ_{min} is visible.

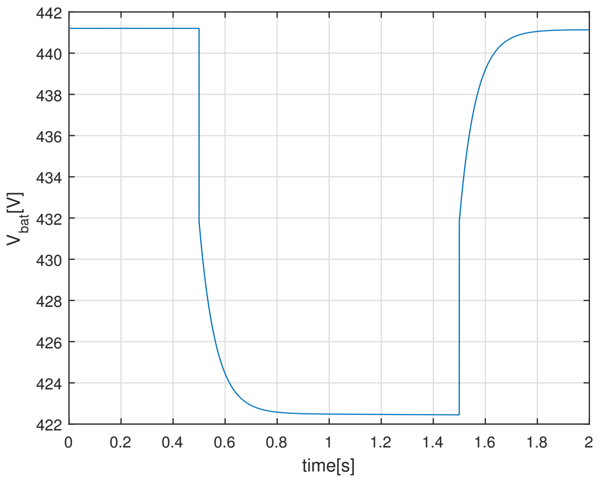

Figure 2.11 – V_{bat} for a 1 second pulse of 50A (discharging, SOC=50%)

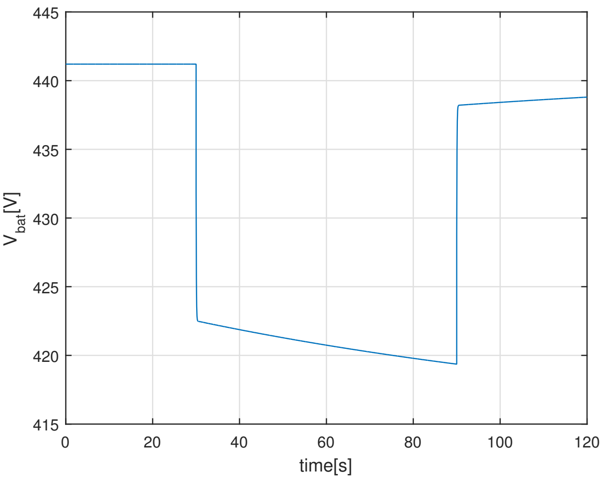

Figure 2.12 – V_{bat} for a 1 minute pulse of 50A (discharging, SOC=50%)

2.3 DC/DC Converter and Battery-side Controller

2.3.1 Topology

The role of the DC/DC converter is to allow bidirectional power transfer between the battery and the DC bus. Usually, the battery is at a lower voltage (LV) and the DC bus at higher voltage (HV). The different components of a bidirectional DC/DC converter with galvanic isolation are depicted in Figure 2.13 :

- The port 1 and port 2 filter networks provide smooth terminal voltages and currents. For each filter network, at least a single capacitor or a single inductor is employed [35].
- The DC/AC converter is a switch network which provides AC power to the HF transformer and the AC/DC converter supplies DC power to the receiving port ; both convert-

ers must allow for bidirectional power transfer. Typically, full bridge circuits, half-bridge circuits, and push-pull circuits are employed. However, different solutions (e.g. the single switch networks used in a bidirectional flyback converter) are reported, as well [35, 36].

- The reactive HF networks provide energy storage capability within the HF AC part. Even if these parts are not necessarily required for a fully functional bidirectional DC/DC converter, they will always be present in practice due to the parasitic components of the HF transformer (e.g. stray and magnetizing inductances, parasitic capacitances) [35].
- The HF transformer is required in order to achieve electric isolation; it further enables large voltage and current transfer ratios. The HF transformer is considered superior over a low frequency transformer, since transformer and filter components become smaller (and often less expensive) at higher frequencies. However, increasing the switching frequency increases the switching losses in the semiconductors [35].

Figure 2.13 – General topology of an isolated, bidirectional DC–DC converter (Source : [35])

Port 1 will be referenced as LV side and port 2 as HV side.
The topology chosen is the Dual Active Bridge (DAB) converter, shown in Figure 2.14. This DAB converter has a symmetrical topology with two full bridges on each side of the HF transformer. Half-bridges or push-pull circuits can be used instead of full bridges, depending on the desired efficiency, cost and power density. For example, half-bridges are cheaper because they use twice as less semiconductors but have lower efficiency because the RMS current through the semiconductors is doubled which multiplies the conducting losses by 4 in each semiconductor. More generally, other topologies of bidirectional DC/DC converters are viable but DAB converter with full bridges is a good compromise between power density, efficiency and cost [35]. The reactive power network simply consists of an inductor L connected in series with the HF transformer. In practice, L is the result of an additional inductance added to the transformer stray inductance.
The switching devices can either be MOSFETs or IGBTs, depending on the required breakdown voltages, power and switching frequency (Figure 2.15). IGBTs are preferred for applications with output power higher than 5kW [37]. The antiparallel diodes can conduct the inductor current when all the switches are off. They can also conduct reverse current in the case of unidirectional switches such as IGBTs.

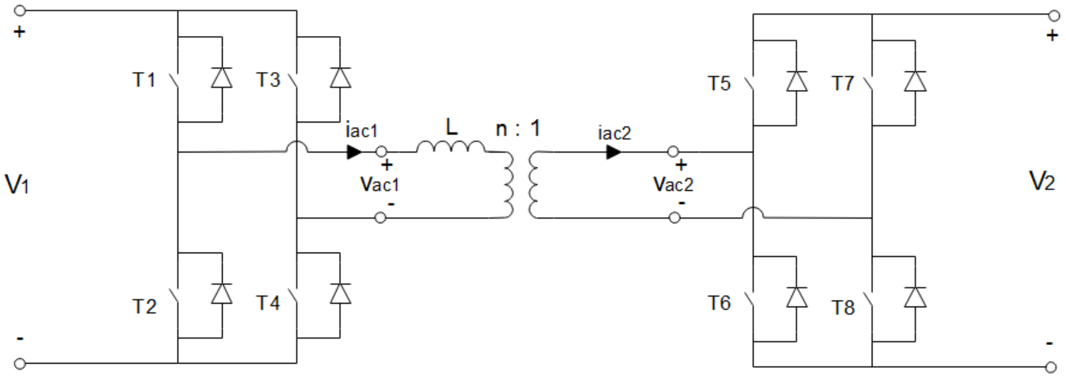

Figure 2.14 – Dual Active Bridge (DAB) converter topology

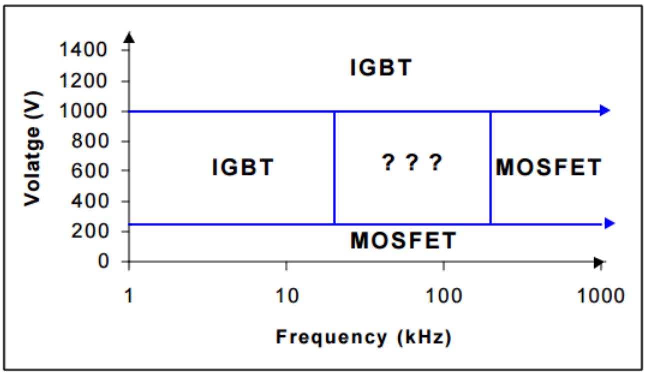

Figure 2.15 – Where MOSFETs and IGBTs are preferred, not counting output power (Source : [37])

2.3.2 Lossless DAB Model

The full bridges can replaced by time varying voltage sources v_{AC1} and v_{AC2} to form the lossless DAB model shown in Figure 2.16. The assumptions of the lossless DAB model are the following [35]:

- All losses are neglected ; ideal switches are thus considered.
- The transformer magnetizing inductance and parasitic capacitances (e.g. transformer coupling capacitance between LV and HV sides) are neglected.
- All HV side (secondary) quantities are referred to the LV side (primary).
- Constant supply voltages V_1 and V_2 are considered.

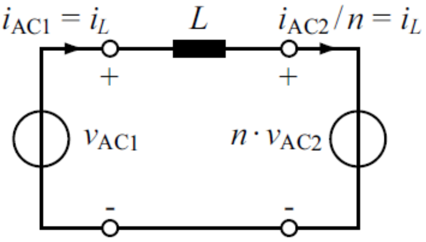

Figure 2.16 – Lossless DAB Model (Source : [35])

With the LV side full bridge, three different voltage levels are possible for $v_{AC1}(t)$ (see Figure 2.14):

$$v_{AC1}(t) = \begin{cases} +V_1 & \text{for state I : } \mathrm{T}_1, \mathrm{T}_4 \text{ on, } \mathrm{T}_2, \mathrm{T}_3 \text{ off} \\ 0 & \text{for state II : } \mathrm{T}_1, \mathrm{T}_3 \text{ on, } \mathrm{T}_2, \mathrm{T}_4 \text{ off or} \\ & \text{for state III : } \mathrm{T}_2, \mathrm{T}_4 \text{ on, } \mathrm{T}_1, \mathrm{T}_3 \text{ off} \\ -V_1 & \text{for state IV : } \mathrm{T}_2, \mathrm{T}_3 \text{ on, } \mathrm{T}_1, \mathrm{T}_4 \text{ off} \end{cases} \tag{2.4}$$

Similarly, $v_{AC2}(t)$ is equal V_2, 0, or $-V_2$ depending on the switching states of T_5, T_6, T_7 and T_8. The resulting voltage across inductor L is :

$$v_R(t) = v_{AC1}(t) - n \cdot v_{AC2}(t) \tag{2.5}$$

This voltage generates the current

$$i_L(t_1) = i_L(t_0) + \frac{1}{L}\int_{t_0}^{t_1} v_R \, dt \tag{2.6}$$

at the time t_1, starting with inital current $i_L(t_0)$ at time t_0. The voltage sources v_{AC1} and v_{AC2} thus generate or receive the respective instantaneous powers

$$p_1(t) = v_{AC1}(t) \cdot i_L(t) \qquad \text{and} \qquad p_2(t) = v_{AC2}(t) \cdot i_L(t) \tag{2.7}$$

The average power for one switching cycle $T_s = 1/f_s$ is

$$P_1 = \frac{1}{T_s} \int_{t_0}^{t_0+T_s} p_1(t)dt \tag{2.8}$$

for the LV side and

$$P_2 = \frac{1}{T_s} \int_{t_0}^{t_0+T_s} p_2(t)dt \tag{2.9}$$

for the HV side. Moreover, since the model is lossless :

$$P_1 = P_2 \tag{2.10}$$

The power level of the DAB converter is typically adjusted using one or more out of the 4 control parameters which are [35]:

- the phase shift, φ, between $v_{AC1}(t)$ and $v_{AC2}(t)$ with $-\pi < \varphi \leq \pi$
- the duty cycle, D_1, of v_{AC1} with $0 \leq D_1 \leq 1/2$
- the duty cycle, D_2, of v_{AC2} with $0 \leq D_1 \leq 1/2$
- the switching frequency f_s

The simplest and most common modulation principle of a DAB converter, called *phase shift modulation*, is considered here. It operates with constant switching frequency and maximum duty cycles, $D_1 = D_2 = 1/2$; it solely varies the phase shift φ in order to control transferred power. Hence, $v_{AC1}(t)$ is either $+V_1$ or $-V_1$ and $v_{AC2}(t)$ is either $+V_2$ or $-V_2$ as shown in Figure 2.17. In practice, as semiconductors have a finite switching time, D_1 and D_2 have to be slightly smaller than 1/2 to make sure that no arm of the bridges is short-circuited. However, considering that $D_1 = D_2 = 1/2$ simplifies the following calculations.

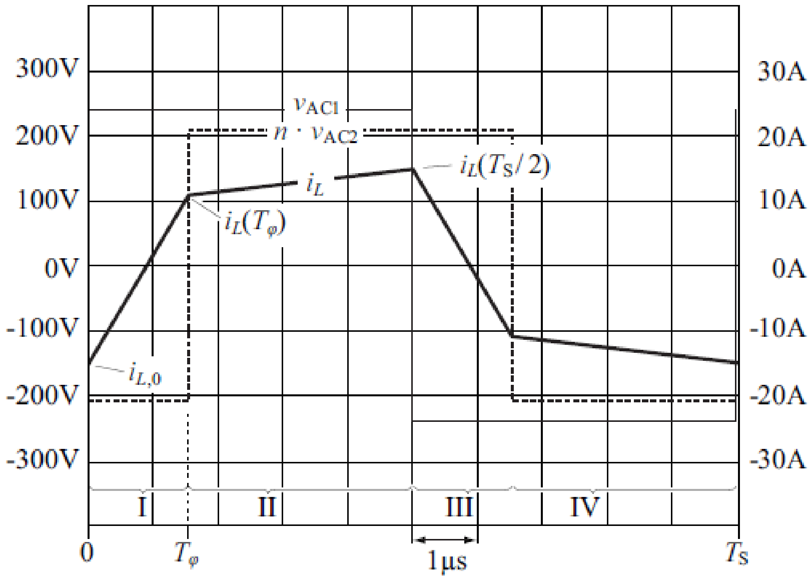

Figure 2.17 – Example of transformer voltages and inductor current waveforms with phase shift modulation (Source : [35])

During steady-state operation, the voltages $v_{AC1}(t)$ and $v_{AC2}(t)$ and the inductor current repeat every half-cycle with reversed signs :

$$\begin{cases} v_{AC1}(t+T_s/2) = -v_{AC1}(t) \\ v_{AC2}(t+T_s/2) = -v_{AC2}(t) \\ i_L(t+T_s/2) = -i_L(t) \end{cases} \tag{2.11}$$

Therefore, only the first half-cycle (intervals I and II in Figure 2.17) has to be considered for the calculation of the transferred power. With $t_0 = 0$ (2.8), we have

$$P_1 = \frac{1}{T_s}\int_0^{T_s} p_1(t)dt = \frac{2}{T_s}\int_0^{T_s/2} v_{AC1}(t) \cdot i_L(t)dt = \frac{2V_1}{T_s}\int_0^{T_s/2} i_L(t)dt \tag{2.12}$$

where t_0 is such that $v_{AC1}(t) = V_1$ during the whole half-cycle. In order to obtain an analytical expression for P_1, the current $i_L(t)$ needs to be determined. In steady-state operation, a certain current $i_{L,0} = i_L(t_0)$ is presumed. On the assumption of a positive phase shift, $0 \leq \varphi \leq \pi$, the resulting expressions for the inductor current are [35] :

$$\begin{array}{lll} \text{time interval I :} & i_L(t) = i_{L,0} + (V_1 + nV_2)t/L & 0 \leq t \leq T_\varphi \\ \text{time interval II :} & i_L(t) = i_L(T_\varphi) + (V_1 - nV_2)(t - T_\varphi)/L & T_\varphi < t \leq T_s/2 \end{array} \tag{2.13}$$

Due to half-cycle symmetry (2.11) and with $T_\varphi = \varphi/(2\pi f_s)$,

$$i_{L,0} = \frac{\pi(nV_2 - V_1) - 2\varphi nV_2}{4\pi f_s L} \tag{2.14}$$

is obtained for positive phase shift, $0 \leq \varphi \leq \pi$, and the same result for negative phase shift, $-\pi \leq \varphi < 0$. With 2.10 and 2.12, and by extending the results to the full phase shift range, $-\pi < \varphi \leq \pi$ the transferred power

$$P = P_1 = P_2 = \frac{nV_1V_2\varphi(\pi - |\varphi|)}{2\pi^2 f_s L} \qquad -\pi < \varphi \leq \pi \tag{2.15}$$

is obtained where $P > 0$ if the power is transferred from the LV side to the HV side and $P < 0$ if the power is transferred from the HV side to the LV side. The maximum power that can be transferred with phase shift modulation is then :

$$|P_{max}| = \frac{nV_1V_2}{8f_sL} \quad \text{for } \varphi = \pm\pi/2 \tag{2.16}$$

The maximum power is thus limited by the converter inductance L.

2.3.3 LC Filters

The role of the filters is to smoothen the battery and DC bus currents by filtering the AC component at the switching frequency. LC filters provide second-order filtering. Figure 2.18 shows the DAB converter with LC filters on each side. Damping resistors are added to make sure that the system is not unstable.

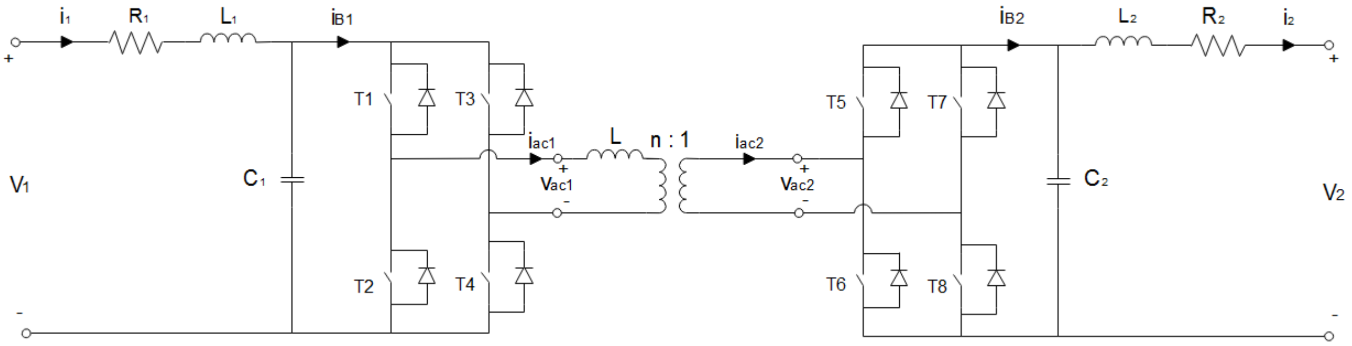

Figure 2.18 – DAB converter with LC filters on each side

The relation between i_1 and i_{B1} (see Figure 2.18) in Laplace domain is

$$i_1 = i_{B1}\frac{\frac{1}{L_1C_1}}{s^2 + \frac{R_1}{L_1}s + \frac{1}{L_1C_1}} \tag{2.17}$$

which can be rewritten in the canonical second-order system form :

$$i_1 = i_{B1}\frac{\omega_{n1}^2}{s^2 + 2\zeta_1\omega_{n1}s + \omega_{n1}^2} \tag{2.18}$$

with

$$\omega_{n1} = \frac{1}{\sqrt{L_1C_1}} \quad \text{and} \quad \zeta_1 = \frac{R_1}{2}\sqrt{\frac{C_1}{L_1}} \tag{2.19}$$

The same equations can be written for i_2 and i_{B2} with parameters ω_{n2} and ζ_2. The Bode diagram in Figure shows the frequency response of this system for different values of ζ.

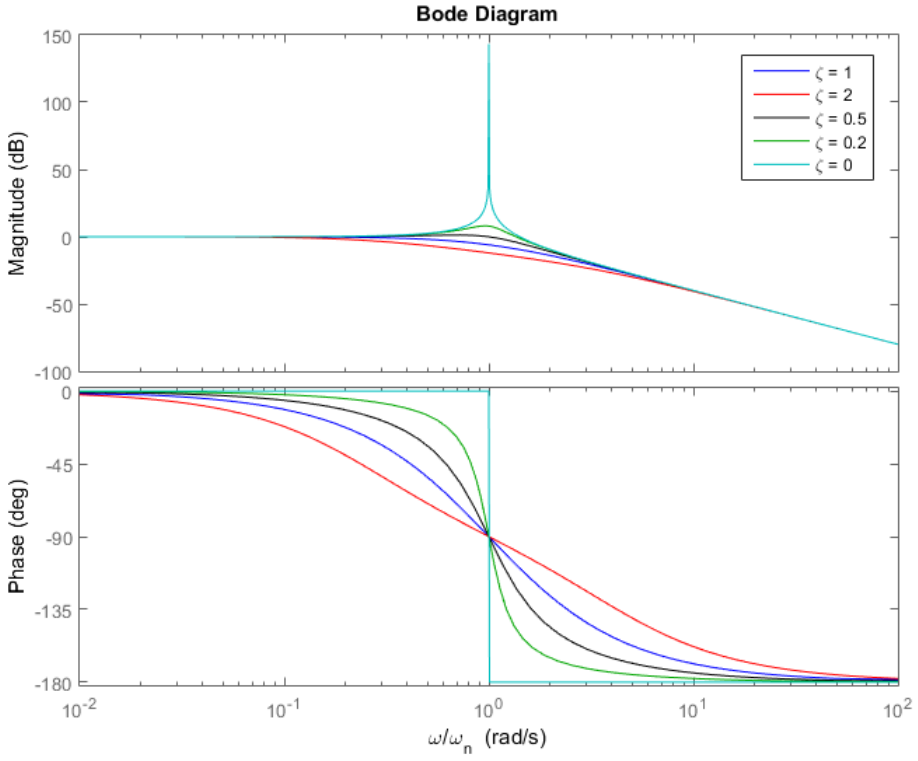

Figure 2.19 – Bode diagram of the LC filter with different values of ζ (damping factor)

The LC filters have to be designed such that

$$f_s \gg \omega_{n1}/2\pi \quad \text{and} \quad f_s \gg \omega_{n2}/2\pi \tag{2.20}$$

where f_s is the switching frequency of the converter, in order to effectively filter the AC component of frequency f_s.

2.3.4 Average Dynamic Model

Simulating the entire converter with its switches has a big computational cost. In fact, with the high switching frequency (typically in the range 10-100kHZ) of these converters and the high sensibility of the output power with respect to the phase shift φ, small time steps are required for the simulation to work properly.

Using an *average dynamic model* allows to obtain approximately the same input/output currents and voltages without modelling the switches, hence highly reducing the computational cost. The average dynamic model works by averaging the values of the currents and voltages over one switching period. The slower dynamic of the LC filters it thus modelled but the faster dynamic of the bridges is not taken into account as the AC component of frequency f_s is filtered anyway.

Rewriting 2.15 for the DAB converter with LC filters (see Figure 2.18), the average power transferred by each bridge over one switching period is

$$P = P_1 = P_2 = \frac{nV_{C1}V_{C2}\varphi(\pi - |\varphi|)}{2\pi^2 f_s L} \qquad -\pi < \varphi \leq \pi \tag{2.21}$$

with V_{C1} and V_{C2} the voltages across capacitors C_1 and C_2. From there, the two bridges can be replaced by controlled current sources (see Figure 2.20) with magnitudes

$$i_{B1} = \frac{P_1}{V_{C1}} = \frac{nV_{C2}\varphi(\pi - |\varphi|)}{2\pi^2 f_s L} \qquad -\pi < \varphi \leq \pi \tag{2.22}$$

$$i_{B2} = \frac{P_2}{V_{C2}} = \frac{nV_{C1}\varphi(\pi - |\varphi|)}{2\pi^2 f_s L} \qquad -\pi < \varphi \leq \pi \tag{2.23}$$

The average dynamic model and complete model are tested and compared in Subsection 2.3.6.

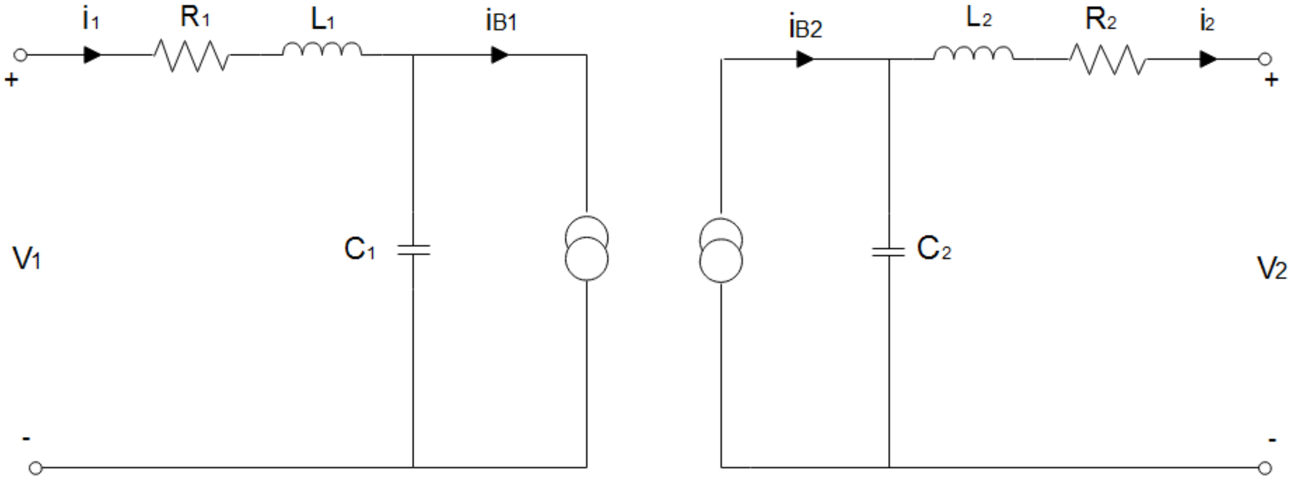

Figure 2.20 – Average dynamic model of DAB converter

2.3.5 Battery-side Controller

The battery-side controller acts on the control parameters of the DAB converter to control the power transfer between the battery and the DC bus. In the case of phase shift modulation, only the phase shift is controlled. In practice, the modulation technique is adjusted depending on the load. For example, *Zero Current Switching* (ZCS) can be obtained by having triangular or trapezoidal waveforms, hence decreasing the switching losses [35]. This is, however, not considered here. Figure 2.21 shows the resulting closed-loop system. The error $P_{ref} - P$ goes to a PI controller whose transfer function is

$$C(s) = K_P + \frac{K_I}{s} = G\frac{\tau s + 1}{\tau s} \tag{2.24}$$

where $K_P = G$ is the proportional gain and $K_I = G/\tau$ is the integral gain. Phase shift is kept in the interval $-\pi/2 \leq \varphi \leq \pi/2$ because the maximum power in absolute value is reached for $\varphi = \pm\pi/2$ and this interval minimizes the RMS current in the transformer.

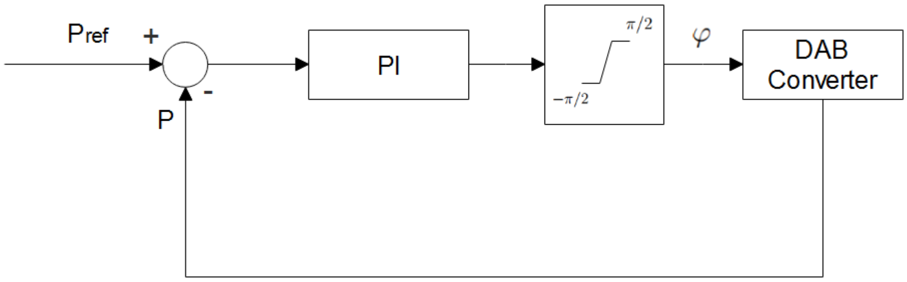

Figure 2.21 – Closed-loop control scheme of the DAB converter

2.3.6 Example and Tests

The battery defined in subsection 2.2.4 is considered to be connected to the LV side of the converter (port 1) and a DC bus of 700V is connected to the HV side (port 2). The DC bus voltage is considered here to be constant (ideal voltage source). The parameters chosen for the DAB converter are given in Table 2.3 (refer to Figure 2.18).

L	23μH	f_s	20kHz
R_1	0.1Ω	R_2	0.1Ω
L_1	0.1mH	L_2	0.1mH
C_1	1mF	C_2	1mF
V_{1nom}	430V	V_{2nom}	700V
n	$V_{1nom}/V_{2nom} = 0.61$		

Table 2.3 – Parameters of DAB converter

Since the nominal power of the battery is 25kW (>5kW), IGBTs are used as switching devices [37]. The choice of f_s = 20kHz is realistic for IGBTs used in this power range [38]. With that choice of parameters, the natural frequency of the LC filters is :

$$f_{n1} = f_{n2} = \frac{1}{2\pi\sqrt{LC}} = 503\text{Hz}$$

The influence of the DAB converter parameters is discussed in Appendix B. Figure 2.22 shows the power curve of the lossless DAB for the chosen parameters (Equation 2.21). The inductance L was chosen such that the converter can transfer a maximum power of 50kW, if it is necessary for a short duration. In this way, the normal operating area is in the more linear part of the curve.

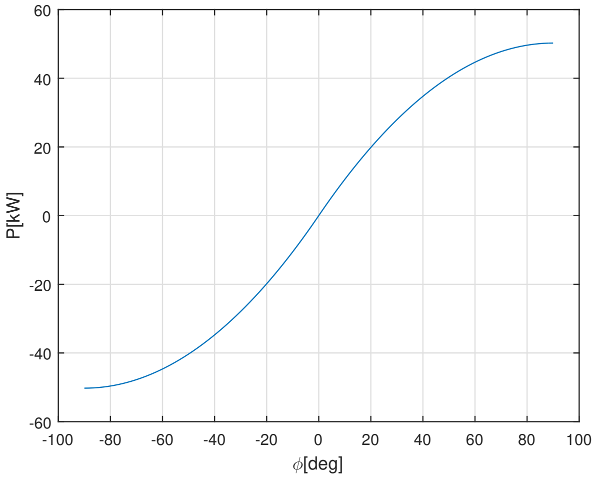

Figure 2.22 – P vs φ for $V_{C1} = 430\text{V}$ and $V_{C2} = 700\text{V}$

Since this model is lossless, it does not directly computes the efficiency of the converter. However, it can be taken taken into account indirectly. This type of converter typically has a nominal efficiency of about 95% [39]. Figure 2.23 shows the typical load-efficiency curve of a DAB converter. The efficiency is higher than 90% as long as the load is higher than 10% of the maximum load.

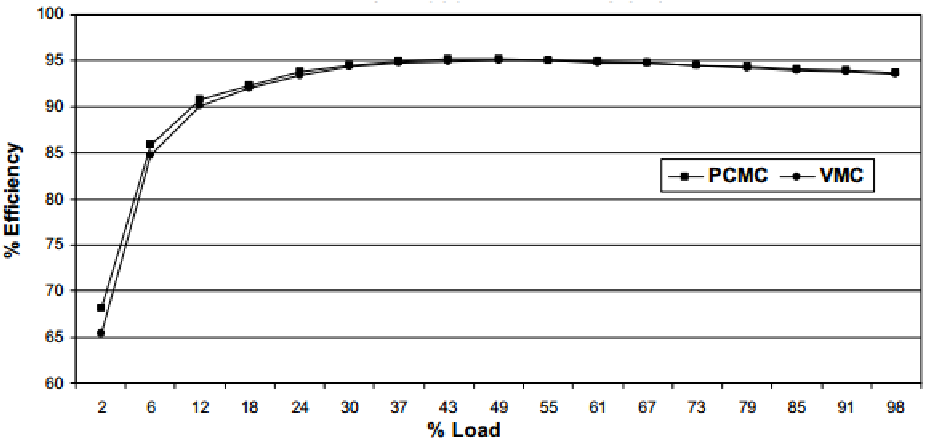

Figure 2.23 – Typical load-efficiency curve of a DAB converter (Source : [40])

Open-loop system

Figures 2.24-2.27 show the open-loop response to a phase shift step in terms of power at the battery (LV) and at the DC bus (HV) for the complete model and the average dynamic model. The comparison shows that the average dynamic model (Figure 2.20) reproduces quite accurately the behaviour of the complete model (Figure 2.18). The transferred power has an overshoot and transient oscillations due to the LC filters. Figures 2.28-2.31 show the voltages across the capacitors C_1 and C_2. Figure 2.32 shows the current and voltages waveforms at the transformer in steady-state.

In order for the simulations to work properly with the complete model, the duty cycles D_1 and D_2 are set slightly smaller than 1/2 and the switches have conducting and snubber resistances. On top of that, the asymmetry between the two bridges may explain why there is a power transfer when φ is 0 (Figures 2.24 and 2.26).

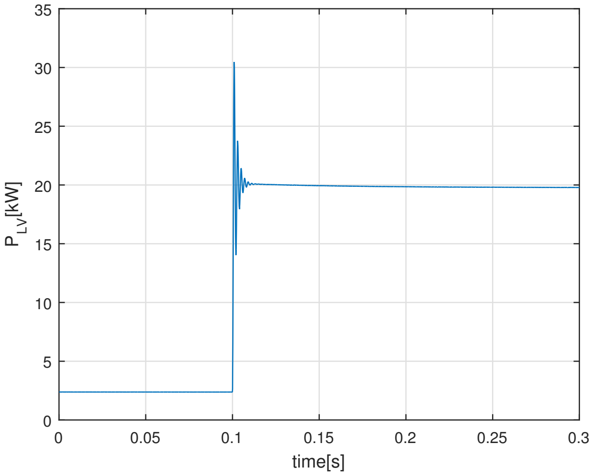

Figure 2.24 – P_{LV} after a 20° phase shift step with complete model

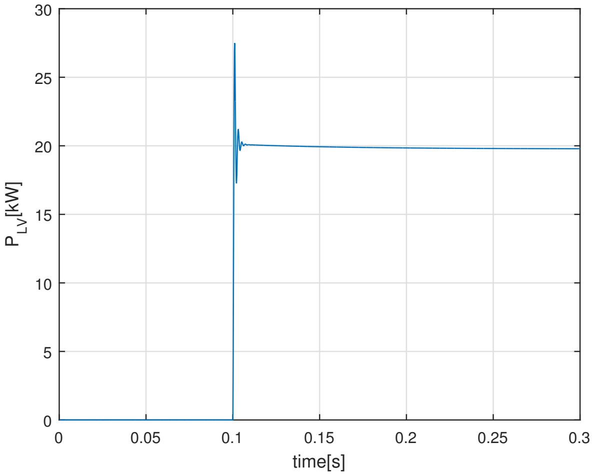

Figure 2.25 – P_{LV} after a 20° phase shift step with average dynamic model

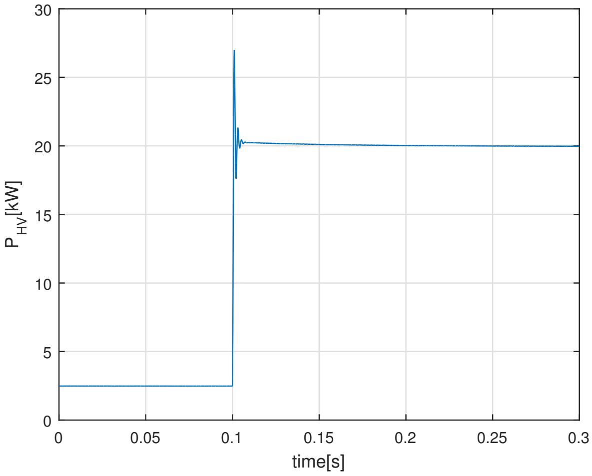

Figure 2.26 – P_{HV} after a 20° phase shift step with complete model

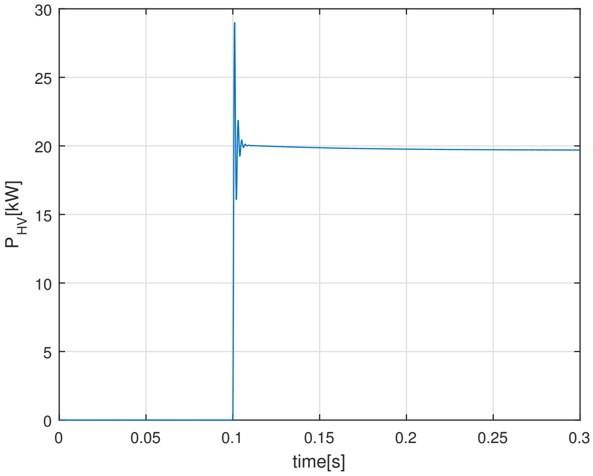

Figure 2.27 – P_{HV} after a 20° phase shift step with average dynamic model

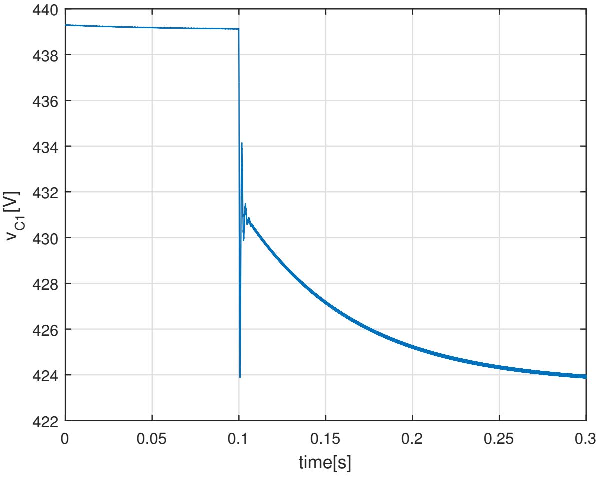

Figure 2.28 – v_{C1} after a 20° phase shift step with complete model

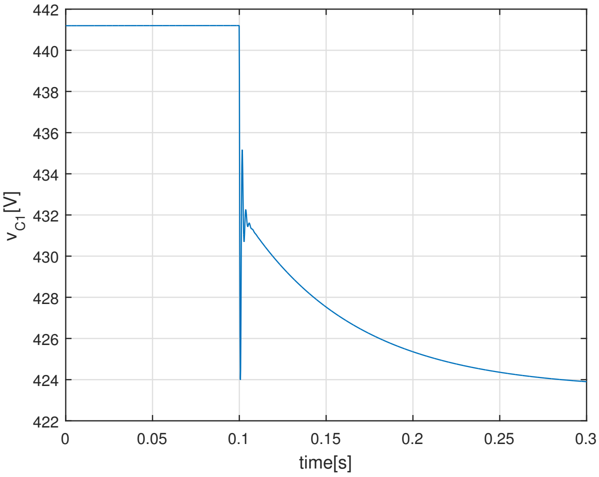

Figure 2.29 – v_{C1} after a 20° phase shift step with average dynamic model

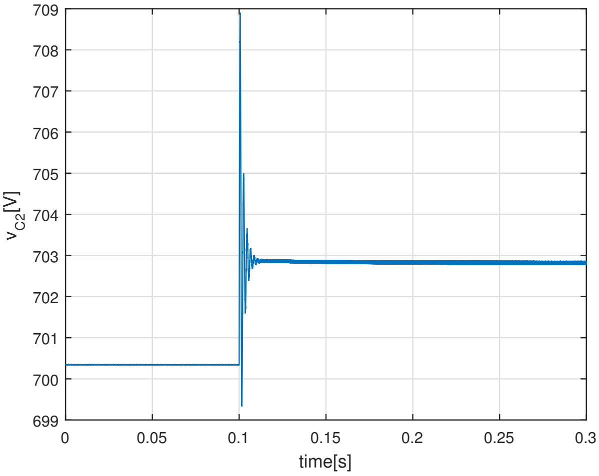

Figure 2.30 – v_{C2} after a 20° phase shift step with complete model

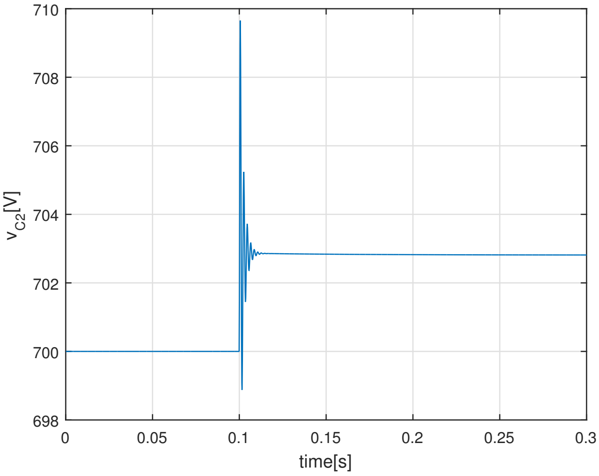

Figure 2.31 – v_{C2} after a 20° phase shift step with average dynamic model

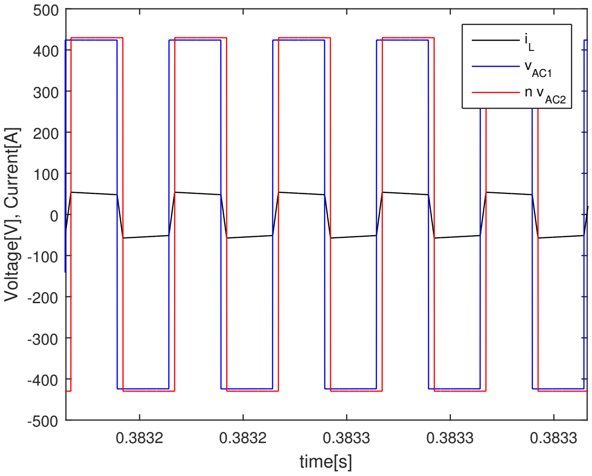

Figure 2.32 – Current and voltages waveforms (referred to LV side) at the transformer in steady-state

Closed-loop system

The parameters chosen for the PI controller are the following (Equation 2.24) :

G	0.9 deg/kW
τ	20 ms

Table 2.4 – Parameters of PI battery-side controller

The influence of the controller parameters is discussed in Appendix B. Figures 2.33-2.38 show the closed-loop response of the system in terms of power transfer at the battery, the DC bus and the control parameter φ. Due to the gradual increase of φ, the power overshoot is smaller than in the open-loop case.

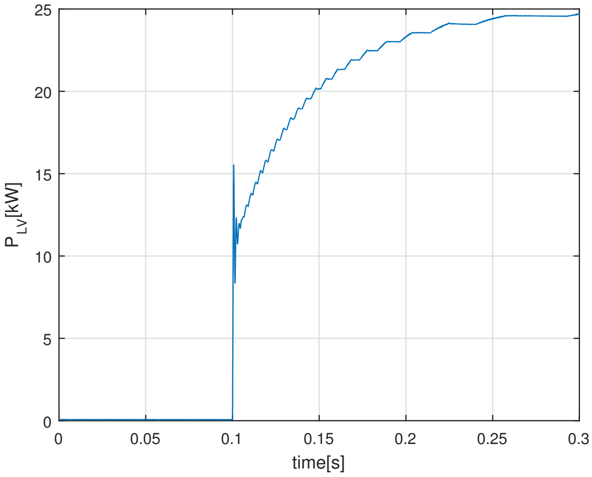

Figure 2.33 – P_{LV} after a P_{ref} step of 25kW with complete model

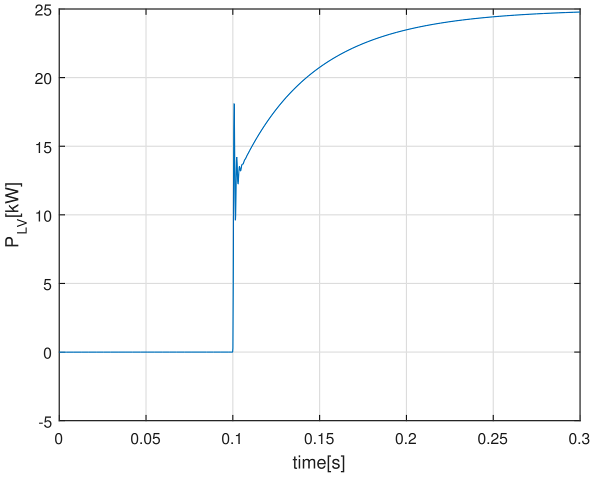

Figure 2.34 – P_{LV} after a P_{ref} step of 25kW with average dynamic model

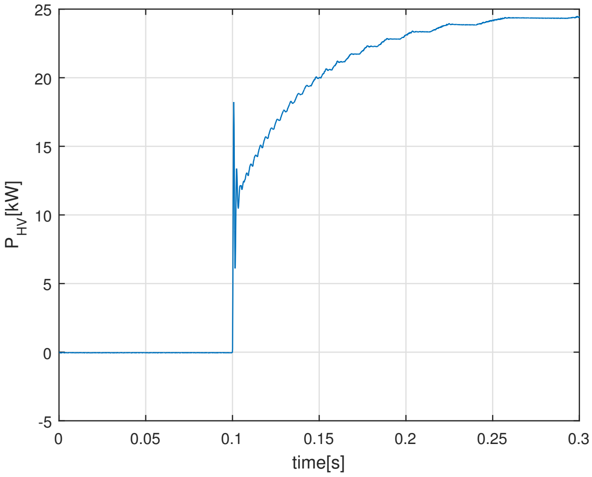

Figure 2.35 – P_{HV} after a P_{ref} step of 25kW with complete model

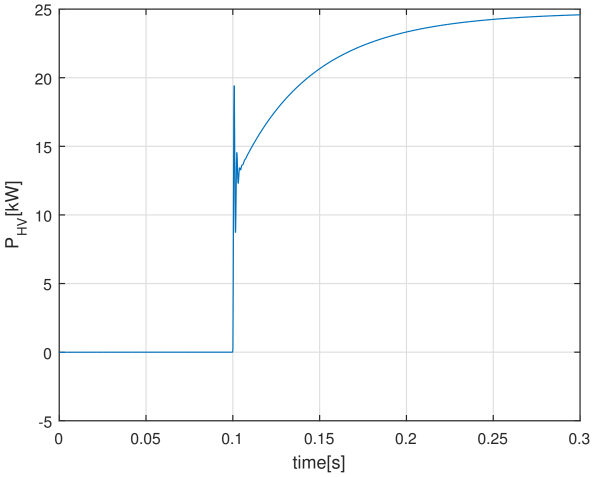

Figure 2.36 – P_{HV} after a P_{ref} step of 25kW with average dynamic model

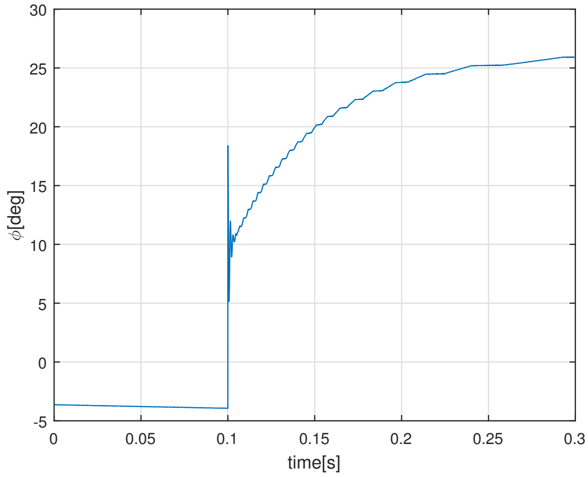

Figure 2.37 – φ after a P_{ref} step of 25kW with complete model

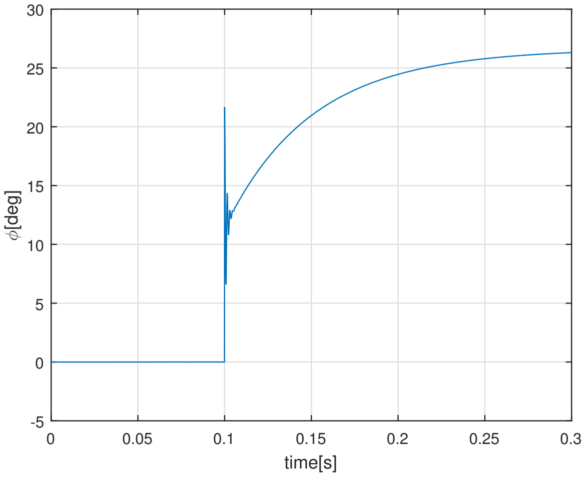

Figure 2.38 – φ after a P_{ref} step of 25kW with average dynamic model

2.4 DC/AC Converter

2.4.1 Topology

The DC/AC converter, also called inverter, can convert DC input voltage into AC output voltage. The inverter can either be connected in single-phase or in three-phase. Usually, when the power of the system is higher than a few kilowatts, it has to be connected in three-phase.

Single-phase Inverter

Figure 2.39 shows the simplest version of the single-phase inverter : it is a half-bridge voltage source inverter (VSI) which contains two controllable switches.
Like in the DC/DC converter, those switches can be MOSFETs or IGBTs depending on the required breakdown voltages, power and switching frequency (Figure 2.15). IGBTs are preferred for applications with output power higher than 5kW [37]. The antiparallel diodes can conduct the inductor current when all the switches are off. They can also conduct reverse current in the case of unidirectional switches such as IGBTs. With this structure, the converter is bidirectional and can thus also work as an AC/DC rectifier.
The modulation technique used is called pulse-width modulation (PWM) : the pulse-width of the signal controlling the switches is modulated in order to control the average value of v_m over one switching period. A 2-level PWM technique is used such that that v_m is either high or low :

$$v_m(t) = \begin{cases} +V_{DC}/2 & \text{if } \mathrm{T}_1 \text{ on and } \mathrm{T}_2 \text{ off} \\ -V_{DC}/2 & \text{if } \mathrm{T}_1 \text{ off and } \mathrm{T}_2 \text{ on} \end{cases} \tag{2.25}$$

Considering one switching period T_s starting at t=0 is considered, we have :

$$\begin{array}{ll} v_m(t) = V_{DC}/2 & 0 \leq t \leq DT_s \\ v_m(t) = -V_{DC}/2 & DT_s < t \leq T_s \end{array} \tag{2.26}$$

where D is the *duty cycle* of the control signal. The average value of v_m over one switching period is thus :

$$\langle v_m \rangle = DV_{DC}/2 - (1-D)V_{DC}/2 \quad 0 \leq D \leq 1 \tag{2.27}$$

If we define $m = 2D - 1$, we have :

$$\langle v_m \rangle = mV_{DC}/2 \quad -1 \leq m \leq 1 \tag{2.28}$$

$\langle v_m(t) \rangle$ is a time-varying function that can be modulated between $-V_{DC}/2$ and $V_{DC}/2$. The modulating signal is a thus a sine wave with the desired amplitude, frequency and phase shift :

$$m(t) = Msin(\omega t + \varphi) \quad -1 \leq M \leq 1 \tag{2.29}$$

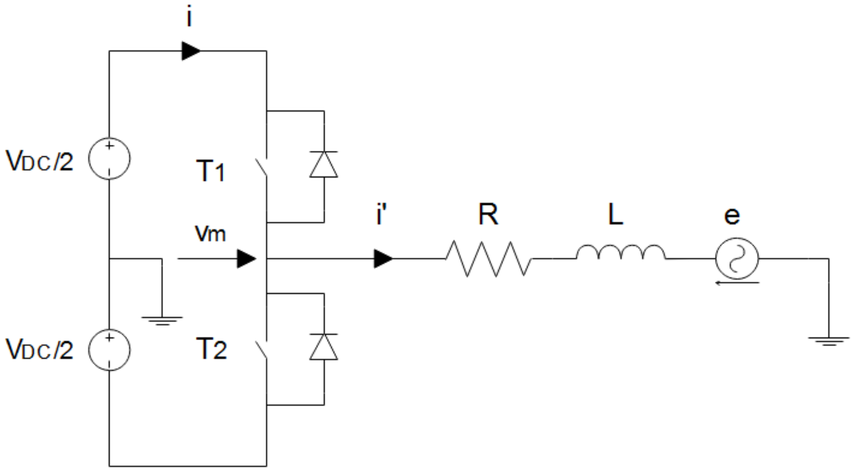

Figure 2.39 – Topology of a single-phase half-bridge inverter

The control signal of the switches is generated by comparing the modulating signal $m(t)$ with a triangular carrier as shown in the example of Figure 2.40. The control signals of T_1 and T_2 are complement to each other. The frequency of the carrier determines the switching frequency f_s of the control signal. The carrier frequency is much higher than the fundamental frequency so that the output current is as smooth as possible. However, the carrier frequency cannot be too high in order to have acceptable switching losses.

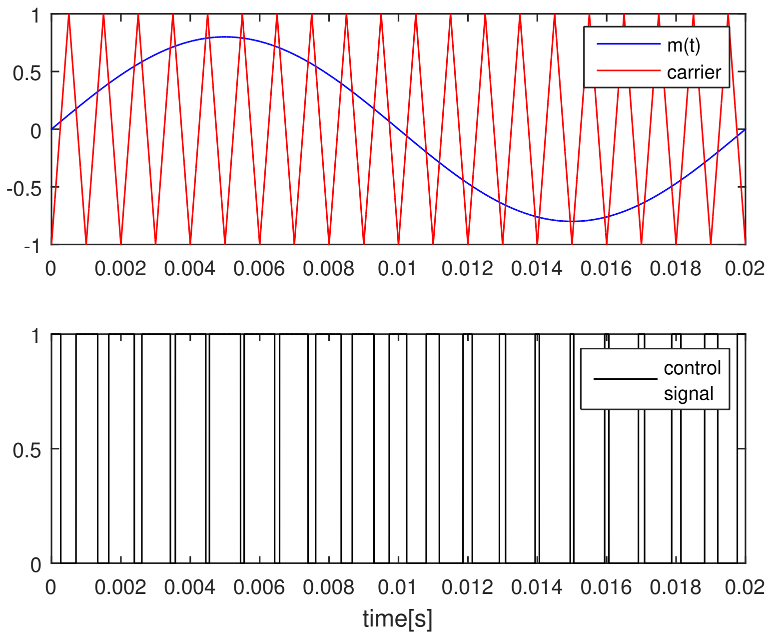

Figure 2.40 – Example of modulating signal ($M = 0.8$, $\omega = 2\pi 50$ rad/s), carrier ($f_s = 1$kHz) and control signal for 2-level PWM

Based on the values of R and L, the output average current $\langle i'(t) \rangle$ can be computed with phasor equations :

$$\overline{I'} = \frac{\overline{V}_m - \overline{E}}{\overline{Z}} \tag{2.30}$$

with

$$\langle i'(t) \rangle = I' sin(\omega t + \psi) = \Im\{\overline{I'} e^{j\omega t}\} \tag{2.31}$$

$$e(t) = E sin(\omega t) = \Im\{\overline{E} e^{j\omega t}\} \tag{2.32}$$

$$\langle v_m(t) \rangle = V_m sin(\omega t + \varphi) = \Im\{\overline{V}_m e^{j\omega t}\} \tag{2.33}$$

$$\overline{Z} = R + j\omega L \tag{2.34}$$

Regardind the input average current $\langle i(t) \rangle$, power conservation gives

$$V_{DC} \langle i(t) \rangle = \langle v_m(t) \rangle \langle i'(t) \rangle \tag{2.35}$$

which implies :

$$\langle i(t) \rangle = \frac{V_m I'}{V_{DC}} sin(\omega t + \varphi) sin(\omega t + \psi) = \frac{V_m I'}{2V_{DC}} (cos(\varphi - \psi) - cos(2\omega t + \varphi + \psi)) \tag{2.36}$$

The average input current of a single-phase inverter thus has a DC component as well as an AC component of angular frequency 2ω.

Another topology that can be used is the full bridge single-phase inverter as shown in Figure 2.41. The working principle is exactly the same as for the half-bridge inverter except that the modulated voltage can vary between $-V_{DC}$ and V_{DC}. In fact, we have :

$$v_m(t) = \begin{cases} +V_{DC} & \text{if } \mathrm{T}_1,\ \mathrm{T}_4 \text{ on and } \mathrm{T}_2,\ \mathrm{T}_3 \text{ off} \\ -V_{DC} & \text{if } \mathrm{T}_2,\ \mathrm{T}_3 \text{ on and } \mathrm{T}_1,\ \mathrm{T}_4 \text{ off} \end{cases} \tag{2.37}$$

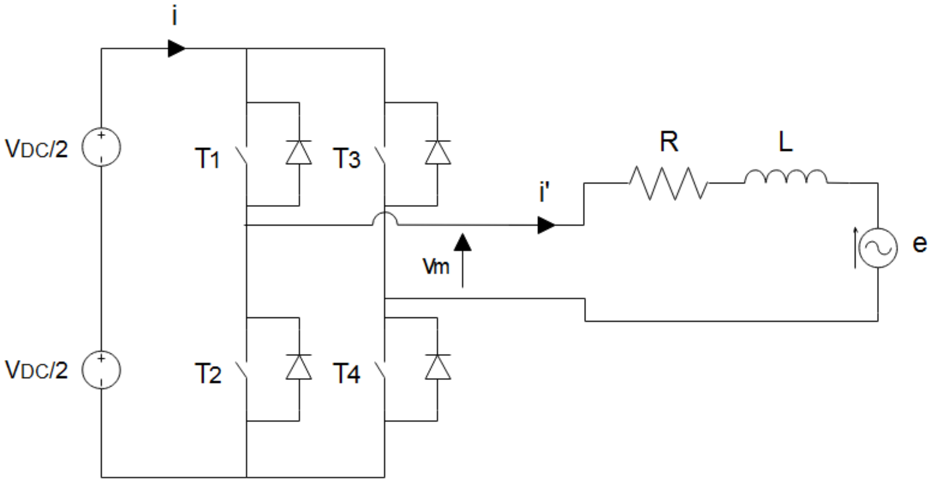

Figure 2.41 – Topology of a single-phase full bridge inverter

Three-phase Inverter

Figure 2.42 shows the topology of a three-phase inverter. The working principle is basically the same as for the single-phase bridge.

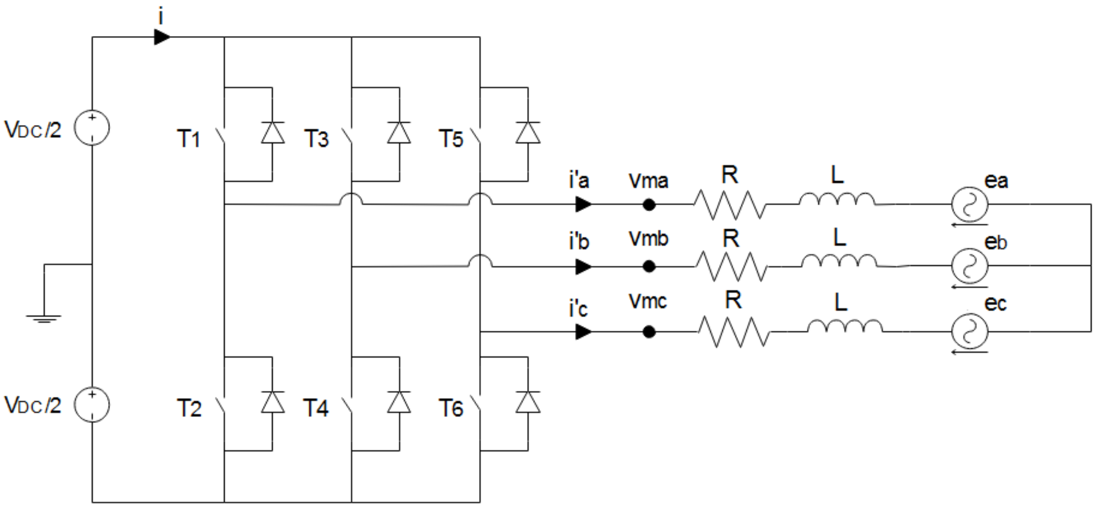

Figure 2.42 – Topology of a three-phase inverter

Considering there is no zero-sequence current (floating neutral), we have :

$$i'_a + i'_b + i'_c = 0 \tag{2.38}$$

Power conservation gives :

$$V_{DC} i(t) = v_{ma}(t) i'_a(t) + v_{mb}(t) i'_b(t) + v_{mc}(t) i'_c(t) \tag{2.39}$$

Using (2.38), it can be rewritten as :

$$V_{DC} i(t) = (v_{ma}(t) - v_{mc}(t)) i'_a(t) + (v_{mb}(t) - v_{mc}(t)) i'_b(t) = v_{m1}(t) i'_a(t) + v_{m2}(t) i'_b(t) \tag{2.40}$$

The phasor equations for the currents are, using (2.38) :

$$\begin{cases} \overline{V}_{ma} = \overline{E}_a + \overline{I'}_a \overline{Z} \\ \overline{V}_{mb} = \overline{E}_b + \overline{I'}_b \overline{Z} \\ \overline{V}_{mc} = \overline{E}_c + (-\overline{I'}_a - \overline{I'}_b) \overline{Z} \end{cases} \tag{2.41}$$

Substracting the third equations to the first and second, we have :

$$\begin{cases} \overline{V}_{m1} = \overline{E}_{ac} + (2\overline{I'}_a + \overline{I'}_b)\overline{Z} \\ \overline{V}_{m2} = \overline{E}_{bc} + (2\overline{I'}_b + \overline{I'}_a)\overline{Z} \end{cases} \tag{2.42}$$

These equations can be rewritten to isolate the currents :

$$\begin{cases} \overline{I'}_a = \frac{(2\overline{V}_{m1} - \overline{V}_{m2}) - (2\overline{E}_{ac} - \overline{E}_{bc})}{3\overline{Z}} \\ \overline{I'}_b = \frac{(2\overline{V}_{m2} - \overline{V}_{m1}) - (2\overline{E}_{bc} - \overline{E}_{ac})}{3\overline{Z}} \end{cases} \tag{2.43}$$

The system can thus be entirely described with two line voltages and currents.
With this three-phase inverter topology, the modulated phase voltage can vary between $-V_{DC}/2$ and $V_{DC}/2$. Hence, considering the modulated voltages are balanced, we have :

$$\langle v_{ma}(t)\rangle = m_a(t)V_{DC}/2 = V_m sin(\omega t + \varphi) \tag{2.44}$$

$$\langle v_{mb}(t)\rangle = m_b(t)V_{DC}/2 = V_m sin(\omega t - 2\pi/3 + \varphi) \tag{2.45}$$

$$\langle v_{mc}(t)\rangle = m_c(t)V_{DC}/2 = V_m sin(\omega t - 4\pi/3 + \varphi) \tag{2.46}$$

with

$$V_m \leq V_{DC}/2 \tag{2.47}$$

Unlike for the single-phase inverter, $\langle i(t)\rangle$ has no component of angular frequency 2ω, if the system is balanced. The mathematical proof is given in Appendix A. However, $\langle i(t)\rangle$ has a 2ω component if the system is unbalanced (negative sequence) [41].

Regarding simulations, the inverter can either be fully modelled with its switches or an *average model* can be used where the voltages and currents are averaged over one switching period. The full model will be used if the harmonics emitted by the system must be represented ; the average model will be used if the computational cost must be reduced.

2.4.2 LC Filters

Like for the DC/DC converters, LC filters are placed on both sides of the DC/AC converter to smoothen the currents by filtering the high frequency components. It is particularly important on the AC side in order to comply with the grid standards in terms of harmonic distortion. Figure 2.43 shows the three-phase inverter with both filters. The DC bus capacitor is represented as an ideal voltage source.

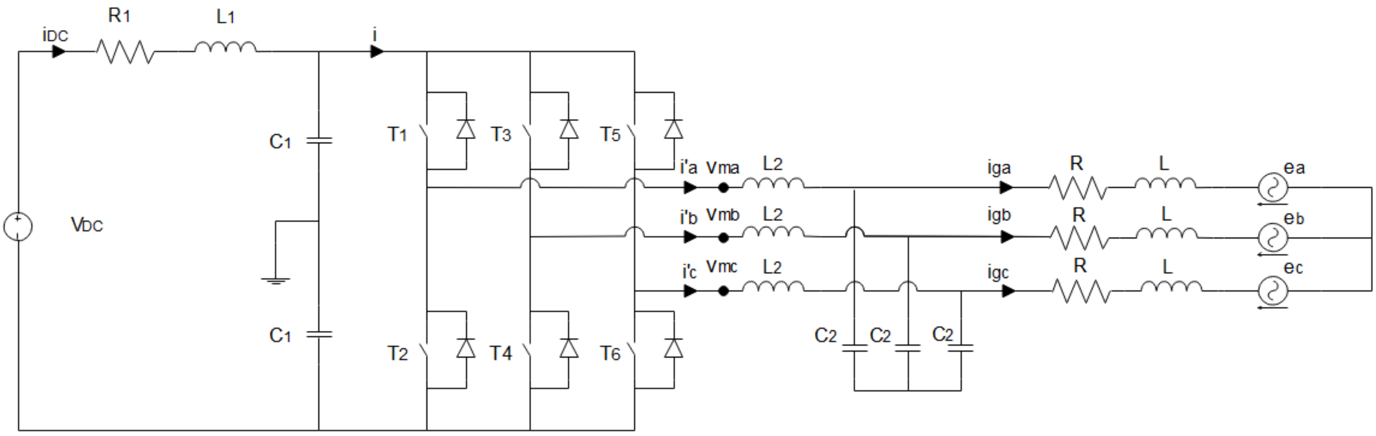

Figure 2.43 – Topology of a three-phase inverter with LC filters

DC side filter

The filter on the DC side is composed of the capacitors C_1 and the inductor L_1. The working principle is the same as for the DC/DC converter (Subsection 2.3.3). With the two capacitors C_1 in series, the natural frequency of the filter is :

$$\omega_{n1} = \frac{1}{\sqrt{L_1 C_1/2}} \tag{2.48}$$

The filter should be designed such that

$$2\pi f_s \gg \omega_{n1} \tag{2.49}$$

where f_s is the switching of the inverter. The condition

$$\omega_{n1} \gg 2\omega \tag{2.50}$$

should also be satisfied to make sure that a possible component of angular frequency 2ω (in case of unbalance) is not amplified.

AC side filter

The filter on the AC side is composed of the inductors L_2 and capacitors C_2, added between the inverter and the RL grid impendance. The resonance frequency of the system is computed as follows, neglecting the resistance R for simplicity :

$$\begin{aligned} i' &= v_m \frac{1}{j\omega L_2 + 1/(j\omega C_2) \parallel j\omega L} \\ &= v_m \frac{-\omega^2 L C_2 + 1}{j\omega(-\omega^2 L L_2 C_2 + L + L_2)} \end{aligned} \tag{2.51}$$

$$i_g = i' \frac{1/(j\omega L)}{j\omega C_2 + 1/(j\omega L)} = v_m \frac{1}{j\omega(-\omega^2 L L_2 C_2 + L + L_2)} \tag{2.52}$$

The resonance frequency is thus :

$$\omega_{n2} = \sqrt{\frac{L + L_2}{L L_2 C_2}} \tag{2.53}$$

The filter should be designed such that

$$2\pi f_s \gg \omega_{n2} \tag{2.54}$$

to eliminate the high order harmonics. The condition

$$\omega_{n2} \gg \omega \tag{2.55}$$

should also be satisfied to make sure that there is no resonance at the fundamental frequency.

The harmonic content of the injected current is usually characterized with the *total harmonic distortion* (THD) and *total demand distortion* (TDD). Current THD is defined as follows :

$$THD = \frac{\sqrt{I_2^2 + I_3^2 + I_4^2 + ...}}{I_1} \tag{2.56}$$

The TDD corresponds to the THD in the case where the injected current is the rated current I_L of the system. Figure 2.44 shows the limits for individual harmonic orders and TDD as established by IEEE (Std 519). Those limits depend on the *short-circuit current* I_{sc} at the point of common coupling. Other organisations than IEEE have established harmonic emission limits, such as IEC (Std 61000-3-2), with slight differences between them. It must be stated that those limits only concern low frequency harmonics. For example, the IEEE Std 519 is only applied until the 50th harmonic order [42]. As for now, there are no real restrictions on individual harmonic emissions between around 2.5kHz and 150 kHZ. This is becoming problematic as it is typically the frequency range utilized by Smart Grid communication technologies. On the other hand, high frequency emissions are limited due to potential perturbations with radio frequencies.

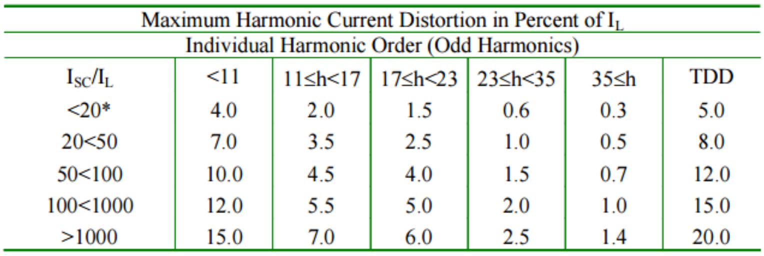

Maximum Harmonic Current Distortion in Percent of I_L

Individual Harmonic Order (Odd Harmonics)

I_{SC}/I_L	<11	11≤h<17	17≤h<23	23≤h<35	35≤h	TDD
<20*	4.0	2.0	1.5	0.6	0.3	5.0
20<50	7.0	3.5	2.5	1.0	0.5	8.0
50<100	10.0	4.5	4.0	1.5	0.7	12.0
100<1000	12.0	5.5	5.0	2.0	1.0	15.0
>1000	15.0	7.0	6.0	2.5	1.4	20.0

Figure 2.44 – Current distortion limits in IEEE Std 519 for general distribution systems (120V through 69kV)

2.4.3 Example and Tests

The parameters of the system are (refer to Figure 2.43) :

V_{DC}	700V	f_s	5kHz
R	0.16 Ω	L	500μH
C_1	1mF	L_1	100μH
C_2	40μF	L_2	500μH

Table 2.5 – Parameters of inverter

Like in previous sections, the rated power the system is 25kW. A three-phase inverter is used with IGBTs and a switching frequency $f_s = 5$kHz which is typical for inverters in this range of power using PWM modulation [43, 44]. This type of inverter typically has an efficiency of about 98% [44]. The system is connected to a grid with 230V RMS phase voltage. The DC bus voltage of 700V allows the system to generate a 230V RMS phase voltage since the condition (2.47) becomes

$$\sqrt{2} \cdot 230 \leq V_{DC}/2 \tag{2.57}$$

which is thus fulfilled. Considering a base power of 25kVA, the grid impedance can also be expressed in per unit :

$$R_{pu} = \frac{400^2}{25e3} R = 0.025 \text{ p.u.}$$

$$X_{pu} = \frac{400^2}{25e3} \omega L = 0.025 \text{ p.u.}$$

This is the typical order of magnitude of grid impendance in distribution systems. In low voltage, the resistive and reactive part of the impedance typically have the same order of magnitude, unlike in higher voltage levels where the resistive part is usually negligible. The influence of these parameters is discussed in Appendix C. With the chosen parameters, the resonance frequencies of the filters are :

$$f_{n1} = \frac{1}{2\pi\sqrt{L_1 C_1/2}} = 712\text{Hz}$$

$$f_{n2} = \frac{1}{2\pi}\sqrt{\frac{L + L_2}{L L_2 C_2}} = 1592\text{Hz}$$

The phase shift φ between the inverter and the grid is adapted to generate the rated current. Figure 2.45-2.48 show the results of the simulations. The Fourier analysis of the grid current shows a peak around the resonance frequency f_{n2} with a 1550Hz (h = 31) component at 0.78%. Therefore, the system complies with the limits (see Figure 2.44) if the short-circuit current at the PCC is such that the ratio $I_{sc}/I_L > 20$. Despite the filtering, the system still emits some harmonics around the switching frequency (0.64% at 4900Hz) and its multiples. However, as explained in Subsection 2.4.2, these are not yet limited by the standards. The grid current has a small DC component which translates into a 50Hz component for the DC current.

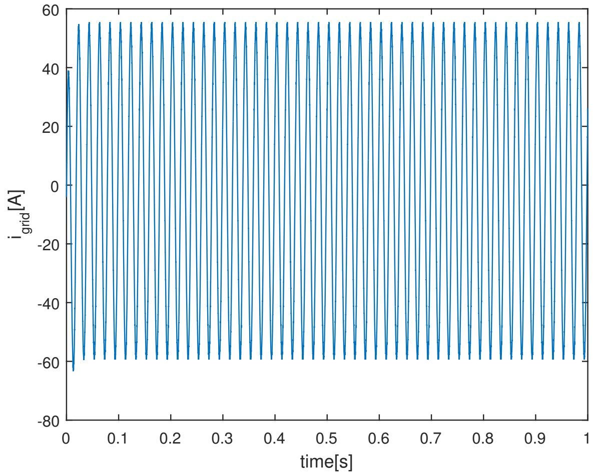

Figure 2.45 – Grid current with $\phi = 3.6^\circ$

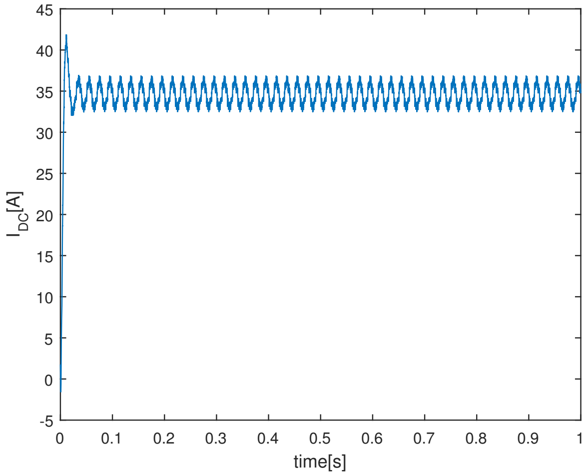

Figure 2.46 – DC current with $\phi = 3.6^\circ$

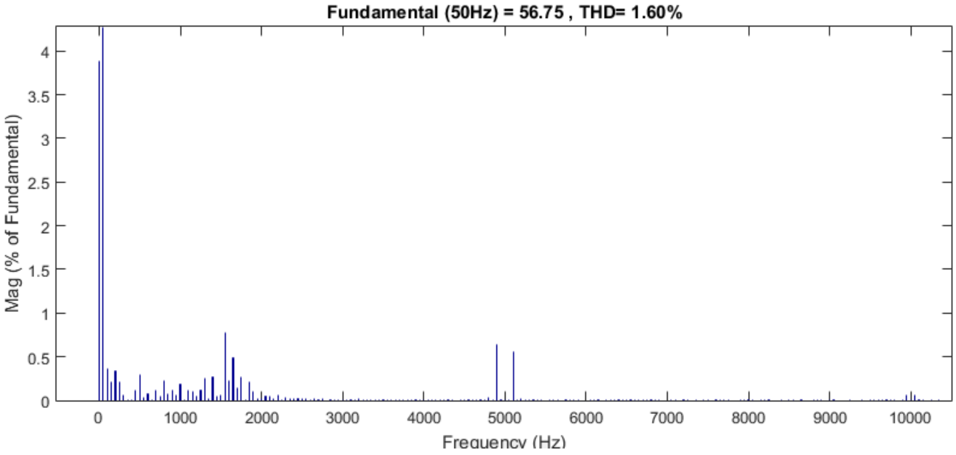

Figure 2.47 – Fourier analysis of the grid current

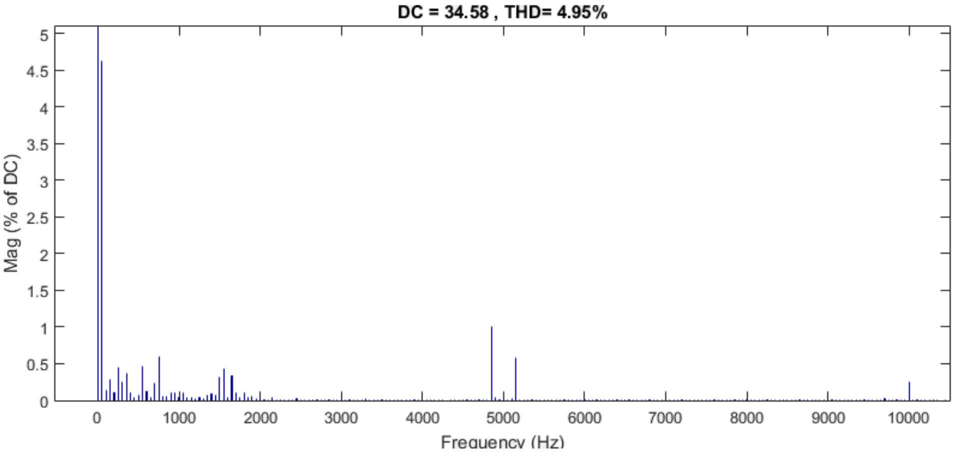

Figure 2.48 – Fourier analysis of the DC current

2.5 Grid-side Controller

2.5.1 General Structure

The grid-side controller is in charge of

- Balancing the system in terms of active power by regulating the DC bus voltage.
- Controlling the reactive power injection.
- Controlling the current injected to/from the grid and making sure the current is substantially balanced and harmonic-free. This particularly important in a microgrid environment where the power qualtiy perturbations can be problematic in island mode. This control requires some sort of synchronization with the grid.
- Generating the modulating signals for the PWM inverter.

Figure 2.49 shows an example of grid-side controller structure. The syncronous reference frame control, also called dq control, uses a reference frame transformation, $abc \rightarrow dq$, to transform the grid current and voltage waveforms into a reference frame that rotates synchronously with the grid voltage. By means of this, the control variables become DC values; thus, filtering and controlling can be easier achieved. The dq control structure is normally associated with proportional–integral (PI) controllers since they have a satisfactory behavior when regulating DC variables. To improve the performance of PI controller in such a structure, cross-coupling terms and voltage feedforward are usually used [45].

A synchronization system is required to synchronize the grid currents with the grid voltage. A very common synchronization technique is the phase-locked loop (PLL) system. It is described in details in subsection 2.5.2. The PLL measures the phase θ of the voltage vector which is then used, in the case of dq control structure, to operate the $abc \rightarrow$ dq transformations. The PLL is also used to measure the grid frequency. The DC link (active power) and Q (reactive power) controllers generate the reference currents in the dq frame.

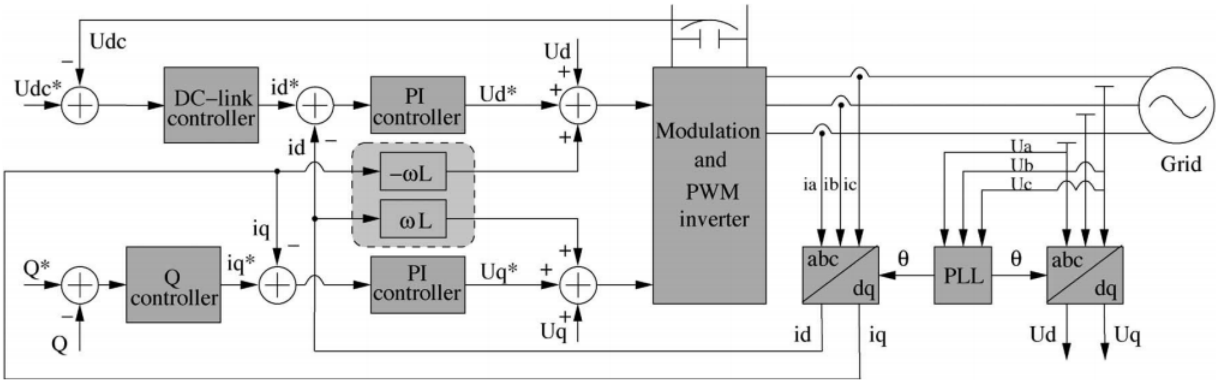

Figure 2.49 – General structure for synchronous rotating frame control strategy (Source : [45])

Regarding power quality issues, it is possible to perform harmonic current compensation in *dq* frame. Since PI controllers typically are associated with dq control structure, the possibilities for harmonic compensation are based on low-pass (LP) and high-pass (HP) filters. If the current controller has to be immune to the grid voltage harmonic distortion (mainly fifth and seventh in three-phase systems), harmonic compensator for each harmonic order should be designed. Figure 2.50 shows the dq control structure having a harmonic compensator for the positive sequence of the fifth harmonic. In addition, under unbalanced conditions, harmonic compensators for both positive and negative sequences of each harmonic order are necessary. As a consequence, four compensators like the ones depicted in Figure 2.50 are necessary to compensate for the fifth and seventh harmonics. The complexity of the control algorithm is noticeable in this case [45].

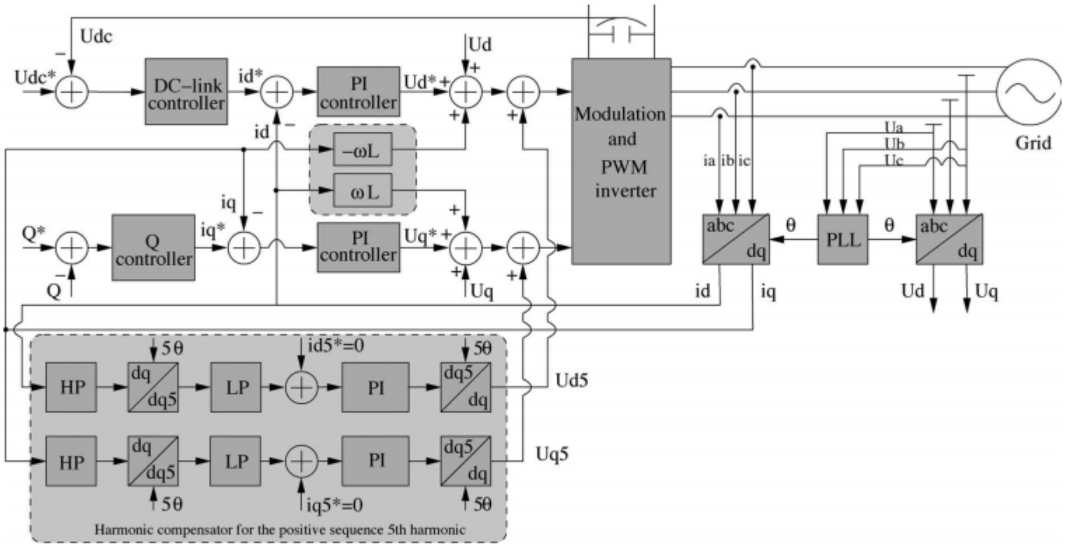

Figure 2.50 – Method for compensating the positive sequence of the fifth harmonic in dq control structure (Source : [45])

Another possible way to structure the control loops is to use the implementation in stationary reference frame, as shown in Figure 2.51. In this case, the grid currents are transformed into stationary reference frame using the $abc \rightarrow \alpha\beta$ module. Since the control variables are sinusoidal in this situation and due to the known drawback of PI controller in failing to remove the steady-state error when controlling sinusoidal waveforms, employment of other controller types is necessary. Proportional resonant (PR) controllers gained a large popularity in the last decade in current regulation of grid-tied systems [45, 46]. In the case of stationary frame control, cross-coupling terms and voltage feedforward are not necessary. Voltage feedforward is used here nonetheless, as it provides soft-start capabilities [41]. The PLL is also necessary to operate $dq \rightarrow \alpha\beta$ transformation for the reference currents.

Characteristic to this controller is the fact that it achieves a very high gain around the resonance frequency, thus being capable to eliminate the steady-state error between the controlled signal and its reference. Moreover, high dynamic characteristics of PR controller have been reported in different works [45, 46].

Regarding harmonic compensation, things are different than in synchrounous frame control. Several harmonic compensators (HC) are cascaded and tuned at the desired frequency. In this way, selective harmonic compensation at different frequencies is obtained. Only one block is required to control both positive and negative sequences for each harmonic. The resulting structure is shown in Figure 2.52. The structure is noticeably simpler than for synchronous frame control. For all these reasons, stationary frame control with PR controllers is chosen here for the BESS.

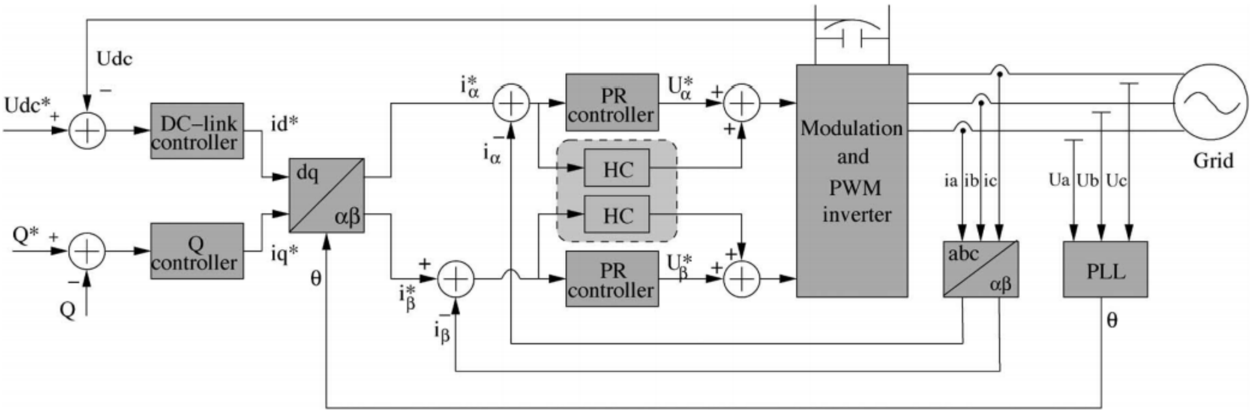

Figure 2.51 – General structure for stationary reference frame control strategy (Source : [45])

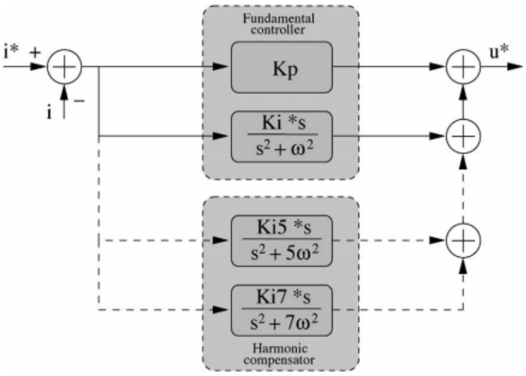

Figure 2.52 – Structure of the harmonic compensator attached to the resonant controller of the fundamental current (Source : [45])

2.5.2 Phase-locked Loop

The role of the PLL is to measure the phase and frequency of the grid voltage. Two types of PLL are presented and compared here : the synchronous reference frame PLL (SRF-PLL) and the enhanced PLL (EPLL).

SRF-PLL

The SRF-PLL is arguably the most well-known and widely used concept in the general areas of power engineering [47]. Its structure is depicted in Figure 2.53.

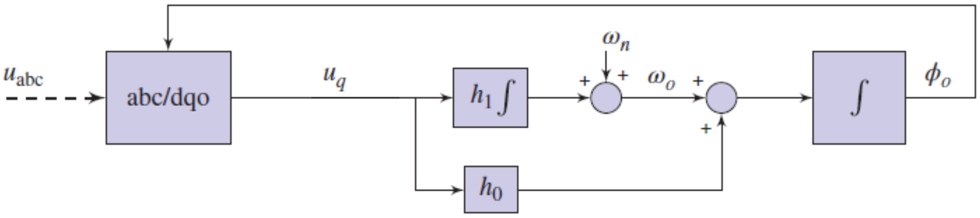

Figure 2.53 – Three-phase SRF-PLL structure (Source : [47])

The PI controller brings the error signal u_q to zero in steady-state. The estimated phase and angular frequency are respectively ϕ_0 and ω_0. The $abc \to dq0$ Park transformation is defined by $u_{dq0} = Pu_{abc}$ where

$$P = \frac{2}{3}\begin{pmatrix} sin\phi_0 & sin(\phi_0 - 2\pi/3) & sin(\phi_0 - 4\pi/3) \\ cos\phi_0 & cos(\phi_0 - 2\pi/3) & cos(\phi_0 - 4\pi/3) \\ 1/2 & 1/2 & 1/2 \end{pmatrix} \tag{2.58}$$

The drawback of the SRF-PLL is that the phase and frequency estimations are perturbed when the grid voltage is polluted with harmonics or unbalanced. Moreover, there is a trade-off at the PI controller between

- a fast controller that reacts quickly to phase/frequency changes but that is vulnerable to grid perturbations.
- a controller that is robust towards perturbations but has a slow response time.

In Figures 2.54-2.57, the grid voltage (400V line RMS) subsequently undergoes a frequency jump, phase jump and 5th harmonic injection with different values of PI parameters h_1 and h_2. The harmonic injection induces an oscillating signal, both for the frequency and phase estimation. It is not shown here but in case of unbalance, an oscillating signal of angular frequency 2ω appears. The influence of the paremeters is as follows :

- In terms of frequency, increasing h_1 improves the response time but increases the error in case of phase jump and amplifies the oscillations due to harmonics. h_1 doesn't have much of an influence on phase estimation.
- In terms of frequency, increasing h_2 deteriorates the response time but decreases the error in case of phase jump. In terms of phase error, increasing h_2 makes the PLL recover faster from a phase jump but amplifies the oscillations due to harmonics.

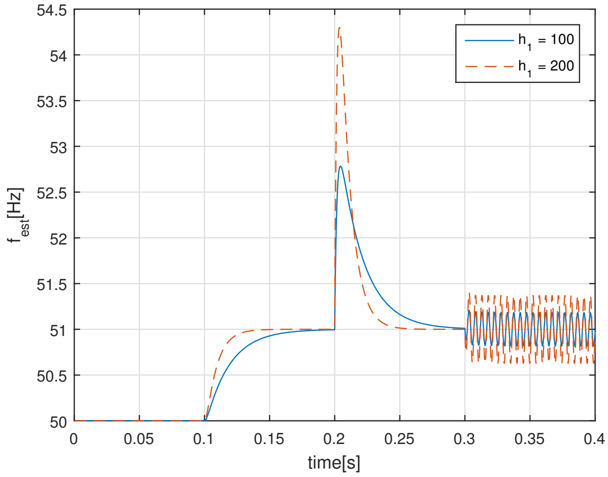

Figure 2.54 – Frequency estimation with 1Hz frequency jump at t=0.1s, 15° phase jump at t=0.2s and 5% of 5th harmonic injection at t=0.3s, $h_2 = 2$

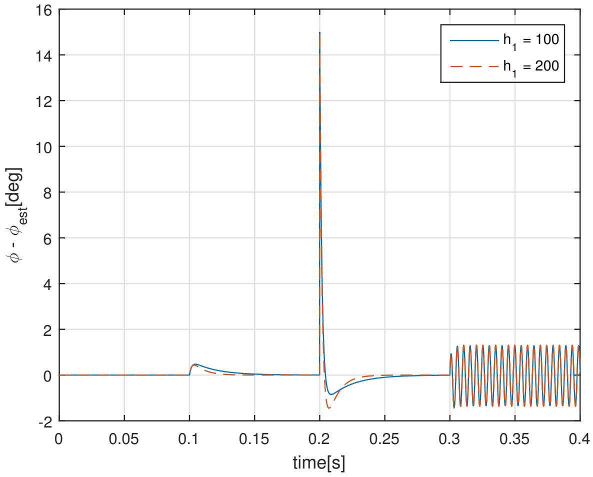

Figure 2.55 – Phase error with 1Hz frequency jump at t=0.1s, 15° phase jump at t=0.2s and 5% of 5th harmonic injection at t=0.3s, $h_2 = 2$

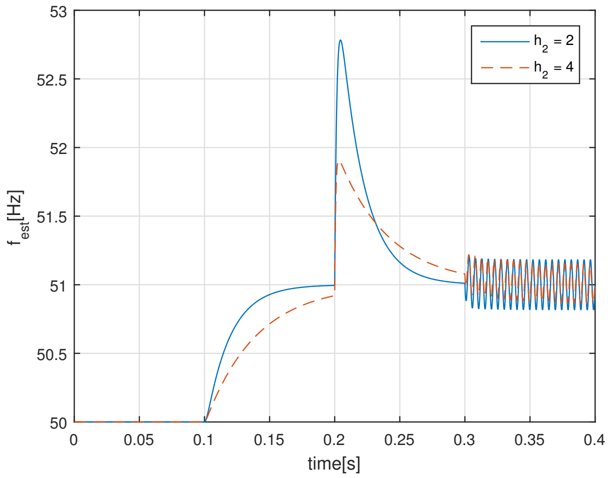

Figure 2.56 – Frequency estimation with 1Hz frequency jump at t=0.1s, 15° phase jump at t=0.2s and 5% of 5th harmonic injection at t=0.3s, $h_1 = 100$

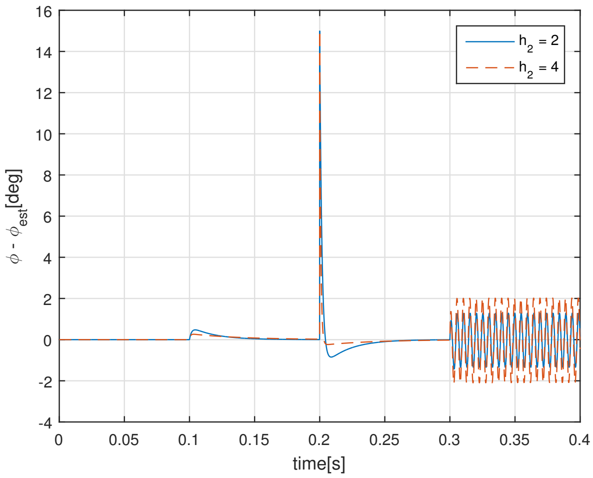

Figure 2.57 – Phase error with 1Hz frequency jump at t=0.1s, 15° phase jump at t=0.2s and 5% of 5th harmonic injection at t=0.3s, $h_1 = 100$

EPLL

Figure 2.58 shows the structure of the three-phase EPLL where (·) is the dot product of two vectors and

$$C(\phi_0) = \begin{pmatrix} cos\phi_0 \\ cos(\phi_0 - 2\pi/3) \\ cos(\phi_0 - 4\pi/3) \end{pmatrix} \quad S(\phi_0) = \begin{pmatrix} sin\phi_0 \\ sin(\phi_0 - 2\pi/3) \\ sin(\phi_0 - 4\pi/3) \end{pmatrix} \tag{2.59}$$

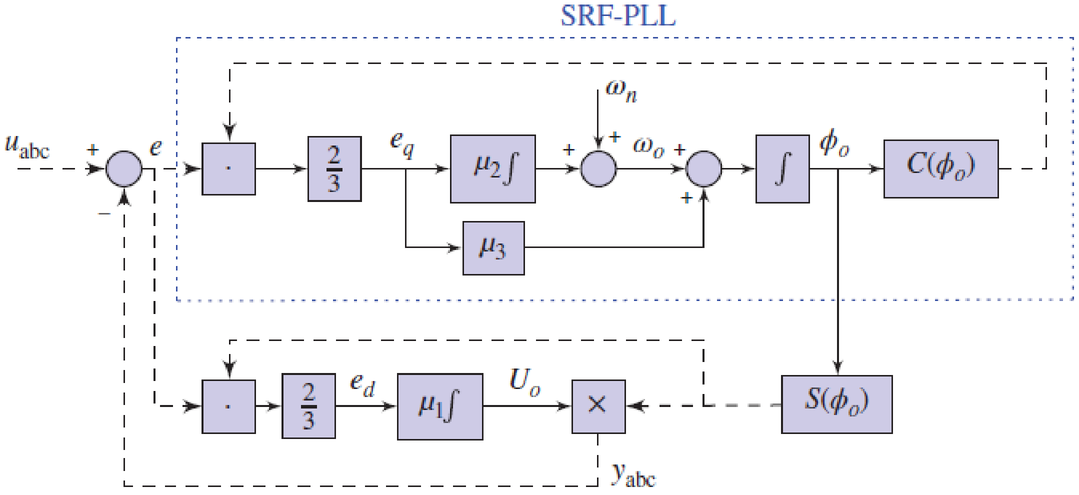

Figure 2.58 – Three-phase EPLL structure (Source : [47])

The EPLL is an extension of the SRF-PLL with an additional loop that estimates the amplitude U_0 of the signal. In this way, the EPLL provides an estimation of the whole signal y_{abc} while the SRF-PLL only estimates the phase and frequency. With this structure, the EPLL can be further extended, for example with an estimation of the negative sequence of the fundamental component of the signal, as depicted in Figure 2.59.

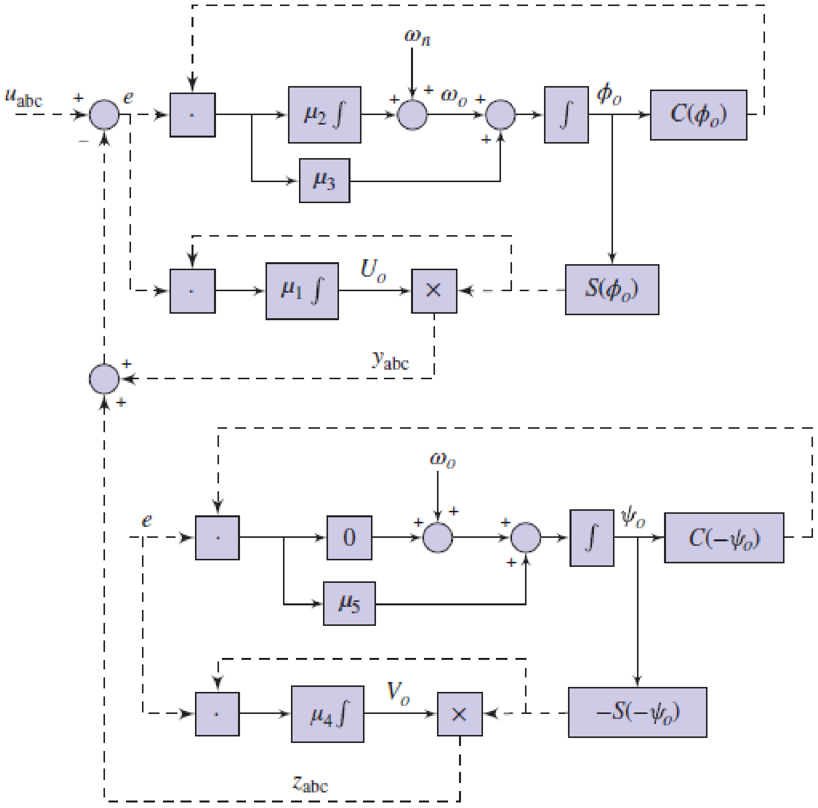

Figure 2.59 – Three-phase EPLL structure with positive and negative sequence estimation (Source : [47])

V_0, ψ_0, z_{abc} are respectively the estimated amplitude, phase and signal of the negative sequence. The negative sequence block uses the frequency estimation provided by the positive sequence block. With this structure, the negative sequence is exctracted, hence the phase ϕ_0

and frequency ω_0 estimations are not affected by an unbalance. The EPLL can even be further extended to extract positive and negative sequence of harmonics, as shown in Figure 2.60. The choice made here is to extract the 5th and 7th harmonics.

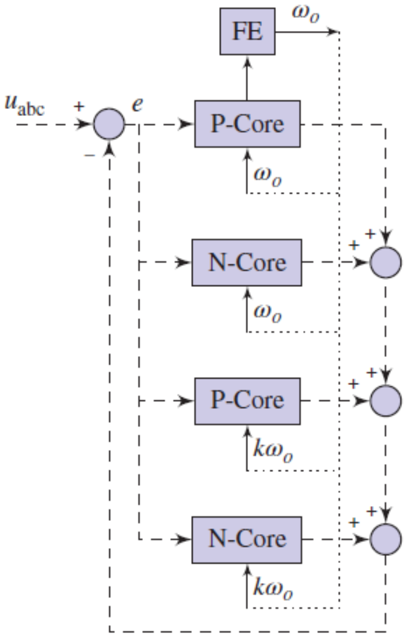

Figure 2.60 – Extendend EPLL to estimate the harmonic of order k (Source : [47])

From now on, the values of the parameters of the EPLL (referred to Figure 2.59) are :

μ_1	200	μ_2	100
μ_3	2	μ_4	200
μ_5	2		

Table 2.6 – Parameters of EPLL

The values of the parameters are the same for the harmonics blocks (μ_4 and μ_5). In Figures 2.61-2.64, the grid voltage subsequently undergoes a frequency jump, phase jump, 5th and 7th harmonic injection and 1-phase voltage dip. The voltage dip induces a negative sequence at the fundamental frequency. It can be observed that EPLL filters rather quickly the effects of the harmonics and unbalance, while being able to track frequency and phase jumps. For these reasons, the EPLL is the chosen synchronization system for the BESS. Post-filtering of the frequency estimation can also be used if necessary.

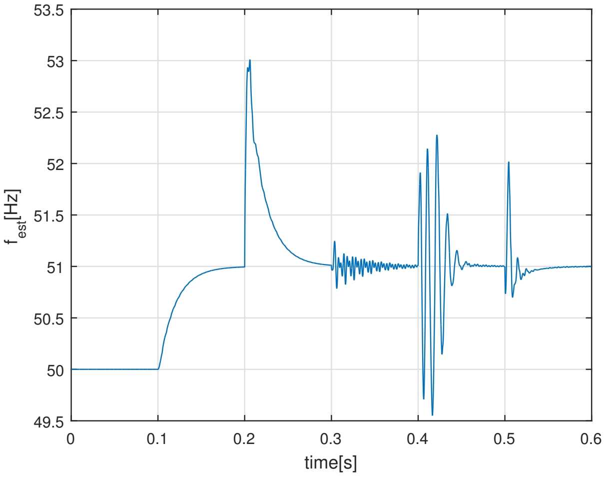

Figure 2.61 – Frequency estimation with 1Hz frequency jump at t=0.1s, 15° phase jump at t=0.2s, 5% of 5th and 3% of 7th harmonic injection at t=0.3s, 50% 1-phase voltage dip from t=0.4s to t=0.5s

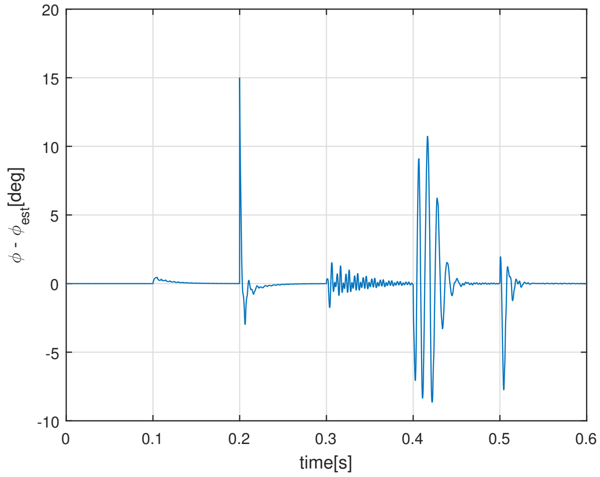

Figure 2.62 – Phase error with 1Hz frequency jump at t=0.1s, 15° phase jump at t=0.2s, 5% of 5th and 3% of 7th harmonic injection at t=0.3s, 50% 1-phase voltage dip from t=0.4s to t=0.5s

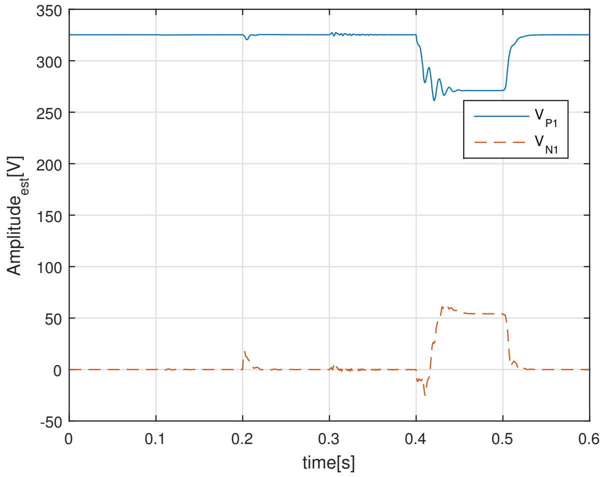

Figure 2.63 – Amplitude estimation of fundamental postive and negative sequence with 1Hz frequency jump at t=0.1s, 15° phase jump at t=0.2s, 5% of 5th and 3% of 7th harmonic injection at t=0.3s, 50% 1-phase voltage dip from t=0.4s to t=0.5s

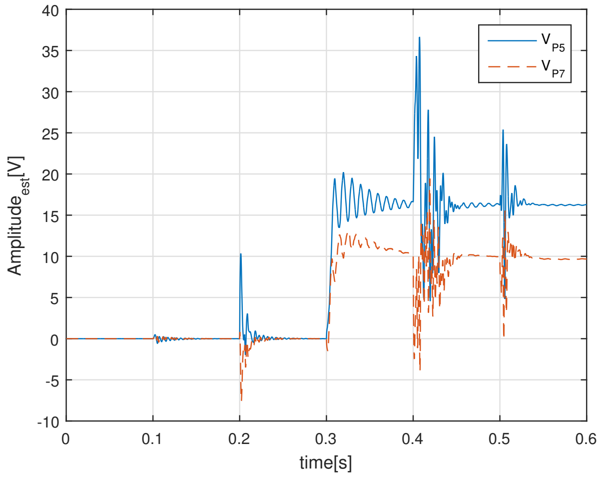

Figure 2.64 – Amplitude estimation of 5th and 7th harmonics (positive sequence) with 1Hz frequency jump at t=0.1s, 15° phase jump at t=0.2s, 5% of 5th and 3% of 7th harmonic injection at t=0.3s, 50% 1-phase voltage dip from t=0.4s to t=0.5s

2.5.3 PR Controllers

The general transfer function a PR controller is the following :

$$C(s) = K_P + \frac{2\omega_c K_I s}{s^2 + 2\omega_c s + \omega_n^2} \tag{2.60}$$

The term in ω_c at the denominator is a necessary damping term to make sure the gain is not infinite at the natural frequency, othwerise causing instability. ω_c corresponds to the cutoff frequency, which means that the gain at $\omega_n \pm \omega_c$ is 3dB smaller than at ω_n. Figures 2.65 and

2.66 show the influence of K_I and ω_c. Increasing K_I raises the gain at the natural frequency but leads to a wider band. Increasing ω_c does not change the gain at the natural frequency and leads to a wider band. The proportional term K_P helps the controller with soft-start capabilities. It should be noted that the PR controller uses the estimation of the PLL as natural frequency to make sure it keeps working even when the grid frequency changes. Stability problems can arise if the PR parameters are not chosen carefully. In fact, if the gain of the controller at the resonance frequency of the output LC filter is too high, the system will go into resonance. All the parameters of the PR controller thus have to be chosen carefully, taking into account the values of the inductance and capacitance of the LC filter. Considering H(s) is the transfer function between the input signal of the LC filter v_m and and the ouput signal i_g, the following result can be obtained (refer to Figure 2.43) :

$$H(s) = \frac{i_g}{v_m} = \frac{1/(LL_2C_2)}{s^3 + s^2R/L + s(L + L_2)/(LL_2C_2) + R/(LL_2C_2)} \tag{2.61}$$

The open-loop gain of the fundamental current is then $C(s)H(s)$ and the stability of the system depends on the closed-loop transfer function (unity feedback) which is

$$T_r(s) = \frac{C(s)H(s)}{1 + C(s)H(s)} \tag{2.62}$$

Specifically, the real part of each pole of $T_r(s)$ must be negative to ensure stability. Gain and phase margins are also commonly used to determine how close the system is to instability. The closed-loop system is unstable if the open-loop gain is greater than 1 at the frequency f_{180} at which the phase is 180°. From there, they are defined as follows :

- The gain margin is the difference between the open-loop gain at f_{180} and unity gain (0 dB). It also corresponds to the possible increase in feedback gain before the closed-loop system becomes unstable.
- The phase margin is the difference between 180° and the phase at which the gain is 0 dB.

Additional resonant controllers are used in parallel for the 5th and 7th harmonic currents. The transfer function of those controllers is :

$$C_k(s) = \frac{2\omega_c K_I s}{s^2 + 2\omega_c s + (k\omega_n)^2} \quad k = 5, 7 \tag{2.63}$$

The reference current is balanced, hence the setpoints of the harmonic and unbalanced currents are zero. Some active compensation techniques consist in intentionally injecting unbalanced/harmonic current in order to decrease the unbalance/harmonic content of the PCC voltage. This is thus not considered here. The output of the current controller is the reference voltage vector in $\alpha\beta$ frame. This vector is then transformed into the modulating signals for the inverter.

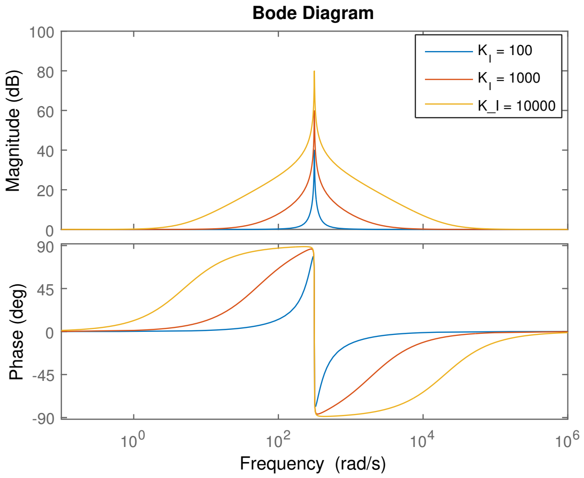

Figure 2.65 – Bode diagram of PR controller with $K_P = 1$ and $\omega_c = 1$ for different values of K_I

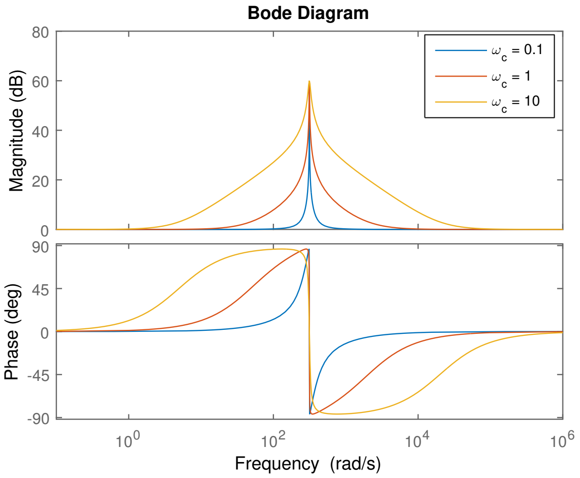

Figure 2.66 – Bode diagram of PR controller with $K_P = 1$ and $K_I = 1000$ for different values of ω_c

2.5.4 DC link and Q Controllers

Conventionally, PI controllers are adopted to regulate the DC link voltage and output reactive power [48]. They respectively generate the current references $i_{d,ref}$ and $i_{q,ref}$. Usually the design of these controllers aims for system sability having slow dynamics [45]. The transfer function of these controllers is

$$C(s) = G\frac{\tau s + 1}{\tau s} \tag{2.64}$$

where G is the proportional gain and τ the response time of the controller. For the DC link controller, G is adjusted depending on the size of the DC link capacitor, to make sure the voltage stays in acceptable range around the reference ; τ is tuned in function of the desired response time and power ramping rate. Instead of using the voltage error $V_{DC,ref} - V_{DC}$, the control variable used is $V_{DC,ref}^2 - V_{DC}^2$, proportional to the DC link energy error. In this way, the control loop becomes linear, while in conventional approach, the control loop is nonlinear [41].

2.5.5 Example and Tests

After several trials, the parameters of the PR controllers were chosen in order to have good dynamic performances while ensuring stability. The values are given in Table 2.7. The influence of these parameters is discussed in Appendix C.

K_P	0.1
K_I	3000
ω_c	0.1

Table 2.7 – Parameters of the PR controllers

Figures 2.67 and 2.68 show the response of the grid current to a pulse of $i_{d,ref}$. It appears that the current reacts virtually instantly to the command. Aside from the high frequency ripple, the response of the system is basically the same with the complete and average inverter models.

The zero-pole map of the closed-loop current controller is depicted in Figures 2.69 and 2.70. As the real part of each pole of the system is negative, the system is stable. The gain and phase margins of the system are given in Figure 2.71. The stability performances can be enhanced by using semi-state feedback(s), for instance with the current of the filtering inductance and/or the voltage of the filtering capacitor [41]. This is not considered here.

The DC link and Q controllers are tested with the whole system in Section 2.6.

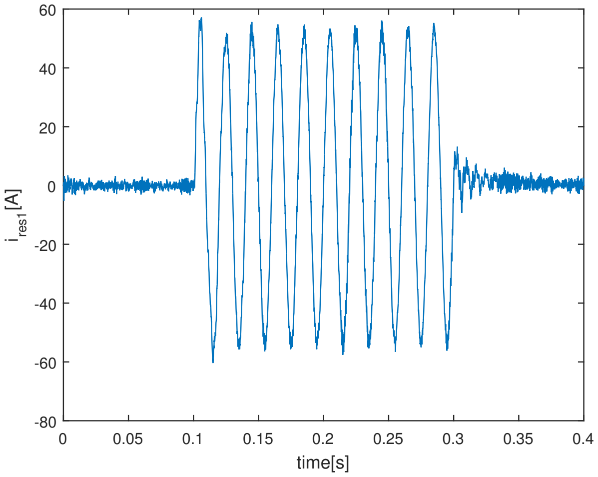

Figure 2.67 – Grid current i_{res1} with a pulse of $i_{d,ref}$ from t=0.1s to t=0.3s, using complete inverter model

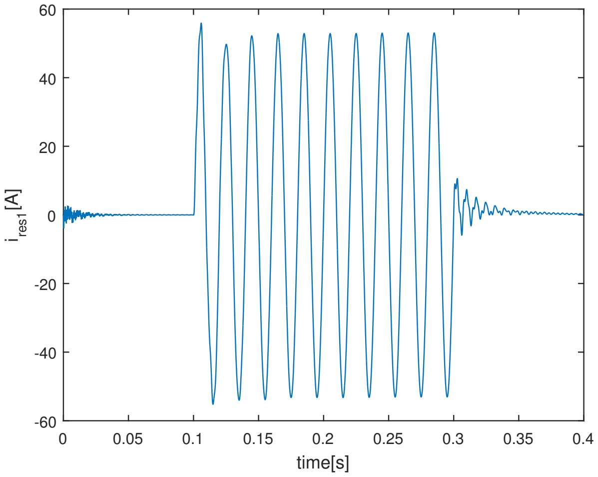

Figure 2.68 – Grid current i_{res1} with a pulse of $i_{d,ref}$ from t=0.1s to t=0.3s, using average inverter model

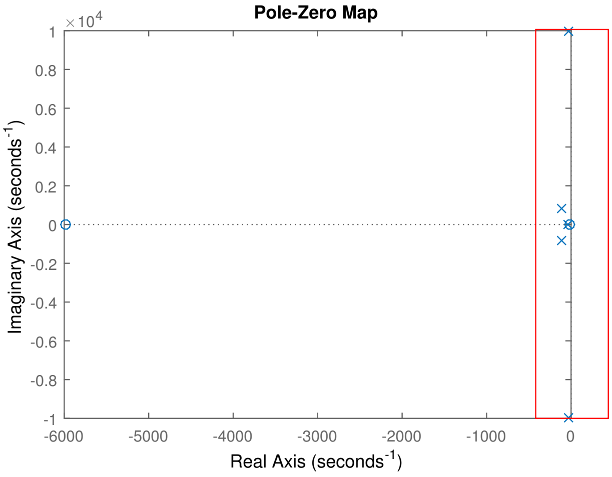

Figure 2.69 – Pole-zero map of closed-loop current controller (red : zoom)

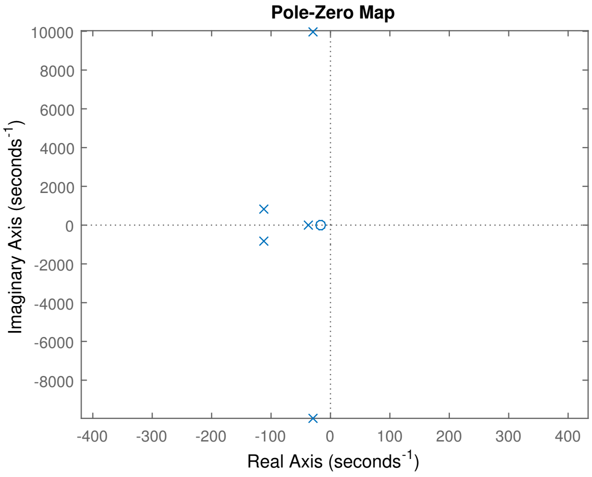

Figure 2.70 – Zoom of pole-zero map of closed-loop current controller

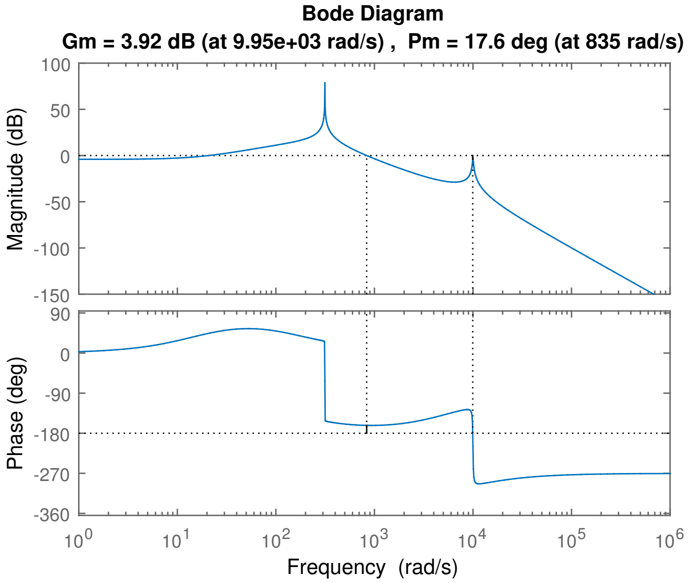

Figure 2.71 – Bode diagram of the open-loop gain and phase/gain margins of the closed-loop system

2.6 Tests on Complete BESS

Two tests are executed on the complete BESS. The first one shows how the system behaves when the grid undergoes perturbations such as harmonics and voltage dip. The goal is thus to evaluate the power quality provided by the BESS as well as the fault-ride through capability. The second test evaluates the ability of the system of to follow a series of active and reactive power setpoints. The average dynamic model is chosen for the DC/DC converter but the complete model is used for the inverter in order to evaluate the harmonic content of the grid current. The value chosen for the DC link capacitor is $C_{DC} = 4\text{mF}$. The equation for the DC link voltage is

$$V_{DC} = \int (I_{DAB} - I_{DC,inv})/C_{DC}\; dt \tag{2.65}$$

where I_{DAB} is the current from the DAB converter and $I_{DC,inv}$ is the DC current to the inverter. The parameters of the DC link and Q controllers are given in Table 2.8. The influence of these paremeters is discussed in Appendix D.

	DC link	Q
G	1e-3 [A/V^2]	2.5e-3 [A/VAr]
τ	100ms	20ms

Table 2.8 – Parameters of DC link and Q controllers

2.6.1 Power Quality and Fault-ride Through Capability

The test is the follwowing : a step of power setpoint is sent to the battery, then the grid undergoes a 1-phase voltage dip and finally 5th and 7th harmonics are added to the grid voltage. The results are depicted in Figures 2.72-2.78.

The output active power does not show much perturbations due to voltage dip or harmonics. The unbalance due to the 1-phase voltage dip induces a 2ω component in the DC inverter which consequently appears in the DC link voltage. During the voltage dip, the voltage setpoint allows to keep the grid current balanced. Equally, after the addition of harmonics, the voltage setpoint

is adapted to control the grid current harmonics.
The comparison of the harmonic limits in Figure 2.44 with the Fourier analysis in Figure 2.78 (0.98% at 1600Hz) shows that the grid current complies with the standard if $I_{sc}/I_L > 20$ at the PCC. Figure 2.77 shows that the DC current of the inverter, despite the LC filter, has a lot of high frequency ripple. Hence, the DC link capacitance must be large enough to effectively filter this ripple.

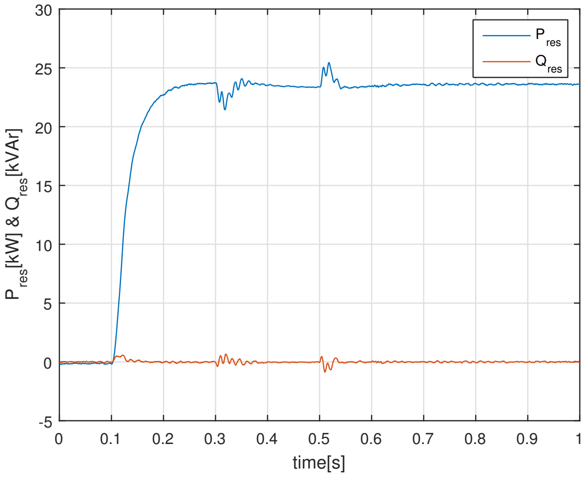

Figure 2.72 – Active and reactive power (positive fundamental sequence) injected to the grid with 25kW setpoint step at t=0.1s, 50% 1-phase voltage dip from t=0.3s to t=0.5s, addition of 5% of 5th harmonic and 3% of 7th harmonic from t=0.6s

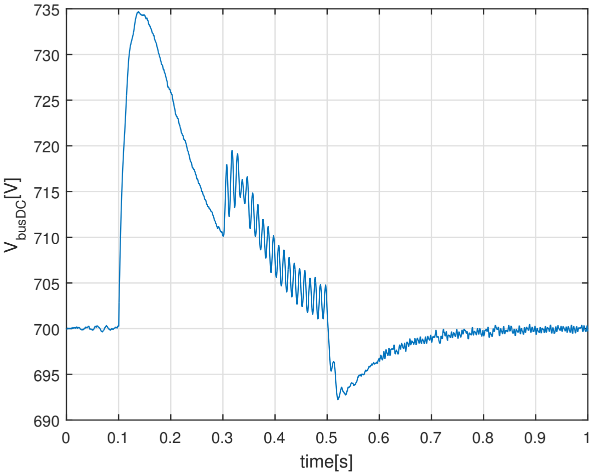

Figure 2.73 – DC link voltage with 25kW setpoint step at t=0.1s, 50% 1-phase voltage dip from t=0.3s to t=0.5s, addition of 5% of 5th harmonic and 3% of 7th harmonic from t=0.6s

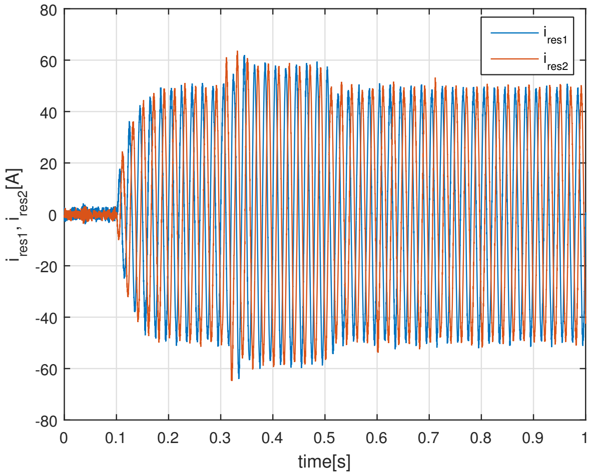

Figure 2.74 – Grid currents with 25kW setpoint step at t=0.1s, 50% 1-phase voltage dip from t=0.3s to t=0.5s, addition of 5% of 5th harmonic and 3% of 7th harmonic from t=0.6s

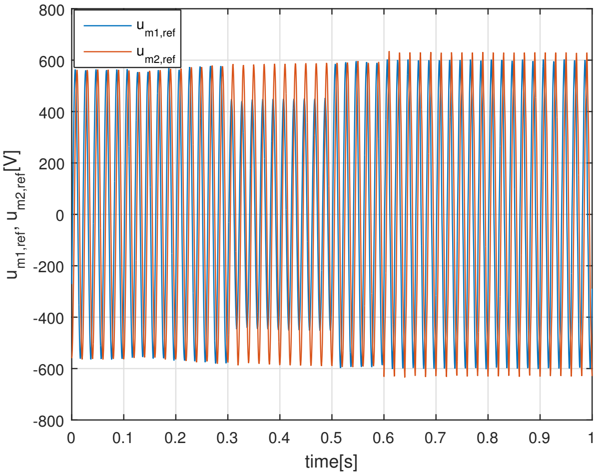

Figure 2.75 – Reference line voltages (output of PR) with 25kW setpoint step at t=0.1s, 50% 1-phase voltage dip from t=0.3s to t=0.5s, addition of 5% of 5th harmonic and 3% of 7th harmonic from t=0.6s

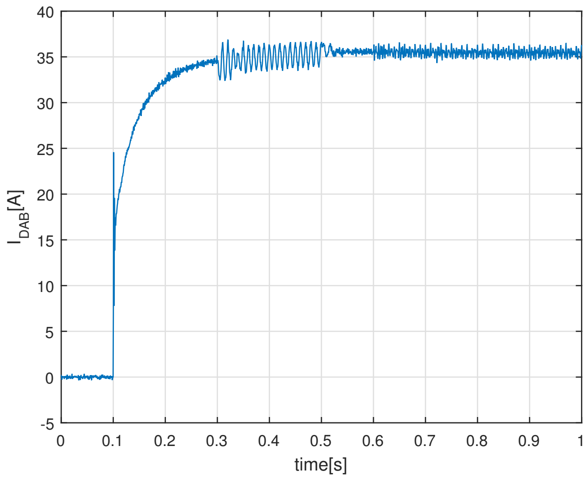

Figure 2.76 – Output current of DAB converter with 25kW setpoint step at t=0.1s, 50% 1-phase voltage dip from t=0.3s to t=0.5s, addition of 5% of 5th harmonic and 3% of 7th harmonic from t=0.6s

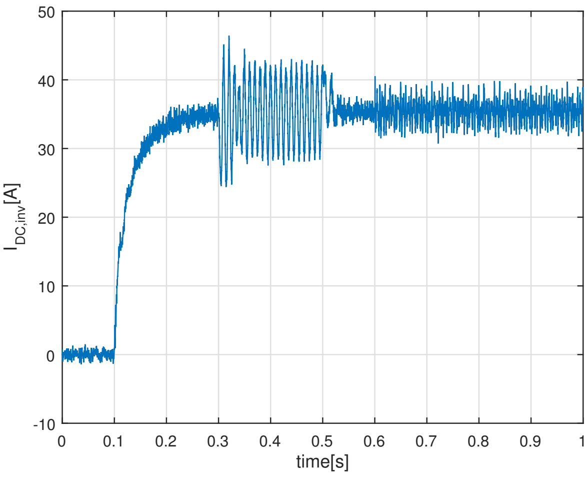

Figure 2.77 – DC side inverter current with 25kW setpoint step at t=0.1s, 50% 1-phase voltage dip from t=0.3s to t=0.5s, addition of 5% of 5th harmonic and 3% of 7th harmonic from t=0.6s

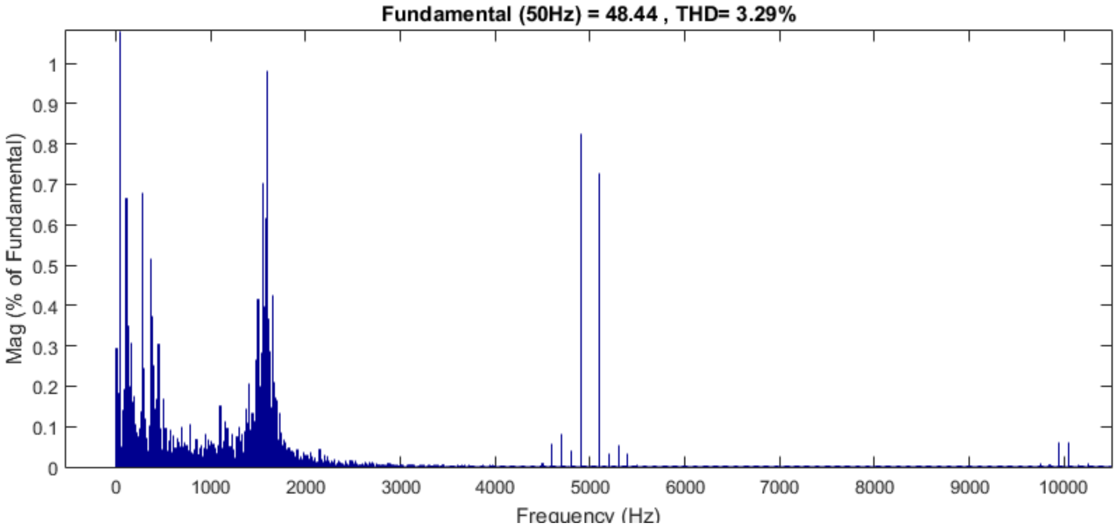

Figure 2.78 – Fourier analysis of i_{res1} from t=0.7s to t=1s

2.6.2 Power Setpoints Following

A series of ramps are given as reference for active and reactive power. Results are depicted in Figures 2.79 and 2.80.
They show that the BESS can follow a series of subsequent setpoints rather effectively and that the active and reactive powers can be controlled independently. The output power lags around 20ms in average behind the command. The maximum power ramping rate achieved is about 4ms/kW[3].

---

3. This corresponds to the typical ramping rate of the SAFT Li-ion battery used by Laborelec.

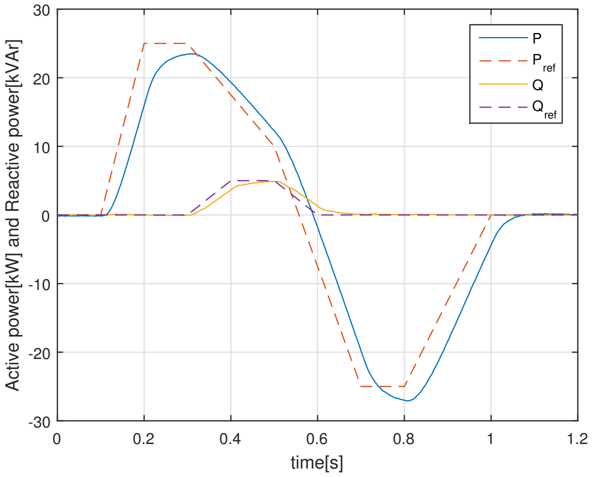

Figure 2.79 – Output active and reactive powers (solid lines) after several setpoint ramps (dashed lines)

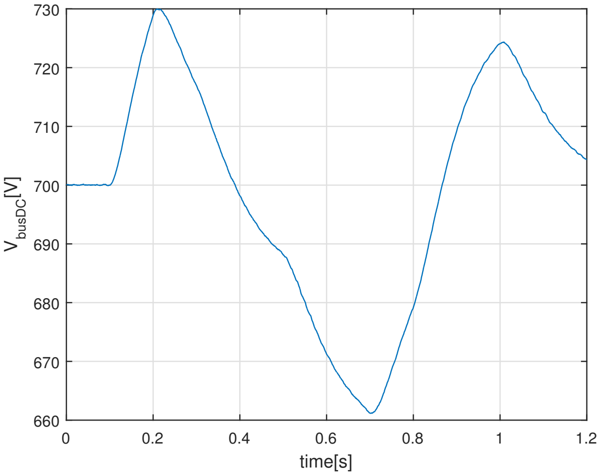

Figure 2.80 – DC link voltage after several setpoint ramps

Chapter 3

Applications of BESS in Microgrids

3.1 Overview

Due to the variability and intermittency of renewable distributed generators (DGs), the operation and control of renewable microgrids is challenging. The weather-dependent DGs may not be able to accommodate the constantly varying load very well and their fluctuation may even cause instability. Thus, ESS are very important in microgrids, especially for renewable microgrids. Since an ESS can operate as load or generator when it is in charging or discharging mode, it is able to balance the power in the microgrid and reduce the impact of any fluctuation. This improves the stability of the microgrid significantly [6]. The general applications and configurations of ESS in microgrids are presented hereafter, BESS being one choice of technology among others. The suited application for an ESS depends on its energy capacity, power rating and response time.

For different applications, the configuration of ESS may need to be different. There are two different configurations of ESS in a renewable microgrid : the **aggregated ESS** and **distributed ESS**. The different structure determines their performance and applications.

An aggregated ESS is a big energy storage facility with dedicated housing in the microgrid. It has usually very large energy capacity and power capability. According to some research [49, 50], an aggregated ESS is more capable of suppressing the power fluctuation in the microgrid than a distributed ESS. This is because the power output of the entire renewable farm is usually more stable than each individual unit (averaging effect). Besides fluctuation suppression, aggreggated ESS also perform energy management features, such as load leveling and peak shifting [6].

There are two different configurations of distributed ESS. One is the distributed ESS on generator side which helps the DGs to smoothen output power. Another type is the distributed ESS on load side which allows to reduce the load variation and manage energy for different purposes. Distributed ESS are smaller than aggreggated ESS because they only handle a single (or a small group) renewable generation unit or load. When used with a renewable generation unit, the distributed ESS is usually connected to the same DC link, behind the grid-side inverter. In this configuration, the ESS helps to have a stable DC link votlage by compensating the fluctuation of renewable generation. As mentioned before, a distributed ESS is not as powerful as an aggregated ESS for mitigating the fluctuation of renewables, but the distributed ESS is easier to be expanded and maintained [6].

An ESS is useful for managing energy and improving the stability and economy of a microgrid system. The major energy management functions include **load leveling** and **peak shifting**. They are widely used to mitigate load fluctuations and improve power quality. Load leveling and peak shifting are similar. Both of them deal with the variation of demand. However, the load leveling is more focused on short-term fluctuation, while peak shifting is more for the long-term (24 h) variation. An example of load leveling is depicted in Figure 3.1. In this way, load leveling improves the efficiency and power quality of the microgrid [6].

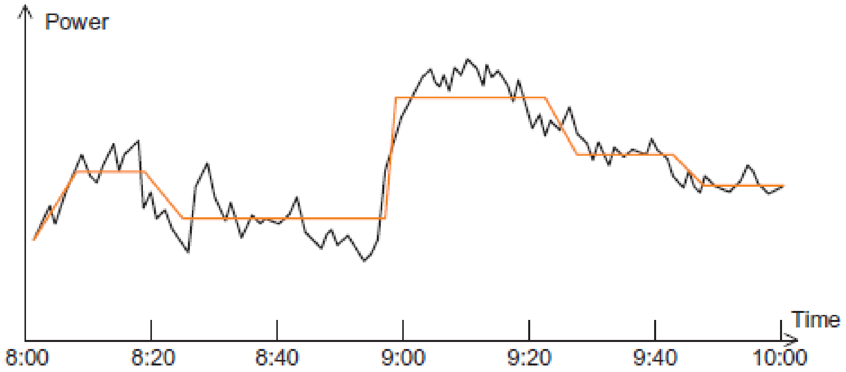

Figure 3.1 – Principle of load leveling : load consumption without ESS (black) and load consumption with ESS (red) (Source : [6]).

ESS can also be used for **fluctuation suppression**, as already mentioned before. The principle is similar to load leveling and peak shifting but with the control being over the generation of renewable units.

Uninterruptible power systems (UPS) are another important application of ESS in microgrids, especially renewable microgrids. Renewable sources, such as solar panels and wind turbines, may suddenly stop generating power due to clouds and shading, nightfall or lack of wind. However, start-up of backup generators may take about 10s. During this period, outages may occur in the microgrid. However, if there is ESS in the microgrid, they can supply the loads to ride through the power shortage [6].

ESS can enhance the **low-voltage ride-through** (LVRT) capability of microgrids. When some incidents happen in the microgrid or main grid, the voltage may suddenly drop and cause some DGs to disconnect which may, in a cascading effect, lead to the disconnection of other DGs resulting in a power outage. Therefore, DGs like wind turbines are required to remain connected to the grid for a period during the voltage dip. By cooperating with an ESS, LVRT capability of WTs can be improved. In fact, in case of voltage dip, the grid-side converter of WT cannot transport full power from the generator to the grid. An ESS can be employed to absorb the excess of power. [6].

ESS can be used as **spinning reserve**. The spinning reserve is the amount of unused capacity connected to the microgrid which is responsible for the **frequency regulation** in case of perturbation. Traditionally, the spinning reserve is a concept for synchronous generators. For example, if one generator of the power system is tripped, the active power unbalance will result in a frequency drop. Hence, other generators have to increase their output to contain the frequency. The more reserve is needed, the operating points of generators are further away from the rated value and thus are less efficient. By involving ESS in the spinning reserve, generators can work more closely to their rated values. Frequency regulation is developed further in Section 3.2.

In the case of dq decoupling control, ESS can participate in the **voltage regulation** of the microgrid. The principle is quite similar to frequency regulation but is achieved through reactive power control.

3.2 Frequency Regulation Strategy with BESS

BESS are characterized with fast response time and high flexibility, which makes them suitable for frequency regulation. in fact, BESS can mitigate frequency variations with a faster response than most DGs, such as synchronous generators (SG) driven, for instance, by wind turbines (WT) or hydraulic turbines (HT). If the capacity of the BESS is limited, those SGs can gradually take over the mid-to-long term frequency regulation.
The frequency regulation is usually divided into several subsequent steps [51]:

- **Primary control** consists in changing a generating unit's power as a function of the frequency, according to its *droop* characteristic, determined by the speed governor settings in the case of a SG. The objective of primary control is to re-establish a balance between generation and demand within the synchronous area at a frequency different from the nominal value. The primary control action time is typically 0 to 30s after disturbance of the balance between generation and demand.
- **Secondary control** makes use of a central regulator, modifying the active power set points of generating sets subject to secondary control, in order to restore the system frequency to its setpoint value. By altering the operating points of individual generating units, secondary control ensures that the full reserve of primary control power activated will be made available again. Secondary control operates slower than primary control, in a timeframe of minutes. Its action becomes evident about 30s after a disturbance/event, and ends within 15 min.
- **Tertiary control** is any automatic or manual change in the working points of the generating units participating, in order to restore an adequate secondary control reserve or to provide desired (in terms of economic considerations) allocation of this reserve within the set of generating units in service.

Figure 3.2 illustrates the principles of primary and secondary control. The rate of change of frequency (ROCOF) after the perturbation depends on the inertia of the synchronous area. Thanks to their fast response time, BESS can provide **virtual inertia** by emulating the inertial response of conventional generators. Consequently, they can increase the equivalent inertia of the synchronous area. The strategy developed here is focused solely on virtual inertia and primary control.

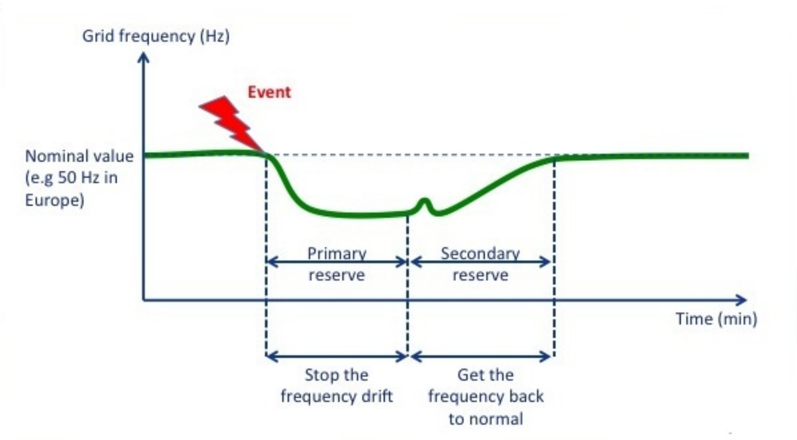

Figure 3.2 – Frequency regulation with primary and secondary reserves (Source : [52])

3.2.1 Virtual Inertial Control

The equation decribing the rotor motion of a synchronous generator (SG) is :

$$J\frac{d\omega_m}{dt} = T_m - T_e \tag{3.1}$$

where J is the total moment of inertia of the rotor mass, ω_m the angular velocity of the rotor, T_m the mechanical torque supplied by the prime mover and and T_e the electrical torque output of the alternator. The electrical frequency ω is linked to the angular veloctiy by $p\omega_m = \omega$ where p is the number of pole pairs of the SG. Rewriting the equation in per unit and in terms of powers :

$$2\frac{H}{\omega_{syn}}\omega_{p.u}(t)\frac{d\omega(t)}{dt} = P_{m,p.u}(t) - P_{e,p.u}(t) \tag{3.2}$$

where H is either the inertia constant of a single SG or the equivalent inertia of a whole synchronous area. This equation indicates that, if the electrical load supplied by the synchronous machine increases, it will compensate by releasing some of its kinetic energy. Hence, the electrical frequency will decrease. The virtual inertial response of the BESS is expressed as follows :

$$\mathit{\Delta} P_{inert} = K_{inert}\frac{df}{dt} \tag{3.3}$$

Including the inertial response of the BESS, Equation (3.2) for the synchronous area becomes

$$(2\frac{H}{f_{syn}}f_{p.u}(t) - K_{inert})\frac{df(t)}{dt} = P_{m,p.u}(t) - P_{e,p.u}(t) \tag{3.4}$$

The equivalent inertia is thus increased if $K_{inert} < 0$.
Using the virtual inertial response, the rate of change of frequency (ROCOF) during the initial period of disturbance (within 5-10s) can be reduced and frequency nadir (the minimum frequency value) can be raised as well.

In order to have an efficient inertial response and to make sure it is not inadvertently activated, the following procedure is used :

- When ROCOF df/dt is smaller than the lower limit a = -0.5 Hz/s (or larger than upper limit b = 0.5 Hz/s) during a time lapse of T_a = 100ms, the inertial response is activated.
- Once activated, the inertial response is not deactivated for at least T_b = 400ms.
- After the delay T_b, if df/dt $\geq$ 0 (or df/dt $\leq$ 0 in case of frequency rise), the inertial response is deactivated.

These settings can be modified in function of the requirements and parameters of the microgrid.

3.2.2 Primary Frequency Control

The primary frequency response of the BESS is also known as the droop response or frequency response reserve. It aims to emulate the governor control of a conventional synchronous generator by taking advantage of the available reserve for the primary frequency regulation. The active power output is controlled in accordance with the system frequency deviation and droop characteristics so that the BESS is able to share the load change with other DGs to ensure that the frequency is restored to the acceptable range within a specified period of time [6]. The expression of the droop response is as follows :

$$\Delta P_{droop} = \frac{1}{R_{droop}} \Delta f = \frac{1}{R_{droop}} (50 - f) \tag{3.5}$$

The droop response is such that the BESS delivers power into the microgrid when f<50Hz and absorbs power when f>50Hz. The performance of frequency regulation depends on the available primary reserve, the droop coefficient R_{droop} as well as the droop characteristics of the other DGs in the microgrid. Figure 3.3 shows how an additional load is shared out between two units with droop control. For a given increase of load, the frequency deviation at the end of the primary regulation depends solely on the droops of the primary reserve units [53].

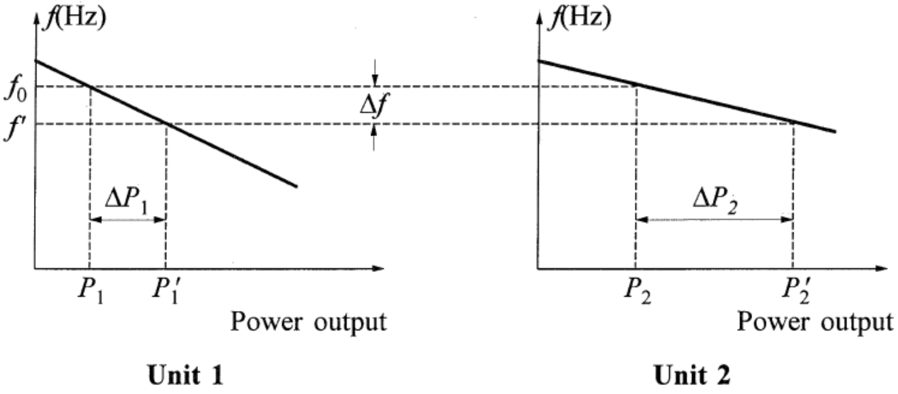

Figure 3.3 – Load sharing by parallel units with droop control (Source : [53])

In the case of a microgrid with several ESS, a variable droop primary frequency regulation based on the real-time SOC of the ESS can be adopted. The coefficient R_{droop} is then a function of the SOC, as depicted in Figure 3.4. In this way, the ESS with more available energy assume a bigger part of the primary control.

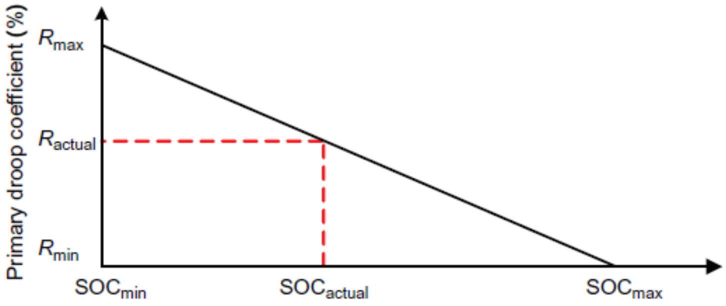

Figure 3.4 – SOC-based dynamic droop curve (Source : [6])

In order to have an efficient primary response and to make sure it is not inadvertently activated, it is only activated when the frequency is smaller than the lower limit c = 49.7 Hz (or higher than upper limit d = 50.3 Hz) during a time lapse of $T_c = 100$ms. This deadband makes sure that the primary regulation is not activated inadvertently. Another choice of deadband can be made in function of the requirements and parameters of the microgrid. Larger frequency deviations are usually expected and tolerated in microgrids than in the main utility grid.

3.2.3 Example and Tests

This frequency regulation strategy is tested with the BESS developed in Chapter 2. The BESS is included in the configuration depicted in Figure 3.5. Initially, the hydraulic turbine is providing 350kW, the total load is consuming 380kW and the main distirbution grid supplies 30kW, so that the microgrid is balanced in terms of active power. The BESS is kept as a frequency regulation reserve, hence it initially provides no power. Then, the microgrid is disconnected from the main distribution grid, resulting in an active power unbalance.

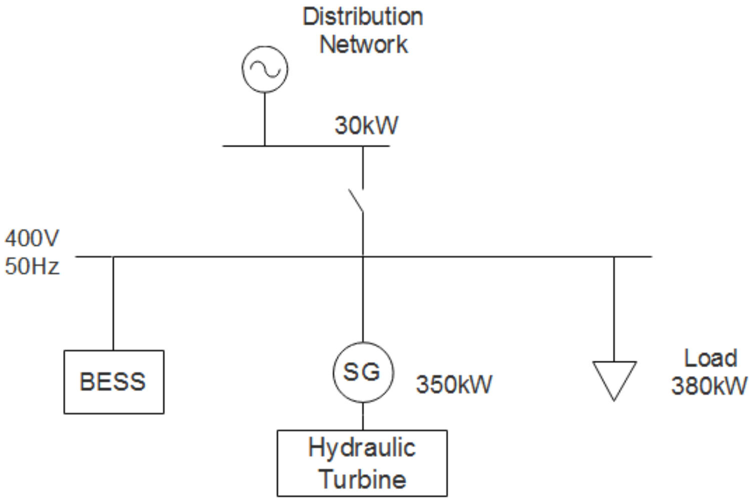

Figure 3.5 – Microgrid configuration for the tested case

The hydraulic turbine is controlled by a governor [1]and is thus part of the primary reserve. The parameters of the BESS and the hydraulic turbine are given in Table 3.1. The output power of the BESS si limited to its nominal value and maximum power ramping rate is set to 4ms/kW.

BESS		Hydraulic Turbine	
Nominal power	25kVA	Nominal power	450kVA
R_{droop}	4.4 mHz/kW	R_{droop}	8.9 mHz/kW (= 8%)
K_{inert}	-85 kW/(Hz/s)	H	3 s [2]

Table 3.1 – Parameters of the BESS and hydraulic turbine

Figures 3.6-3.9 show the results of the simulation under 4 different BESS frequency controls : with the inertial control, with the primary control, with both controls and without control (BESS not participating). A numerical analysis of the results is given in Table 3.2. It can be seen that the BESS significantly improves the frequency response of the microgrid. This is due

---

[1] The Simulink block *Hydraulic Turbine and Governor* is used with its default settings values excepting the static droop.

[2] Typical inertia constant of a hydraulic turbine [54]

to the fact that the BESS brings additional frequency regulation reserve and has a much faster response time than the hydraulic turbine. The inertial control raises the nadir and decreases the ROCOF right after the disturbance. The primary control improves the overall response and has the additional effect to reduce the duration to reach steady state and increases the steady-state frequency.

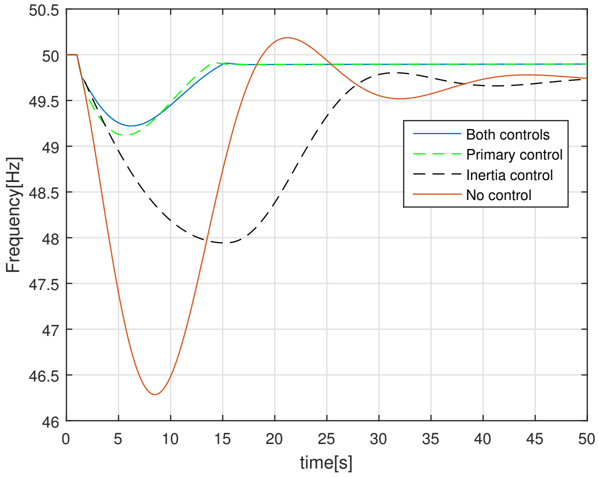

Figure 3.6 – Microgrid frequency response under different frequency controls

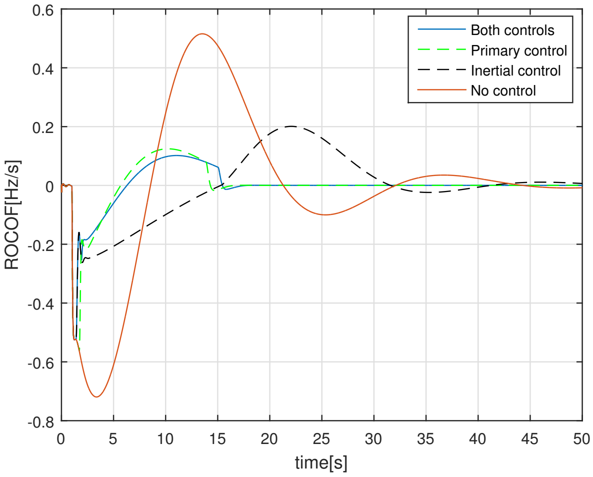

Figure 3.7 – Microgrid ROCOF under different frequency controls

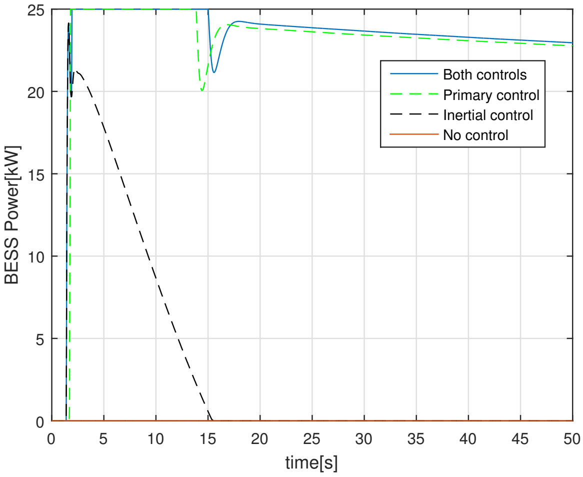

Figure 3.8 – BESS power under different frequency controls

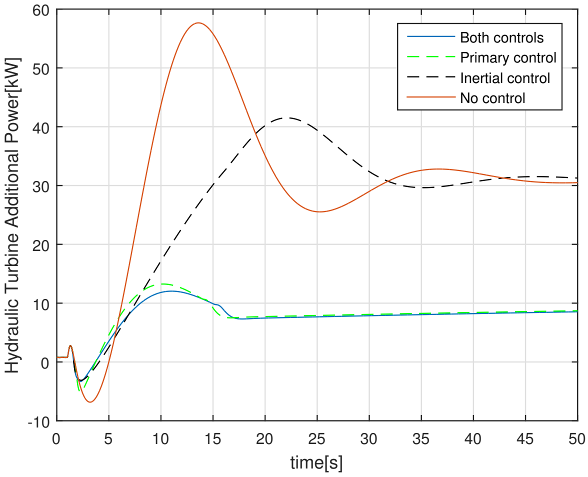

Figure 3.9 – Hydraulic turbine additional power under different frequency controls

	Nadir	Average ROCOF (before nadir)	Steady-state Frequency	Duration to Reach Steady-state[3]
Both controls	49.22 Hz	-0.15 Hz/s	49.91 Hz	14.5 s
Primary control	49.12 Hz	-0.19 Hz/s	49.91 Hz	13.4 s
Inertial control	47.94 Hz	-0.15 Hz/s	49.73 Hz	44.5 s
No control	46.29 Hz	-0.50 Hz/s	49.73 Hz	43.0 s

Table 3.2 – Comparison of numerical results with different controls

---

[3] The steady state is considered to be reached when the frequency stabilizes in a ± 0.05 Hz interval around the steady-state frequency.

Chapter 4

Conclusion

A complete electrical model of a BESS was developed in this thesis. It includes the following elements :

- **Li-ion Battery & BMS** : An equivalent electrical circuit composed of resistors and capacitors was used to model the battery. The value of the parameters obtained in Article [28] for one Li-ion celle were utilized. Then, an example of realistic Li-ion battery model (25kW, 34kWh) was built by mounting a certain number of Li-ion cells in series and parallel. The main purpose of the model is to reproduce the dynamic behaviour of the battery but it also provides a SOC estimation. The BMS is indissociable from its battery and its role is to protect, monitor and stabilize the battery. For instance, the BMS limits the current when the SOC is above/below a certain threshold to provent overcharge/over-discharge.
- **DC/DC Converter** : The topology chosen is the DAB converter with full bridges on both sides. This converter is bidirectional and is a good compromise between efficiency, cost and power denstiy [35]. The lossless model of the converter is used and the simplest modulation technique (phase shift modluation) is considered. LC filters are used on both sides of the converter to smoothen the battery and DC link current. From there, an average dynamic model of the converter is built and compared with the full model.
- **Battery-side Controller** : A PI controller regulates the output power of the battery by controlling the phase shift of the DAB converter.
- **DC link** : The DC link is simply composed of a relatively large capacitance. It allows to filter the current harmonics which are not totally eliminated by the LC filters. It also provides some sort of decoupling between the battery and grid sides of the sytem. In larger systems, other DERs or ESS can be connected to the same DC link.
- **DC/AC Converter** : The topology chosen is the three-phase voltage source inverter with PWM modulation. It allows for bidirectional power flow. LC filters are placed on both sides of the converter. The AC side filter is particularly important as it directly impacts the harmonic content of the grid current.
- **Grid-side Controller** : This controller is composed of an outer slower control loop and an inner faster control loop. The DC link and Q controllers form the outer loop. They are both PI controllers and respectively regulate the DC link voltage (thus active power balance) and reactive power. They generate the reference currents in the dq frame. The inner loop contols the the grid current. The control is performed in the stationary ($\alpha\beta$) frame with PR controllers and the 5th and 7th harmonic currents are regulated as well. This inner loop generates the modulating signal for the inverter. The parameters of the PR controllers have to be chosen carefully to make sure there is no instability due to resonance with the output LC filter. Synchronization is performed with an EPLL which is more robust against harmonics and unbalance than classic PLLs.

Tests on the overall system showed that, with the chosen parameters values, the BESS is robust against perturbations such as unbalance and harmonics. Moreover, the harmonic content of the grid current is relatively low.

The model was tested on a real-time simulation platform (Power hardware in the loop, owned by Laborelec). The average dynamic models were used for both converters to reduce computational cost. The fact that the model could be successfully simulated in real-time (no overruns) proves the feasibility of the designed controllers.

Finally, a small simple microgrid was built, composed of the BESS, a group of loads and a hydraulic turbine. For the test, the microgrid is considered to be disconnected from the main utility grid, which implies an active power unbalance. The tests show that developed BESS model can be effectively be integrated in a larger power system and work properly. Moreover, the results proves the interest of using a BESS for frequency regulation in a microgrid. Since the BESS provides additional frequency regulation reserve and has a much faster response time than the hydraulic turbine, it significantly improves the frequency response of the microgrid.

As mentioned in Section 1.3, this model will be utilized by Laborelec for some of their projects. They will have the opportunity to further improve and validate this model by running experimental tests on Li-ion batteries and simulate the model in more complex power systems. The approach of the model is rather systemic and does not go into the precise design of the power electronics components. This emphasis of the model was intentionally placed on dynamic performances and power quality considerations, but other aspects such as efficiency and costs could be examined in more details for the model.

Appendix A

Three-phase Inverter DC Current

Starting from the three balanced phase voltages given in Equations (2.44-2.46), the two line voltages are then :

$$\langle v_{m1}(t)\rangle = m_1(t)V_{DC}/2 = U_m sin(\omega t - \pi/6 + \varphi) \tag{A.1}$$

$$\langle v_{m2}(t)\rangle = m_2(t)V_{DC}/2 = U_m sin(\omega t - \pi/2 + \varphi) \tag{A.2}$$

If the currents are balanced as well, we have :

$$\langle i'_a(t)\rangle = I' sin(\omega t + \psi) \tag{A.3}$$

$$\langle i'_b(t)\rangle = I' sin(\omega t - 2\pi/3 + \psi) \tag{A.4}$$

Finally, the power conservation equation (2.40) becomes

$$\begin{aligned} V_{DC}\langle i(t)\rangle &= U_m I' sin(\omega t - \pi/6 + \varphi) sin(\omega t + \psi) + U_m I' sin(\omega t - \pi/2 + \varphi) sin(\omega t - 2\pi/3 + \psi) \\ &= \frac{U_m I'}{2}(cos(\varphi - \psi - \pi/6) - cos(2\omega t + \varphi + \psi - \pi/6)) + \\ &\frac{U_m I'}{2}(cos(\varphi - \psi + \pi/6) - cos(2\omega t + \varphi + \psi - 7\pi/6)) \\ &= \frac{U_m I'}{2}(cos(\varphi - \psi - \pi/6) + cos(\varphi - \psi + \pi/6)) \end{aligned} \tag{A.5}$$

This proves that, in case of balanced system, the DC current has no 2ω component, unlike with single-phase inverter. However, if the system is unbalanced, there is a 2ω component.

Appendix B

Influence of DC/DC Converter and Battery-side Controller Parameters

The influence of the DC/DC converter and battery-side controller parameters is examined in this appendix. The output battery power P_{LV} and DC link power P_{HV} are anaalyzed for different set of parameters. The parameters are referred to the diagram shown in Figure 2.18. The system is tested in closed-loop. Excepting the parameter of interest, the values of the other parameters are the same as in Subsection 2.3.6.

DAB Converter Parameters

Figures B.1 and B.2 show that increasing the filter capacitances decreases the overshoots of P_{LV} and P_{HV}. Figures B.3 and B.4 show that increasing the filter inductances increases the initial oscillations and overshoots. In fact, as shown in Equation 2.19, the damping ratio increases when C increases and L decreases. For optimal design, the capacitance should thus be as large as possible, taking into account constraints of size and cost. The inductance should not to be too large, but large enough to effectively filter HF components.

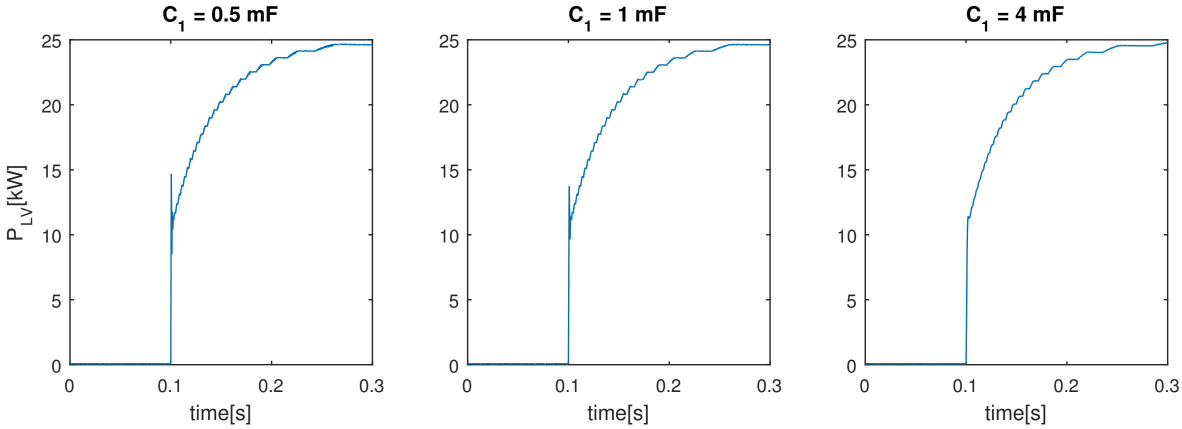

Figure B.1 – P_{LV} after a P_{ref} step of 25kW for different values of C_1

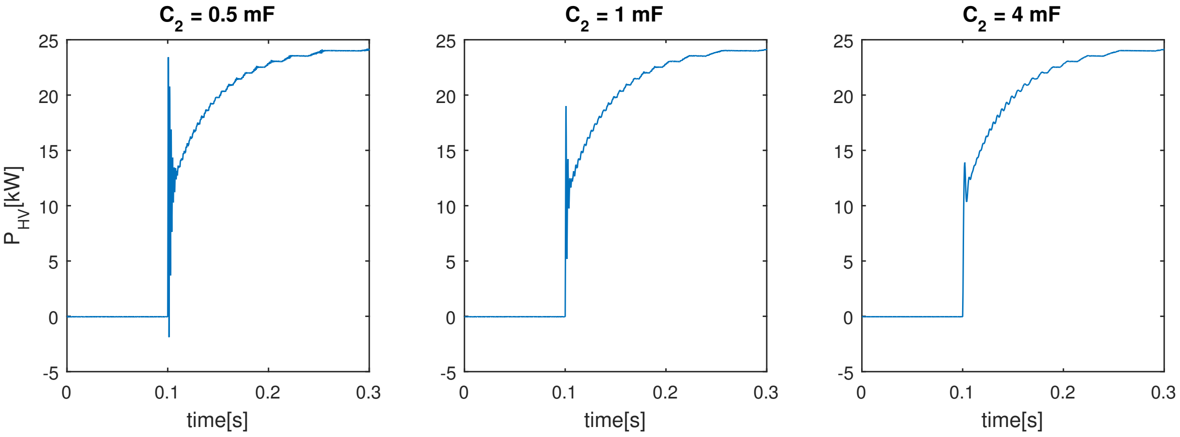

Figure B.2 – P_{HV} after a P_{ref} step of 25kW for different values of C_2

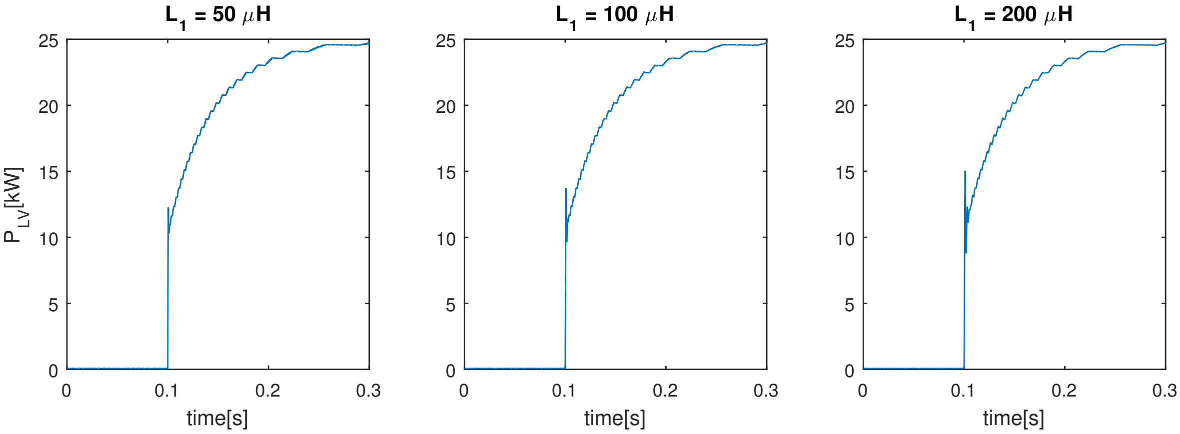

Figure B.3 – P_{LV} after a P_{ref} step of 25kW for different values of L_1

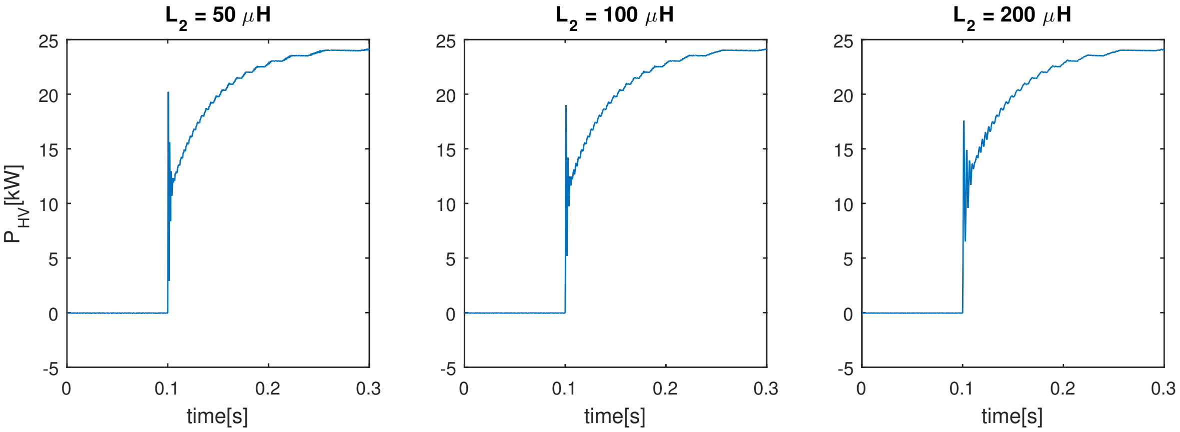

Figure B.4 – P_{HV} after a P_{ref} step of 25kW for different values of L_2

Battery-side Controller Paremeters

Figures B.5 and B.6 show that increasing the proportional gain G accelerates the response of the system but raises the overshoot. Figures B.7 and B.8 show that decreasing τ accelerates the response of the system. However, if τ is further decreased, an overshoot and oscillations around the stedy-state value will appear.

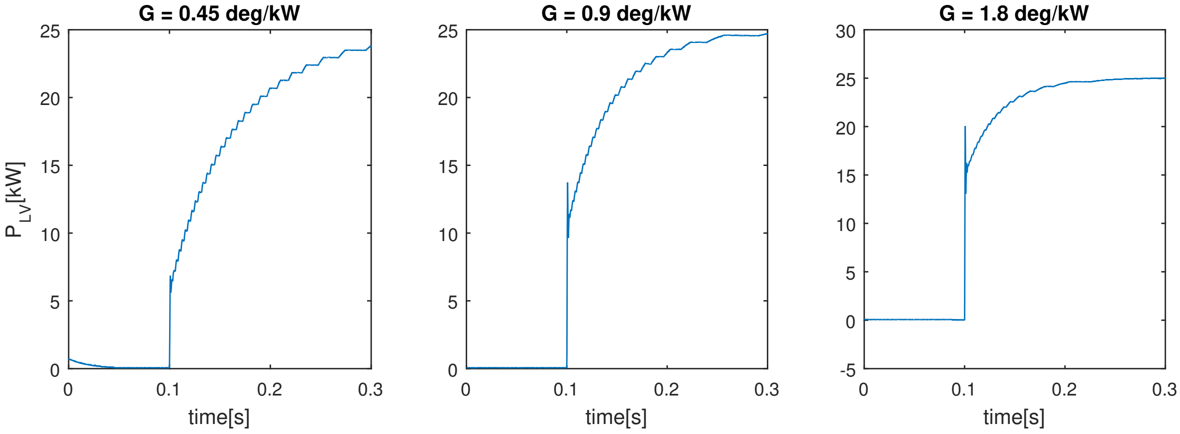

Figure B.5 – P_{LV} after a P_{ref} step of 25kW for different values of G

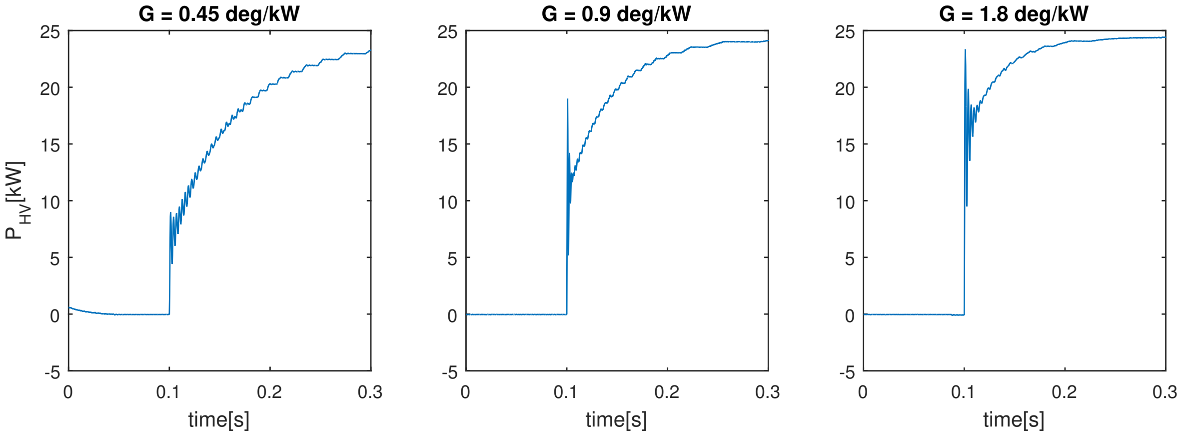

Figure B.6 – P_{HV} after a P_{ref} step of 25kW for different values of G

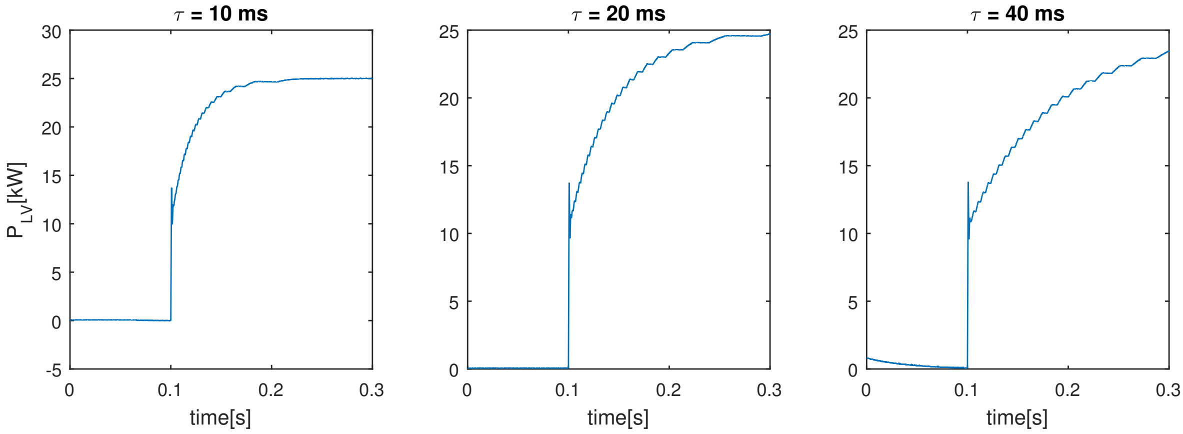

Figure B.7 – P_{LV} after a P_{ref} step of 25kW for different values of τ

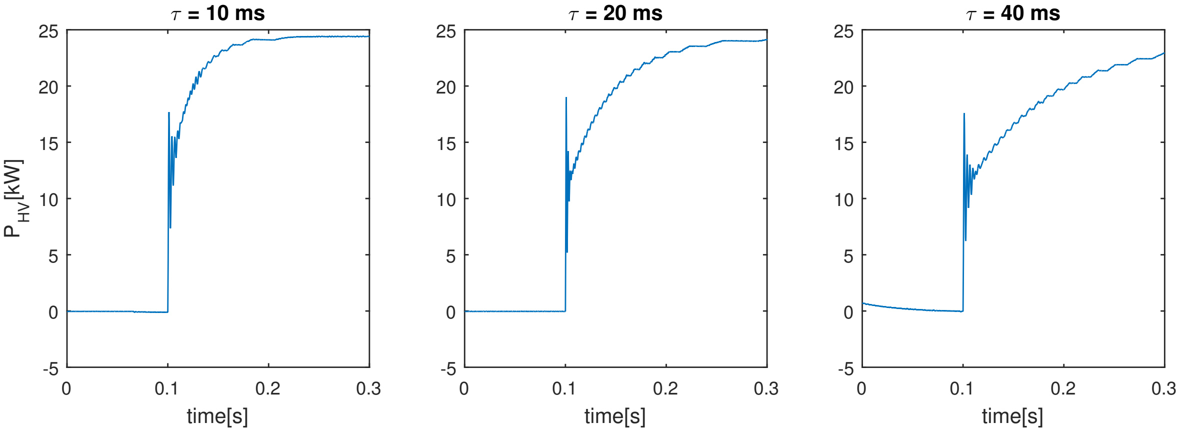

Figure B.8 – P_{HV} after a P_{ref} step of 25kW for different values of τ

Appendix C

Influence of Grid Impendance, Output LC filter and Grid-side Controller Paremeters

The influence of the grid impedance, output LC filter and grid-side controller parameters is examined in this appendix. The effect of these paremeters on the stability of the current control is considered. The parameters are referred to the diagram shown in Figure 2.43 and the controller transfer function given in Equation 2.60. The system is tested in closed-loop. Excepting the parameter of interest, the values of the other parameters are the same as in Subsections 2.4.3 and 2.5.5.

Grid Impedance

The variation of the natural frequency f_{n2} (Eq 2.53) of the output LC filter with the grid inductance L is depicted in Figure C.1. Figures C.2 and C.3 show how that there are overall more harmonics when L is smaller. The influence of the grid resistance R on the harmonic content is negligible.

Figure C.4 shows the position of the poles of the closed-loop system as a function of L. Increasing L gets all the poles closer to the imaginary axis. When a certain value of L is reached, two poles have positive real part, hence the system becomes unstable. On the other hand, as shown in Figure C.5, R has a stabilizing effect and, as it increases, gets the poles further away from the imaginary axis. If the resistance is too small, the system might be unstable.

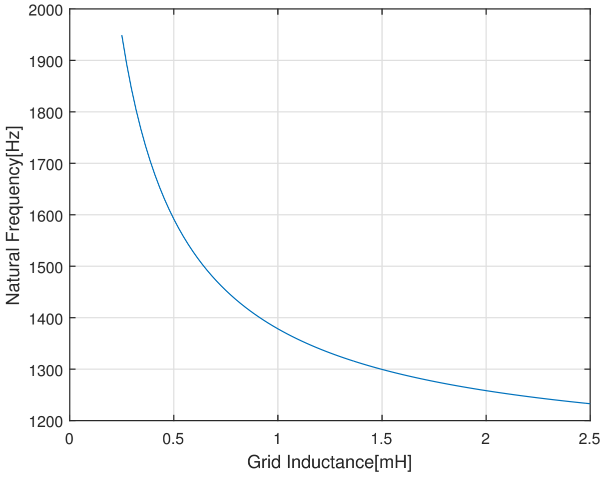

Figure C.1 – Variation of f_{n2} with L

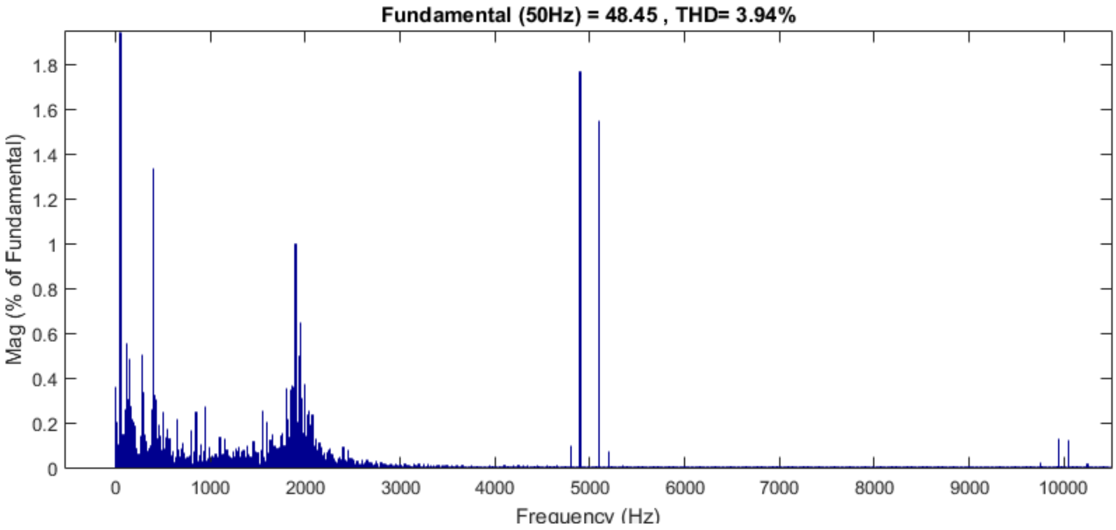

Figure C.2 – Fourier analysis of i_{res1} with $L = 0.25\text{mH}$

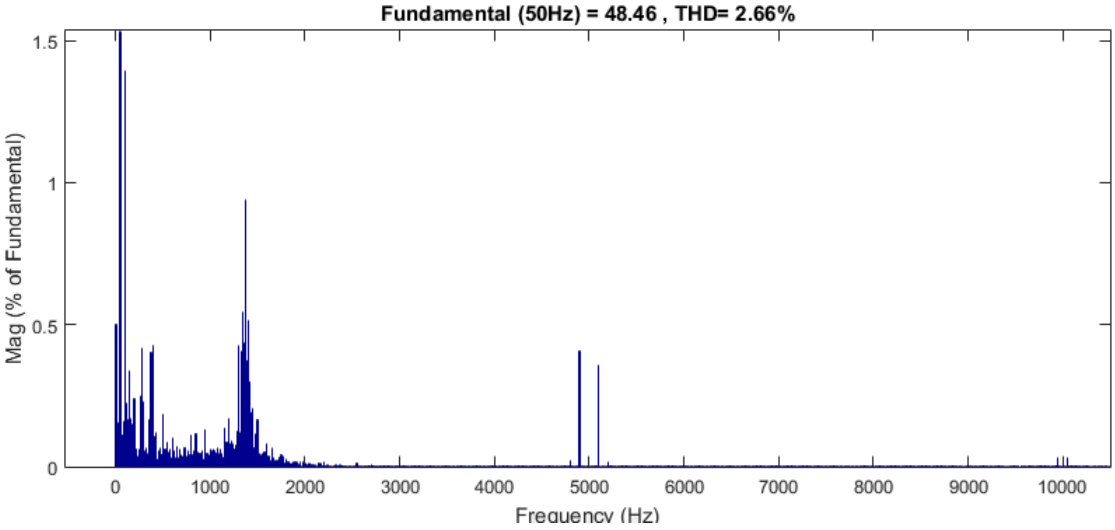

Figure C.3 – Fourier analysis of i_{res1} with $L = 1\text{mH}$

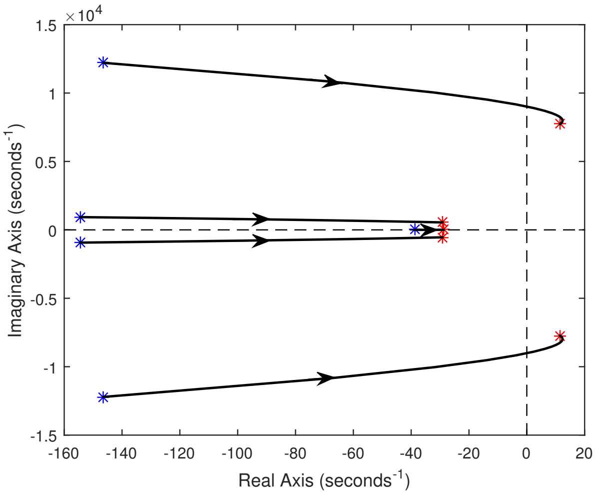

Figure C.4 – Poles trajectory when L varies from 0.25mH (blue) to 2.5mH (red)

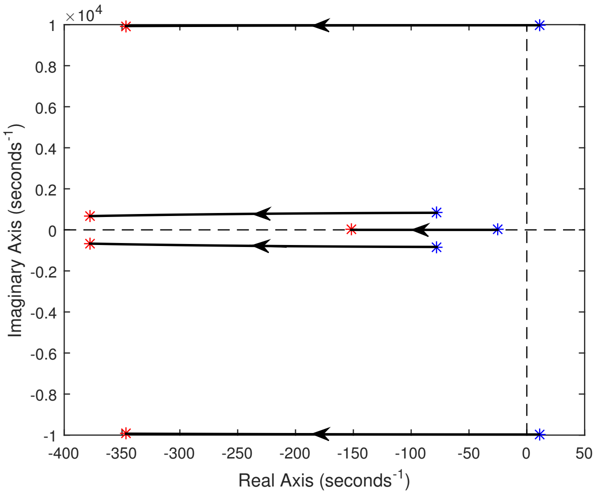

Figure C.5 – Poles trajectory when R varies from 0.08Ω (blue) to 0.8Ω (red)

Output LC Filter Parameters

Figures C.6 and C.7 show that increasing L_2 reduces the overall harmonic content. Figures C.8 and C.9 show that increasing C_2 reducs the high order harmonics but increases the lower order harmonics.

Figure C.10 show that increasing L_2 drives some poles away from the imaginary axis while it gets other poles closer. At $L_2 = 0.25$mH, the sytem is unstable. Figure C.11 show that C_2 has basically no influence on stability.

As a result, for efficient filtering, L_2 should be as large possible taking into accounts constraints of size and cost. C_2 has to be chosen carefully, depending on the requirements in terms of harmonics.

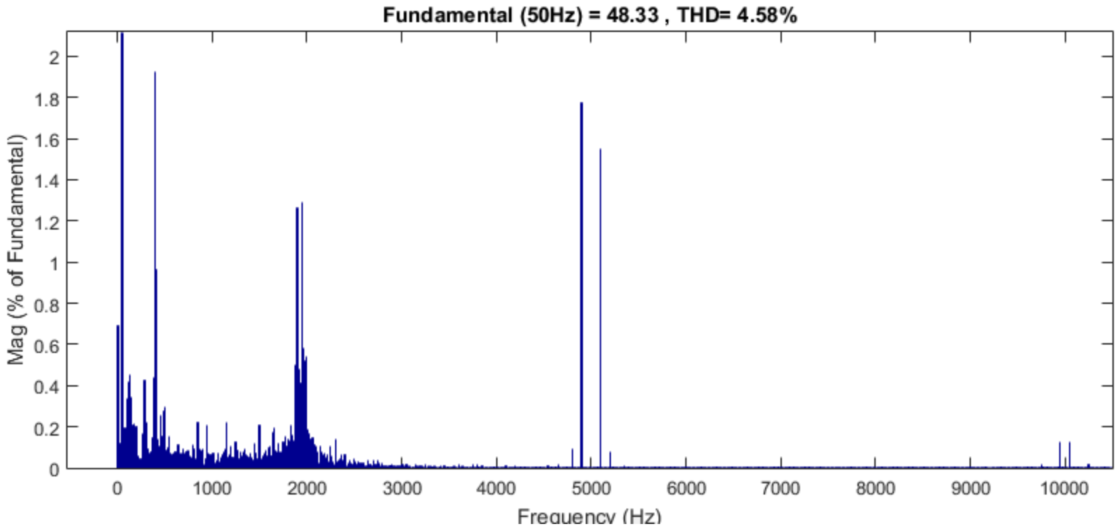

Figure C.6 – Fourier analysis of i_{res1} with $L_2 = 0.25$mH

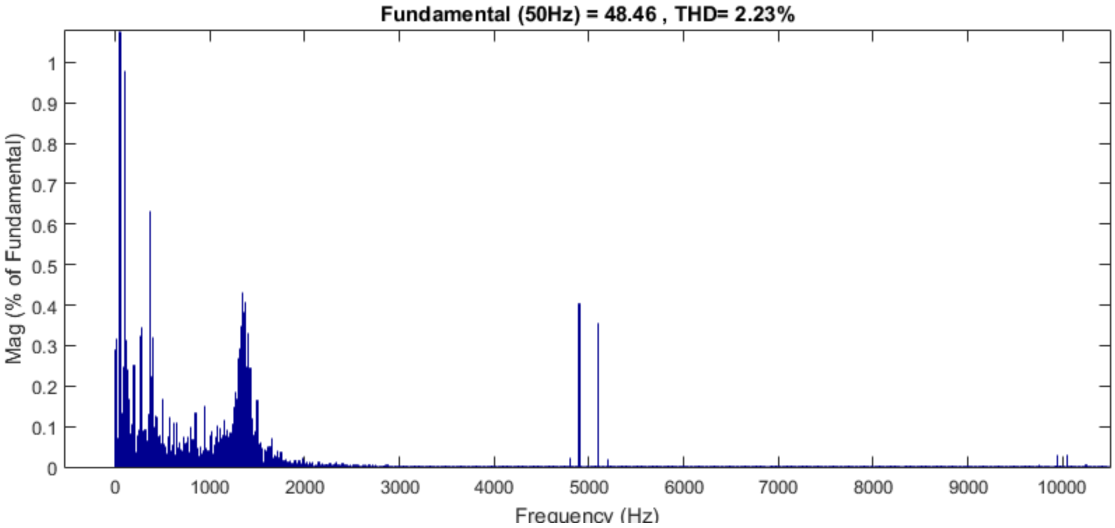

Figure C.7 – Fourier analysis of i_{res1} with $L_2 = 1\text{mH}$

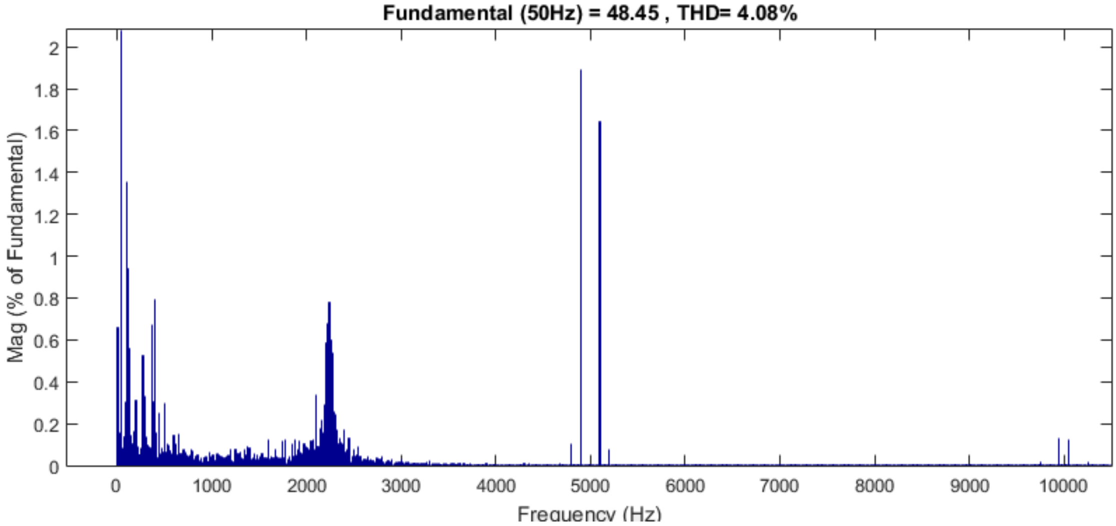

Figure C.8 – Fourier analysis of i_{res1} with $C_2 = 20\mu\text{F}$

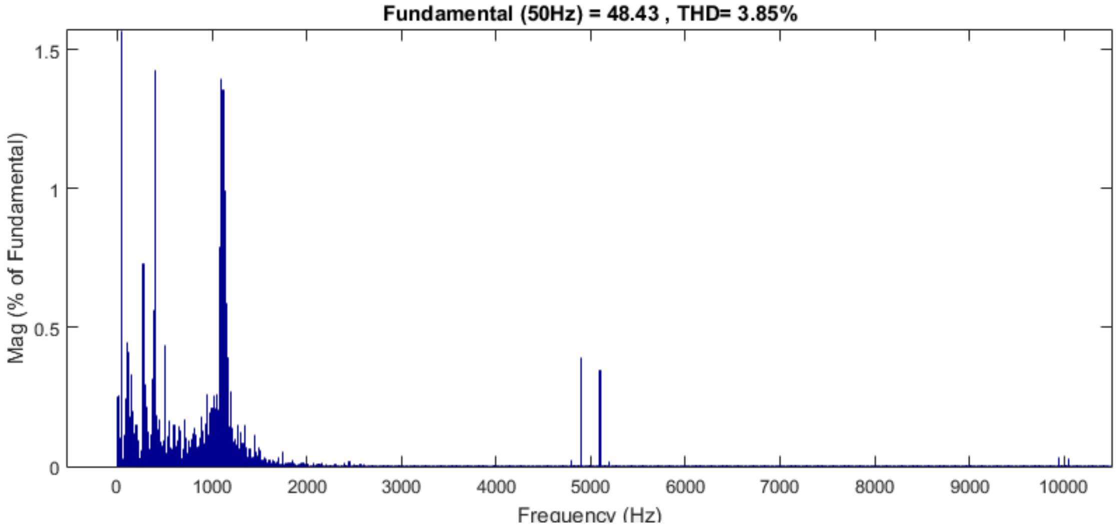

Figure C.9 – Fourier analysis of i_{res1} with $C_2 = 80\mu\text{F}$

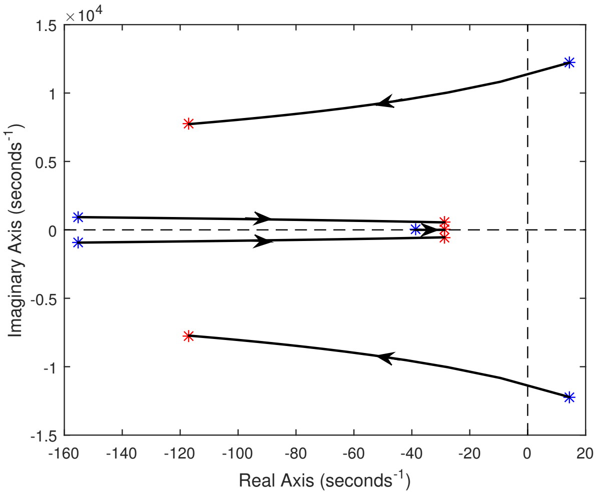

Figure C.10 – Poles trajectory when L_2 varies from 0.25mH (blue) to 2.5mH (red)

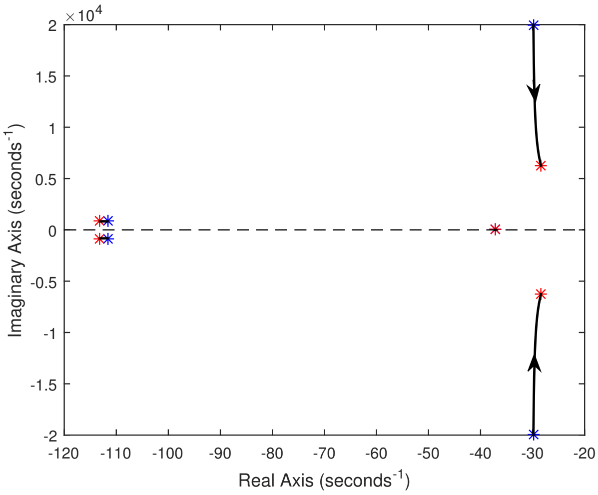

Figure C.11 – Poles trajectory when C_2 varies from 10μF (blue) to 100μF (red)

Grid-side Controller Parameters

Figure C.12 shows that dynamics is influenced by the parameter K_I. Increasing K_I accelerates the response but can lead to an overshoot if it is too high. Parameters K_P and ω_c do not influence this kind of test as the gain at the fundamental frequency is mainly determined by K_I.

Figures C.13, C.14 and C.15 show that all the paremeters influence the stability by driving some poles away while taking other poles closer. The choice of parameters to ensure and optimize stability performances is thus complex.

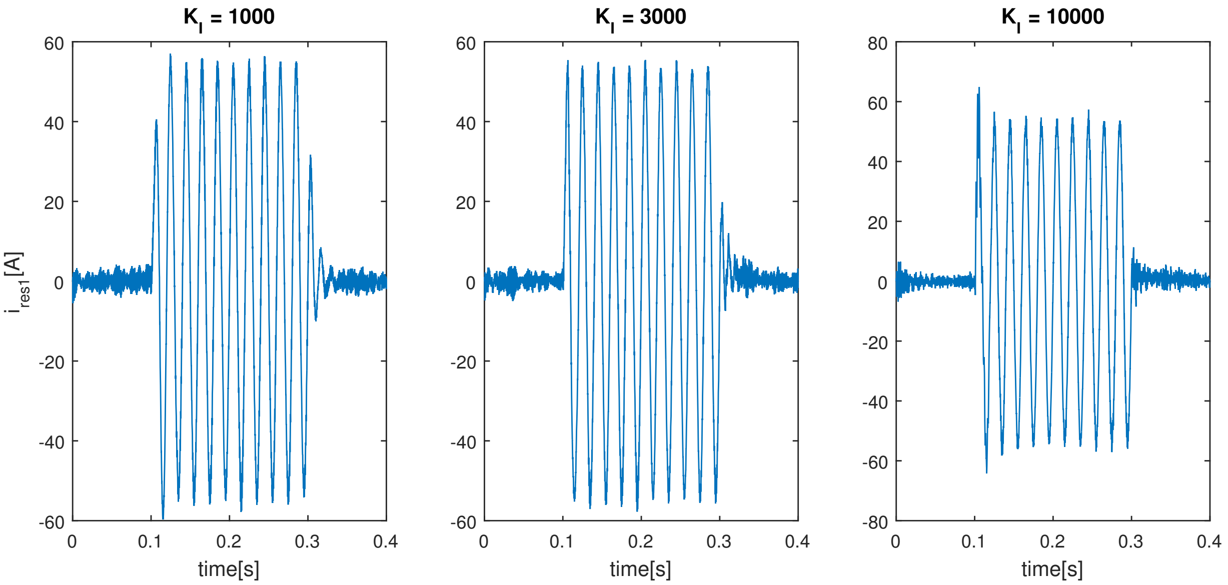

Figure C.12 – Grid current i_{res1} with a pulse of id,ref from t=0.1s to t=0.3s with different values of K_I

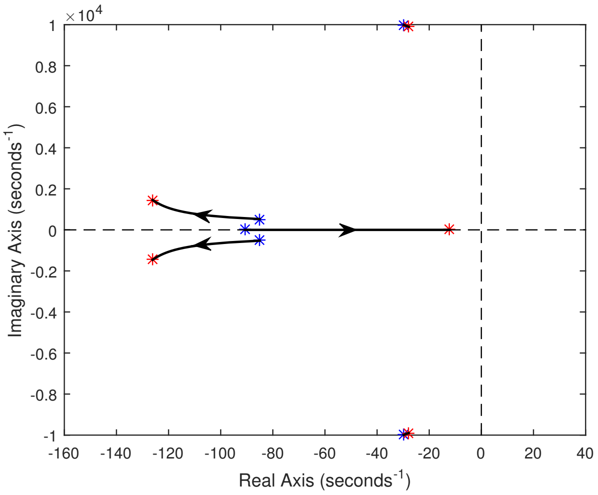

Figure C.13 – Poles trajectory when K_I varies from 1000 (blue) to 10000 (red)

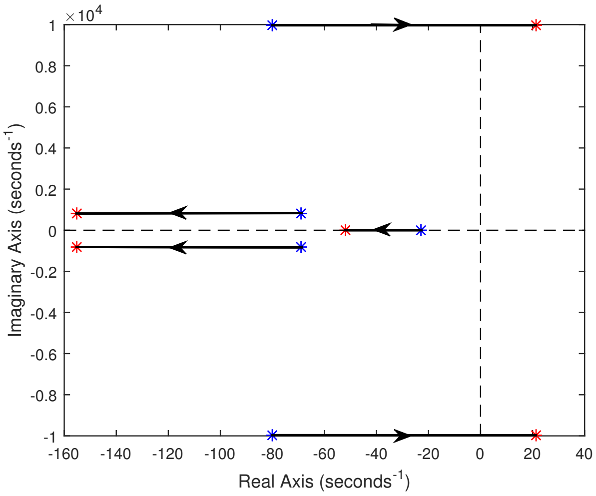

Figure C.14 – Poles trajectory when K_P varies from 0 (blue) 0.2 (red)

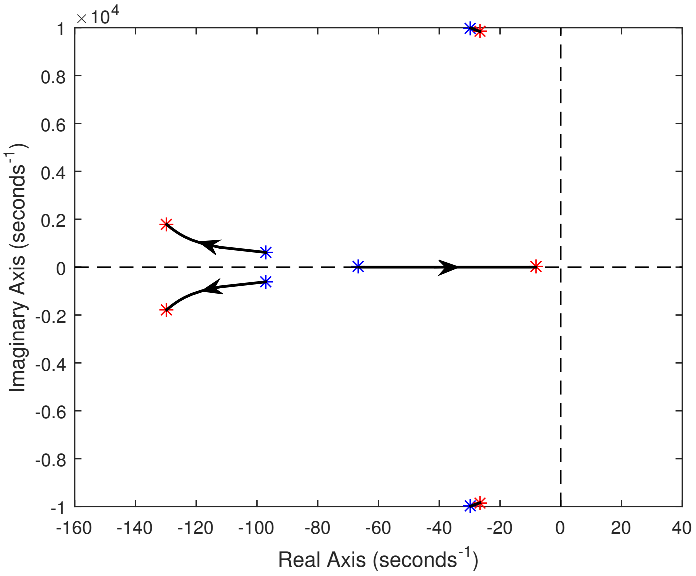

Figure C.15 – Poles trajectory when ω_c varies from 0.05 (blue) 0.5 (red)

Appendix D

Influence of DC Link Controller Parameters

The influence of the DC link controller parameters is examined in this appendix. Excepting the parameter of interest, the values of the other parameters are the same as those developed in Chapter 2.

Figure D.1 shows that when the proportional gain G is too high, HF oscillations from the inverter may be amplified and impact the DC link voltage. Figure D.2 shows that if the proportional gain is too small (with respect to integral gain), a power overshoot will occur. G also influences the response time of the system.

Figure D.3 shows that τ, the controller response time, influences the peak DC link voltage and the time for the DC link voltage to be restored to its reference value. τ also influences the response time and may lead to a nonlinear power increase if it is too small.

For a chosen set of (G,τ), the DC link capacitance must be chosen to have acceptable deviations of the DC link voltage.

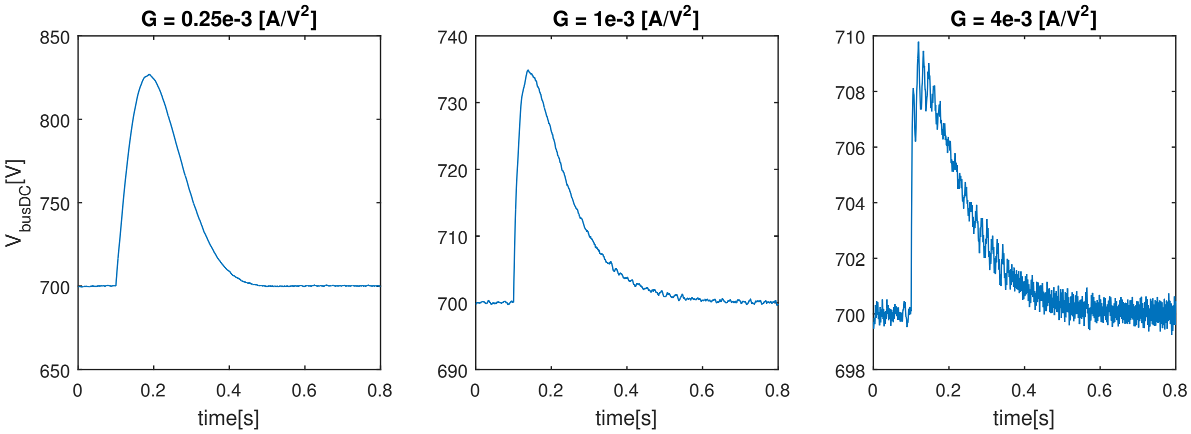

Figure D.1 – Dc link voltage after a 25kW P_{ref} step for different values of G

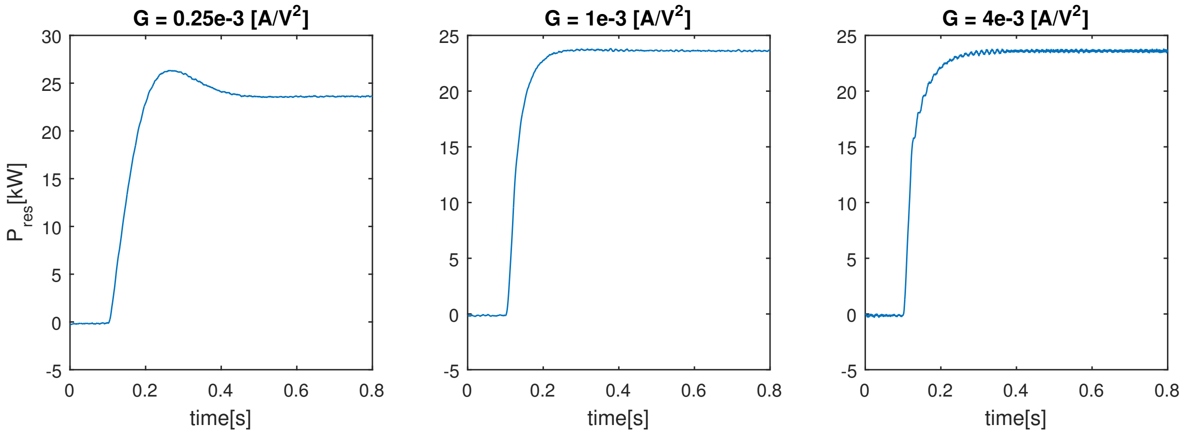

Figure D.2 – Output power P_{res} after a 25kW P_{ref} step for different values of G

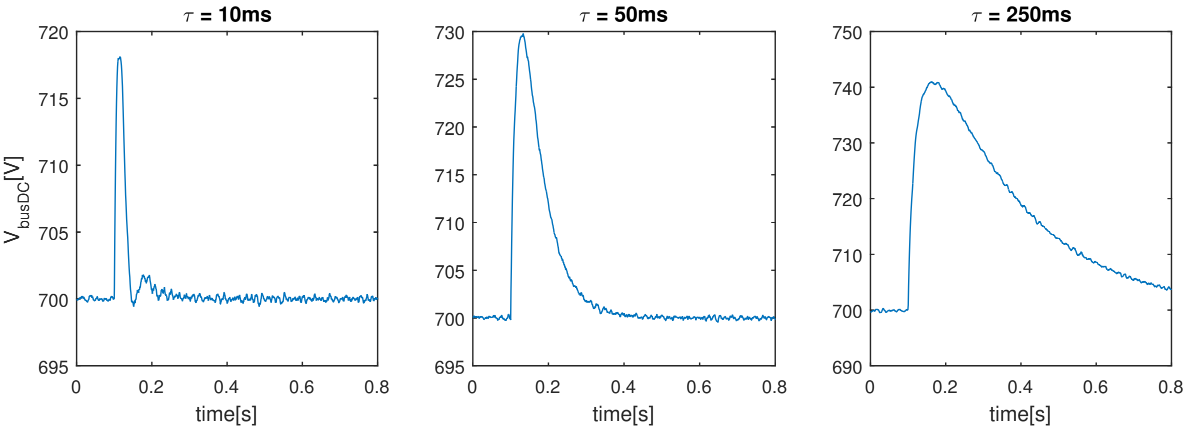

Figure D.3 – Dc link voltage after a 25kW P_{ref} step for different values of τ

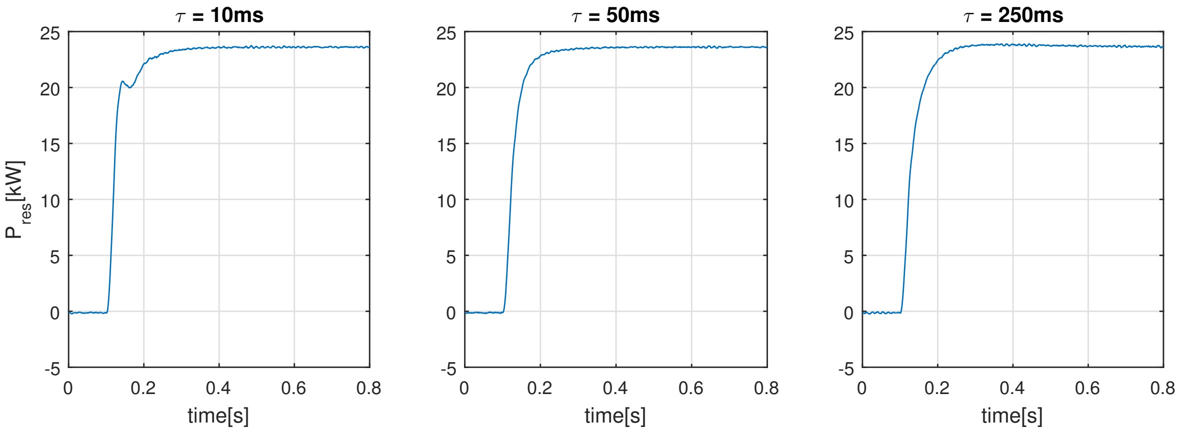

Figure D.4 – Output power P_{res} after a 25kW P_{ref} step for different values of τ

Bibliography

[1] "History Of Batteries : A Timeline" (2014, June). Retrieved from http://www.upsbatterycenter.com/blog/history-batteries-timeline/.

[2] Bruno Scrosati and Jürgen Garche, "Lithium batteries : status, prospects and future", *Journal of Power Sources*, vol. 195, pp. 2419–2430, 2010.

[3] Epec, "Battery cell comparison". Retrieved from http://www.epectec.com/batteries/cell-comparison.html, consulted the 4th of May 2017

[4] James F. Rohan, Maksudul Hasan, Sanjay Patil, Declan P. Casey and Tomás Clancy, "Energy Storage: Battery Materials and Architectures at the Nanoscale", *ICT - Energy - Concepts Towards Zero - Power Information and Communication Technology*, 2014.

[5] U.S. Department of Energy, "The History of the Electric Car". Retrieved from https://www.energy.gov/public-services/vehicles, consulted the 5th of May 2017.

[6] David W. Gao, *Energy Storage for Sustainable Microgrid.* Academic Press, 2015.

[7] Gold Peak Industries Ltd., "Lithium Ion Technical Book", 2000.

[8] Cutler Cleveland and Christopher J. Morris, *Dictionary of Energy.* Amsterdam: Elsevier, p. 473, 2006.

[9] "Car Prototype Generates Electricity, And Cash" (2007, December), *Science Daily.* Retrieved from https://www.sciencedaily.com/releases/2007/12/071203133532.htm.

[10] Dan T.Ton and Merill A.Smith, "The U.S. Department of Energy Microgrid Initiative", *The Electricity Journal*, vol. 25, pp. 84-94, 2012.

[11] Xiong Liu, Peng Wang and Poh Chiang Loh, "A Hybrid AC/DC Microgrid", Nanyang Technological University, Singapore, 2010.

[12] Claudio A. Cañizares, "Trends in Microgrid Control", *IEEE Transactions on Smart Grid*, vol. 5, no. 4, pp. 1905-1919, 2014.

[13] U.S. Department of Energy, "DOE Global Energy Storage Database". Retrieved from www.energystorageexchange.org.

[14] R.S Khurmi, *Materials Science.* S.Chand & Company, 2014.

[15] Ioannis Hadjipaschalis, Andreas Poullikkas and Venizelos Efthimiou, "Overview of current and future energy storage technologies for electric power applications", *Renewable and Sustainable Energy Reviews*, vol. 13, 2008.

[16] Edward Barbour, "Energy Storage Technologies Explained". Retrieved from http://energystoragesense.com/energy-storage-technologies/, consulted the 9th of May 2017.

[17] J. Bélanger, P. Venne and J.-N. Paquin, "The What, Where and Why of Real-Time Simulation", 2013.

[18] Chris Caerts, "Web-of-Cells Concept and Control Scheme (part 1)" (2016). Retrieved from http://www.electrairp.eu/index.php?option=com_content&view=article&id=354.

[19] Matthew T. Lawder, Bharatkumar Suthar, Paul W. C. Northrop, Sumitava De, C. Michael Hoff, Olivia Leitermann, Mariesa L. Crow, Shriram Santhanagopalan and Venkat R. Subramanian, "Battery Energy Storage System (BESS) and Battery Management System (BMS)for Grid-Scale Applications", *Proceedings of the IEEE*, vol. 102, no. 6, 2014.

[20] Math H.J. Bollen, *Understanding Power Quality Problems.* IEEE Press Series on Power Engineering, 2000.

[21] Marshall Brain, "How Lithium-ion Batteries Work". Retrieved from http://electronics.howstuffworks.com/everyday-tech/lithium-ion-battery1.htm, consulted the 10th of May 2017.

[22] Chris Woodford, "Lithium-ion batteries" (2014, December). Retrieved from http://www.explainthatstuff.com/how-lithium-ion-batteries-work.html, consulted the 10th of May 2017.

[23] H.J. Bergveld, W.S. Kruijt and P.H.L. Notten, *Battery Management Systems: Design by Modelling.* Eindhoven : Philips Research Laboratories, 2002.

[24] David Linden and Thomas Reddy, *Handbook of batteries.* McGraw-Hill, 2001.

[25] Daniel H. Doughty and Chris C. Crafts, "FreedomCAR Electrical Energy Storage System Abuse Test Manual for Electric and Hybrid Electric Vehicle Applications", Sandia National Laboratories, 2006.

[26] Yuan Zou, Xiaosong Hu, Hongmin Ma and Shengbo Eben Li, "Combined State of Charge and State of Health estimation over lithium-ion battery cell cycle lifespan for electric vehicles", *Journal of Power Sources*, vol. 273, pp. 793-803, 2015.

[27] D. W. Dennis, V. S. Battaglia and A. Belanger, “Electrochemical modeling of lithium polymer batteries”, *Journal of Power Sources*, vol. 110, pp. 310–320, 2002.

[28] Ryan C. Kroeze and Philip T. Krein, "Electrical Battery Model for Use in Dynamic Electric Vehicle Simulations", University of Illinois, 2008.

[29] P. Rong and M. Pedram, “An analytical model for predicting the remaining battery capacity of lithium-ion batteries", University of Southern California, 2003.

[30] Hongwen He, Rui Xiong and Jinxin Fan, "Evaluation of Lithium-Ion Battery Equivalent Circuit Models for State of Charge Estimation by an Experimental Approach", *Energies*, vol. 4, pp. 582-598, 2011.

[31] Mohsen Mousavi, Shaikh Hoque, Shahryar Rahnamayan, Ibrahim Dincer, Greg F. Naterer, "Optimal Design of an Air-Cooling System for a Li-Ion Battery Pack in Electric Vehicles with a Genetic Algorithm", in Proceedings of the IEEE Congress on Evolutionary Computation, 2000.

[32] E. Sarasketa-Zabala, E. Martinez-Laserna, M. Berecibar, I. Gandiaga, L.M. Rodriguez-Martinez, I. Villarreal,"Realistic lifetime prediction approach for Li-ion batteries", *Applied Energy*, vol. 162, pp. 839-852, 2015.

[33] Battery University, "BU-802b: What does Elevated Self-discharge Do?" (2017, April). Retrieved from http://batteryuniversity.com/learn/article/elevating_self_discharge.

[34] Panasonic, CGR18650AF datasheet. Retrieved from http://www.datasheetarchive.com/pdf/download.php?id=66592976dbf72936a88cde4c94c9b19d803011&type=P&query=CGR18650A.

[35] Florian Krismer, "Modeling and Optimization of Bidirectional Dual Active Bridge DC–DC Converter Topologies", PhD thesis, ETH Zurich, 2010.

[36] G. Chen, Y.-S. Lee, S. Y. R. Hui, D. Xu and Y. Wang, “Actively clamped bidirectional flyback converter”, *IEEE Transactions on Industrial Electronics*, vol. 47, no. 4, 2000.

[37] Carl Blake and Chris Bull, "IGBT or MOSFET: Choose Wisely", Infineon, 2003.

[38] Infineon, "IGBT Selection Guide", Retrieved from `http://www.infineon.com/dgdl/Infineon-IGBT_Discretes_Selection_Guide-SG-v00_00-EN.pdf?fileId=db3a3043324cae8c01326cea43bc17bc`.

[39] Federico Ibáñez, Javier Vadillo, Miguel Martínez-Iturralde Maiza and José Martín Echeverría, "30kW DC-DC Converters with Regenerative Mode for Electric Cars", *Journal of Power Electronics*, vol. 12, pp. 233-241, 2012.

[40] Texas Instruments, "Phase-Shifted Full Bridge DC/DC Power Converter Design Guide", 2014.

[41] Sayed Ali Khajehoddin, Masoud Karimi Ghartemani, Praveen Jain and Alireza Bakhsai, "Distributed Power Generation Interface", U.S. Patent 8,668,287 B2.

[42] John Cheng, "IEEE Standard 519-2014", Schneider. Retrieved from `http://www.schneider-electric.com.tw/documents/Event/2016_electrical_engineering_seminar/IEEE_STD_519_1992vs2014.pdf`, consulted the 7th of June 2017.

[43] N. A. Rahim and S. Mekhilef, "High Efficiency THIPWM Three-Phase Inverter for Grid Connected System", In Proc. IEEE Symposium on Industrial Electronics and Applications, 2010.

[44] Witold Mazgaj, Bartosz Rozegnal and Zbigniew Szular, "Switching Losses in Three-phase Voltage Source Inverters", 2015.

[45] Frede Blaabjerg, Remus Teodorescu, Marco Liserre and Adrian V. Timbus, "Overview of Control and Grid Synchronization for Distributed Power Generation Systems", *IEEE Transactions on Industrial Electronics*, vol. 53, no. 5, 2006.

[46] Remus Teodorescu, Frede Blaabjerg and Marco Liserre, "Proportional-Resonant Controllers : A New Breed of Controllers Suitablefor Grid-Connected Voltage-Source Converters", Proceedings of The 9th International Conference on Optimization of Electrical and Electronic Equipments, 2004.

[47] Masoud Karimi-Ghartemani, *Enhanced Phase-locked Loop Structures for Power and Energy Applications*. Wiley IEEE Press Series on Microelectronic Systems, 2014.

[48] Mojgan Nikouie, Oskar Wallmark, Lebing Jin and Hans-Peter Nee, "A DC-link Voltage Control Scheme for Single-phase Grid-connected PV Inverters", Proceedings of Energy Conversion Congress and Exposition, 2011.

[49] Kyung Soo K, McKenzie KJ, Yilu L and Atcitty S., "A study on applications of energy storage for the wind power operation in power systems", Proc. IEEE Power Engineering Society General Meeting, 2006.

[50] Wei L and Joos G., "Performance comparison of aggregated and distributed energy storage systems in a wind farm for wind power fluctuation suppression", Proc. Power Engineering Society General Meeting, 2007.

[51] Aneel Kumar Akhani, "Primary Secondary and Tertiary Frequency Control". Retrieved from `http://top10electrical.blogspot.be/2015/10/primary-secondary-and-tertiary.html`, consulted the 29th of May 2017.

[52] Hugues Chanoine, "Frequency regulation: the need for fast responding assets and the “mileage” case in the USA" (2013, September). Retrieved from `http://www.cleanhorizon.com/blog/2013/09/frequency-regulation-the-need-for-fast-responding-assets-and-the-mileage-case\-in-the-usa/`.

[53] Prabha Kundur, *Power System Stability and Control.* Electric Power Research Institute, 1994.

[54] D.P.Kothari and I.J. Nagrath, *Modern Power System Analysis*. McGraw-Hill, 1980.